IMAGING UNDER SALT: ILLUMINATION COMPENSATION BY REGULARIZED INVERSION

A DISSERTATION
SUBMITTED TO THE DEPARTMENT OF GEOPHYSICS
AND THE COMMITTEE ON GRADUATE STUDIES
OF STANFORD UNIVERSITY
IN PARTIAL FULFILLMENT OF THE REQUIREMENTS
FOR THE DEGREE OF
DOCTOR OF PHILOSOPHY

Marie L. Clapp
July 2005

© Copyright 2005 by Marie L. Clapp
All Rights Reserved

printed as Stanford Exploration Project No. 122
by permission of the author

Copying for all internal purposes of the sponsors
of the Stanford Exploration Project is permitted

I certify that I have read this dissertation and that in my opinion it is fully adequate, in scope and quality, as a dissertation for the degree of Doctor of Philosophy.

Biondo Biondi
(Principal Adviser)

I certify that I have read this dissertation and that in my opinion it is fully adequate, in scope and quality, as a dissertation for the degree of Doctor of Philosophy.

Jon F. Claerbout

I certify that I have read this dissertation and that in my opinion it is fully adequate, in scope and quality, as a dissertation for the degree of Doctor of Philosophy.

Gary Mavko

Approved for the University Committee on Graduate Studies.

Abstract

Imaging in areas of strong velocity contrasts is an increasingly important problem in the search for hydrocarbons. The multipathing and poor illumination that occur in such areas render conventional imaging techniques inadequate. Traditional imaging techniques use a migration operator to reverse the wavefield propagation. Unfortunately, migration alone cannot properly image areas of poor illumination. This problem has been overcome with an iterative inversion that uses an imaging operator and its adjoint along with a regularization operator.

The imaging operator used in the inversion process is a linear operator relating reflectivities to data (a migration operator). This operator creates an image that includes angle domain (or offset ray parameter) common image gathers (ADCIGs). I regularize the image space using two different regularization schemes. In the first scheme, called the geophysical scheme, the regularization operator acts horizontally along the ray parameter axis. This assumes that there is no moveout along the ray parameter axis, meaning that the correct velocity model has been used by the imaging operator. The geophysical regularization operator penalizes large changes in amplitude along offset ray parameters, which are assumed to be caused by poor illumination. The second regularization scheme, called the geological scheme, combines the first regularization operator with a second regularization operator that acts along specified dips at every point in the X-Z plane. This geological regularization tends to create events with the user-specified dip at each point in the X-Z plane. This allows information from a seismic interpretation or geological model to be included in the inversion.

The images obtained with both of my regularized inversion schemes are cleaner than the result of migration alone and the events in areas of poor illumination are stronger and more

consistent in amplitude. The geophysical regularization scheme is demonstrated on real 2-D and 3-D data and the geological regularization is demonstrated on real 2-D data.

Preface

All of the figures in this thesis are marked with one of the three labels: [ER], [CR], and [NR]. These labels define to what degree the figure is reproducible from the data directory, source code and parameter files provided on the web version of this thesis [1].

ER denotes Easily Reproducible. The author claims that you can reproduce such a figure from the programs, parameters, and data included in the electronic document. We assume you have a UNIX workstation with Fortran90, Fortran77, C, X-Window system, and the SEPlib software package. Before the publication of the electronic document, someone other than the author tests the author's claim by destroying and rebuilding all ER figures.

CR denotes Conditional Reproducibility. The author certifies that the commands are in place to reproduce the figure if certain resources are available. SEP staff have not attempted to verify the author's certification. To find out what the required resources are, you can inspect a corresponding warning file in the document's result directory. For example, you might need a large or proprietary data set. You may also need a super computer, or you might simply need a large amount of time (20 minutes or more) on a workstation.

NR denotes Non-Reproducible. This class of figure is considered non-reproducible. Figures in this class are scans and artists' drawings. Output of interactive processing are labeled NR.

[1] http://sepwww.stanford.edu/public/docs/sep122

Acknowledgements

It is impossible to adequately acknowledge everyone who has helped me on this long, strange journey. So many people have contributed in so many ways, I could write another 100 pages and still not feel that I have thanked everyone. I'll spare you that, though, and try to limit myself.

I'll start with my family. My sisters and brothers, Sue, Theresa, Alan, and Steve, honed my competitiveness and strengthened my stubborn streak, both of which were vital throughout my school years. Mom has always supplied me with love, support and kisses on the forehead. Dad taught me that you can always work harder than you thought you could.

I wouldn't be here without a love of science, which started as a small spark when I was in elementary school and was fanned into an inferno by my 8th grade science teacher, Mr. Maddox. I was fortunate enough to spend my undergraduate years at the Colorado School of Mines, where Dr. Larner and Dr. Kaufman channeled my scientific aptitude into geophysics. Also at Mines, I made wonderful friends who got me through the stress of my undergraduate work, then taunted me (in a nice way) as I went to graduate school. Thank you for being there for me, Ang, Bry, Kelly, Tiff and J.

Now for the part of my acknowledgments that I know all the SEPers want to read. First, I would never have entered the PhD program if Jon and Biondo hadn't encouraged me. Now that I have this thesis done, I can thank them unconditionally for that confidence. More importantly, the majority of the theory in this thesis comes from long discussions with Biondo.

SEP is fortunate to have the best administrator in the whole school: Diane. She handles all of the details that keep the group running smoothly and still had time to chat when I needed to

connect with a “real” person (meaning not a geophysicist!). Thanks, Diane, you kept me sane - most of the time.

OK, now for my fellow students. I’ll start with some individual acknowledgments. Paul was extremely useful with good conversations and tons of coding support. Morgan also provided good conversations and introduced me to rock climbing, which is a great stress reliever when you get pass acrophobia. Reaching back a bit into the past, Sean also provided good conversations and on occasion rescued me from some practical jokes played on me by an officemate. Many thanks for help and discussions to Sergey, who really intimidated me until I realized that he considered me a colleague, which seems to be Russian for “someone with whom to sip vodka”.

On a more general note, I want to thank all of my officemates who put up with my singing, decorating, incredibly loud plaid shirts, and occasional emotional breakdowns. Also, it hasn’t always been easy being the only woman in SEP, but all of the guys have been wonderful about treating me just like ... well, one of the guys. Except for when I was walking around hugely pregnant for the week after my due date and everyone seemed a bit nervous. We all got through it, though, and you all were great. Thanks!

I also need to thank all of the past SEPers who built the infrastructure I relied on to do my work. For both software and theory, I have stood on the shoulders of giants.

Now for the financial thank-yous. First, my gratitude to all contributors to the beer fund. Friday beers are where you really learn the most about your colleagues, so all of the late fees are worth it. On a more serious note, I have to thank all of SEP’s sponsors for supporting us. Also, thank you for providing us with data (for my thesis, a special thanks to BP and ExxonMobil).

I have saved the most important thank-you for last. Bob, I simply would not be getting my PhD without your help and support. You and Sammy are the best things I will be taking away from Stanford.

Contents

Abstract **iv**

Preface **vi**

Acknowledgements **vii**

1 Introduction **1**

2 Migration in complex areas **9**

3 Imaging by inversion **23**

4 Real data results **61**

5 Summary **93**

Bibliography **96**

List of Figures

1.1 Model of a complex subsurface. The rays emanating from the point at depth 1.8 km and x location 10 km represent seismic energy that is trying to get below the salt body. As the energy encounters the salt body (shown in black), most of it is directed away from the reflectors that exist below the salt. 2

1.2 Model of a complex subsurface. The rays emanating from the point at depth 4.25 km and x location 10 km represent seismic energy that is trying to reach the surface. As the energy encounters the salt body (shown in black), some of it is directed away from the receivers that exist at the surface. 3

1.3 Image produced by migration from the data recorded over the subsurface in Figure 1.1. The events seen clearly on the left side of the image die out as they go beneath the salt. These are the shadow zones. 4

2.1 The relationships of the *surface-related* parameters source (s) and receiver (g) locations, and their sections and gathers. The top part shows a simple survey geometry over a single flat subsurface reflector: the single source (s) is connected to each receiver (g) by rays that reflect at the flat reflector. The lower part shows various ways we can arrange the data based on the relation of the shot and receiver. The axes are labeled to indicate the source location (s), receiver location (g), offset (h) which is the difference between the receiver and shot locations ($h = g - s$), and the midpoint location (y), which is halfway between the source and receiver ($y = (s+g)/2$). (From (Claerbout, 1995)) . 12

2.2 Raypaths through a fairly simple velocity model consisting of a weak vertical velocity gradient and a strong low velocity lens. An individual shot gather will contain energy that travels along both of these raypaths. The low velocity lens allows both traveltimes and receiver ray parameters p_r to be identical. 13

2.3 Raypaths through a simple constant velocity velocity model with a low velocity lens. An individual common offset gather will contain energy that travels along both of these raypaths. The arrivals will have identical traveltimes and midpoint ray parameters. 13

2.4 Defining the angle domain. The reflector element is completely defined by its subsurface location **x** and its dip vector ν. This reflector element will be represented at the surface by an event element defined by s, p_s, r, p_r, t, the source position, source ray parameter, receiver position, receiver ray parameter, and two way travel time, respectively. The connection of the reflector element to the event element comes from the incident and reflected rays that define the opening angle θ. 14

2.5 Left: Offset panel after downward continuation. Right: Angle-domain CIG . 21

2.6 Raytracing through a velocity model with a strong low velocity lens. The maximum offset recorded in this model is 3000 meters, so rays that are separated by more than 3000 meters at the surface represent energy that is lost. 22

2.7 Migration result from the velocity model shown in Figure 2.6. The common p_{hx} section (left panel) has shadow zones positive and negative 600m in CRP. The ADCIG (right panel) has clear “holes” in the events caused by energy leaving the bounds of the survey, as demonstrated by Figure 2.6. The depth slice (top panel) shows the illumination problem as white streaks through the black triangle. 22

3.1 Downward continuation migration result for part of the Sigsbee2A model. Left: common offset ray parameter section. Ovals indicate interesting areas of poor illumination. Right: four CIGs taken from between CRP 10.0 km and 10.25 km. Arrows indicate holes in the events. 28

3.2 Velocity model for part of the Sigsbee2A model. 29

3.3 Result of 10 iterations of geophysical RIP for part of the Sigsbee2A model. Left: common offset ray parameter section. The amplitudes and continuity within the ovals is improved compared to Figure 3.1. Right: four CIGs taken from between CRP 10.0 km and 10.25 km. The holes indicated by the arrows are largely filled in. The artifacts that existed in the shadow zones are cleaned up. 30

3.4 Reflectors picked from the migration result for part of the Sigsbee2A model, overlaid on the stack of the migration result. 32

3.5 Result of 8 iterations of geological RIP for part of the Sigsbee2A model. Left: common offset ray parameter section. The amplitudes and continuity within the ovals is improved compared to Figure 3.1 and Figure 3.3. Right: four CIGs taken from between CRP 10.0 km and 10.25 km. The holes indicated by the arrows are completely filled in. 33

3.6 Reflectors picked from the actual reflectivity model for part of the Sigsbee2A model, overlaid on the stack of the migration result. 34

3.7 Result of 8 iterations of geological RIP for part of the Sigsbee2A model, using the reflectors picked from the actual reflectivity model. Left: common offset ray parameter section. The amplitudes and continuity within the ovals is improved compared to Figure 3.1 and Figure 3.3. Right: four CIGs taken from between CRP 10.0 km and 10.25 km. The holes indicated by the arrows are completely filled in. 35

3.8 The recorded data corresponding to a synthesized seismic survey over the velocity model in Figure 2.6. The triangular shaped extent of the data seen in the time slice (top) is caused by the limited survey geometry. 37

3.9 The result of migrating the data in Figure 3.8. Note the holes in the CIGs indicating poor illumination caused by seismic energy being directed outside of the survey area. 38

3.10 Result after 3 iterations of geophysical RIP. The holes in the CIGs seen in Figure 3.9 have been largely filled in. 39

3.11 The "expanded" data after 3 iterations of geophysical RIP. The regularization of the model space has filled in areas from which the seismic data was directed outside of the survey area. This has "extended" the data beyond the limits seen in Figure 3.8. 40

3.12 Constant velocity example of "lost" frequencies. Left: model space where regularization spreads energy throughout the region bounded by the two horizontal lines. Right: data space where the two bounding lines now curve upward. The dashed lines indicate the frequency range of the original data. 42

3.13 The weighting operator ($\mathbf{W}_{\mathrm{m}}^{2}$) produced using flat layers as the reference model. 44

3.14 Results enlarged from CRP $=$ 9.75km to CRP $=$ 11.25km. Left: stack of migration. Center: stack of model space weighted result. Right: stack of result after 10 iterations of geophysical RIP. 46

3.15 Migration result with the picked "reflectors" overlaid. These reflectors do not match the correct reflectors and should produce a bad result. 48

3.16 Result of 3 iterations of the geologically regularized result with badly picked reflectors. 49

3.17 The result of 3 iterations of geophysical RIP inversion using the correct velocity model. Note the more consistent amplitudes of events as they pass beneath the salt in the CRP-depth panel and the lack of artifacts obscuring events beneath the salt (inside ovals). In the offset ray parameter-depth panel note the filling in of the holes in the events at the mid-range of offset ray parameters (inside ovals). 54

3.18 The result of downward-continuation migration using a velocity model 5% higher than the correct model. The events are all positioned deeper than they should be and there is moveout along the offset ray parameter axis. The ovals still indicate the loss of amplitudes under the salt edge and the poor imaging beneath the salt in the CRP-depth panel and holes in the events in the p_h panel. 55

3.19 The result of 3 iterations of regularized inversion using the 5% scaled up velocity model. Despite the use of the incorrect velocity model, the image is quite comparable to the result using the correct velocity (Figure 3.17). In the CRP-depth panel, the events extend farther under the salt and events under the salt can be seen (inside the ovals). In the p_h-depth panel, the holes in the events are filled in (inside the oval). 56

3.20 The smoothed velocity model. Note that the canyon in the top of the salt has disappeared. 56

3.21 The result of downward-continuation migration using a severely smoothed velocity model. The events in the CRP-depth panel are properly imaged away from the salt but are mispositioned near the salt. The offset ray parameter-depth panel is completely uninformative. The ovals indicate the same absolute regions as the ovals in 3.17. 57

3.22 The result of 3 iterations of preconditioned inversion using the smoothed velocity model. The result is cleaner than the migration result, but not more believable. The ovals indicate the same absolute regions as the ovals in 3.17. . 58

3.23 Velocity model to test the effect of geophysical RIP on AVA. 58

3.24 Amplitude variation with p_h. Left panel shows the results for the shallowest interface as seen in Figure 3.23, center panel for the second interface, and right panel for the deepest interface. The solid line shows the theoretical value and the dots show the values obtained from the image after downward-continuation migration. 59

3.25 Amplitude variation with p_h for geophysical regularization after 5 iterations. Left panel shows the results for the shallowest interface as seen in Figure 3.23, center panel for the second interface, and right panel for the deepest interface. The solid line shows the theoretical value and the dots show the values obtained after inversion. 59

3.26 Amplitude variation with p_h for geophysical regularization after 10 iterations. Left panel shows the results for the shallowest interface as seen in Figure 3.23, center panel for the second interface, and right panel for the deepest interface. The solid line shows the theoretical value and the dots show the values obtained after inversion. 59

3.27 Amplitude variation with p_h for geophysical regularization after 15 iterations. Left panel shows the results for the shallowest interface as seen in Figure 3.23, center panel for the second interface, and right panel for the deepest interface. The solid line shows the theoretical value and the dots show the values obtained after inversion. 60

4.1 Subset of the BP Gulf of Mexico velocity model. 62

4.2 Top: result of downward-continuation migration of 2-D line. Left part is a common offset ray parameter section at $p_h = .265$, right part is a common image gather from $CRP = 20.675$. Bottom: result of 6 iterations of geophysical RIP. 64

4.3 Top: result of downward-continuation migration of 2-D line. Left part is a common offset ray parameter section at $p_h = .235$, right part is a common image gather from $CRP = 20.575$. Bottom: result of 6 iterations of geophysical RIP. 65

4.4 Top: result of downward-continuation migration of 2-D line. Left part is a common offset ray parameter section at $p_h = .1375$, right part is a common image gather from $CRP = 22.5$. Bottom: result of 6 iterations of geophysical RIP. 66

4.5 Top: result of downward-continuation migration of 2-D line. Left part is a common offset ray parameter section at $p_h = .265$, right part is a common image gather from $CRP = 21.575$. Bottom: result of 6 iterations of geophysical RIP. 67

4.6 Zoomed portion of Figure 4.2. Top: result of downward-continuation migration of 2-D line. Left part is a common offset ray parameter section at $p_h = .265$, right part is a common image gather from $CRP = 20.675$. Bottom: result of 6 iterations of geophysical RIP. Ovals indicate areas where poor illumination exists in the migration result and is improved in the RIP result. . 68

4.7 Zoomed portion of Figure 4.3. Top: result of downward-continuation migration of 2-D line. Left part is a common offset ray parameter section at $p_h = .235$, right part is a common image gather from $CRP = 20.575$. Bottom: result of 6 iterations of geophysical RIP. Ovals indicate areas where poor illumination exists in the migration result and is improved in the RIP result. . 69

4.8 Zoomed portion of Figure 4.4. Top: result of downward-continuation migration of 2-D line. Left part is a common offset ray parameter section at $p_h = .1375$, right part is a common image gather from $CRP = 22.5$. Bottom: result of 6 iterations of geophysical RIP. Ovals indicate areas where poor illumination exists in the migration result and is improved in the RIP result. . 70

4.9 Zoomed portion of Figure 4.5. Top: result of downward-continuation migration of 2-D line. Left part is a common offset ray parameter section at $p_h = .265$, right part is a common image gather from $CRP = 21.575$. Bottom: result of 6 iterations of geophysical RIP. Ovals indicate areas where poor illumination exists in the migration result and is improved in the RIP result. . 71

4.10 Top: stack of the result of downward-continuation migration of 2-D line. Bottom: stack of the result of 6 iterations of geophysical RIP. Ovals indicate areas where poor illumination exists in the migration result and is improved in the RIP result. 72

4.11 Comparison of the data space residuals from RIP with geophysical regularization. The vertical axis is time, the horizontal axis is offset. Each row is a collection of CMP gathers taken from locations across the whole survey, taking the envelope of the energy and clipping the high values (indicated by black). The first row is the original data, the second row shows the same CMP gathers after 2 iterations, the third row is after 4 iterations, fourth row after 6 iterations, fifth row after 8 iterations and sixth after 10 iterations. 73

4.12 Migration result overlaid by the reflectors picked for geological regularization. 74

4.13 Top: result of downward-continuation migration of 2-D line. Left part is a common offset ray parameter section at $p_h = .265$, right part is a common image gather from $CRP = 20.675$. Bottom: result of 6 iterations of geological RIP. This result can also be compared to the geophysical RIP result in Figure 4.2. 76

4.14 3-D image displayed with depth slice, inline section from crossline=21.125 km and crossline section from inline=20.35 km. Top: stack after common azimuth migration. Bottom: stack after 7 iterations of geophysical RIP. Ovals indicate areas of particular improvement in the RIP result. 78

4.15 3-D image displayed with depth slice, inline section from crossline=20.9 km and crossline section from inline=21.675 km. Top: stack after common azimuth migration. Bottom: stack after 7 iterations of geophysical RIP. Ovals indicate areas of particular improvement in the RIP result. 79

4.16 Zoomed 3-D image displayed with depth slice, inline section from crossline=21.3 km and crossline section from inline=23.25 km. Top: stack after common azimuth migration. Bottom: stack after 7 iterations of geophysical RIP. Ovals indicate areas of particular improvement in the RIP result. 80

4.17 Zoomed 3-D image displayed with depth slice, inline section from crossline=20.6 km and crossline section from inline=23.5 km. Top: stack after common azimuth migration. Bottom: stack after 7 iterations of geophysical RIP. Ovals indicate areas of particular improvement in the RIP result. 81

4.18 Migration result. Crossline=20.9 km, common inline p_h section from $p_h =$ .1875, and common image gather from inline=20.375 km. Compare with Figure 4.19. 84

4.19 Geophysical RIP result. Crossline=20.9 km, common inline p_h section from $p_h = .1875$, and common image gather from inline=20.375 km. Compare with Figure 4.18. 85

4.20 Migration result. Crossline=20.9 km, common inline p_h section from $p_h =$ .2325, and common image gather from inline=21.65 km. Compare with Figure 4.21. 86

4.21 Geophysical RIP result. Crossline=20.9 km, common inline p_h section from $p_h = .2325$, and common image gather from inline=21.65 km. Compare with Figure 4.20. 87

4.22 Migration result. Crossline=20.9 km, common inline p_h section from $p_h =$ .15, and common image gather from inline=20.9 km. Compare with Figure 4.23. 88

4.23 Geophysical RIP result. Crossline=20.9 km, common inline p_h section from $p_h = .15$, and common image gather from inline= 20.9 km. Compare with Figure 4.22. 89

4.24 Migration result. Crossline=20.9 km, common inline p_h section from $p_h = .2925$, and common image gather from inline=20.9 km. Compare with Figure 4.25. 90

4.25 Geophysical RIP result. Crossline=20.9 km, common inline p_h section from $p_h = .2925$, and common image gather from inline=20.9 km. Compare with Figure 4.24. 91

Chapter 1

Introduction

Today's world is still quite far from overcoming its dependence on hydrocarbons. Unfortunately, finding hydrocarbons is getting more and more difficult. They are no longer found by simply looking for surface anticlines. We now look for hydrocarbons deep within the earth in stratigraphic or structural traps (Dobrin and Savit, 1988). In this thesis, I am concerned with improving our ability to create images of complex structural traps using seismic data.

A good location for a structural trap is at the edges of salt bodies in the subsurface. These salt bodies are often found under deep water, making it economically unfeasible to just drop a well (wildcatting). Therefore, we want to image the subsurface surrounding the salt as well as possible. Unfortunately, salt has a very high seismic velocity (often twice as high as the surrounding subsurface) that significantly reduces the amount of seismic energy that gets through to the surrounding rock (Figure 1.1, seismic energy is represented by rays). This energy may be directed outside of the bounds of the seismic survey (Figure 1.2), or become evanescent (die out) at the salt boundaries. This poor illumination makes it very difficult to image the potential hydrocarbon traps.

Imaging the subsurface is commonly done with some type of migration. Migration tries to move the seismic energy recorded at the earth's surface back to where it belongs in the subsurface, thereby creating an image of the subsurface. Poor illumination will cause "shadow zones" in the resulting image, in the areas where we hope to find the potential hydrocarbon

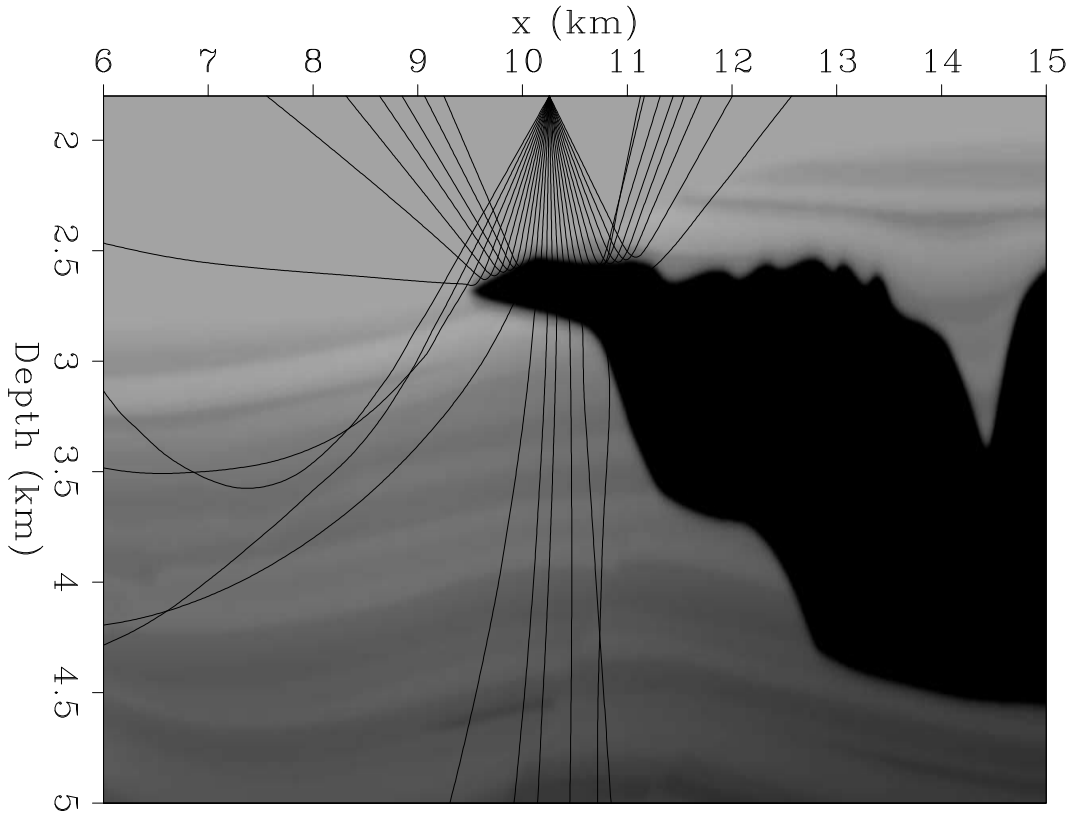

Figure 1.1: Model of a complex subsurface. The rays emanating from the point at depth 1.8 km and x location 10 km represent seismic energy that is trying to get below the salt body. As the energy encounters the salt body (shown in black), most of it is directed away from the reflectors that exist below the salt. intro-ray.down [ER]

traps. These shadow zones are clear in Figure 1.3, which shows the result of trying to migrate the seismic data collected over the subsurface shown in Figure 1.1. Shadow zones often contain some seismic signal that may be recovered with better imaging techniques. However, some of the information we would need to fill in these areas does not exist in the data at all.

CONVENTIONAL METHODS

Even in areas with poor illumination, there is generally some signal present, it is just weak and obscured by noise. Conventional methods for trying to improve imaging in poorly illuminated

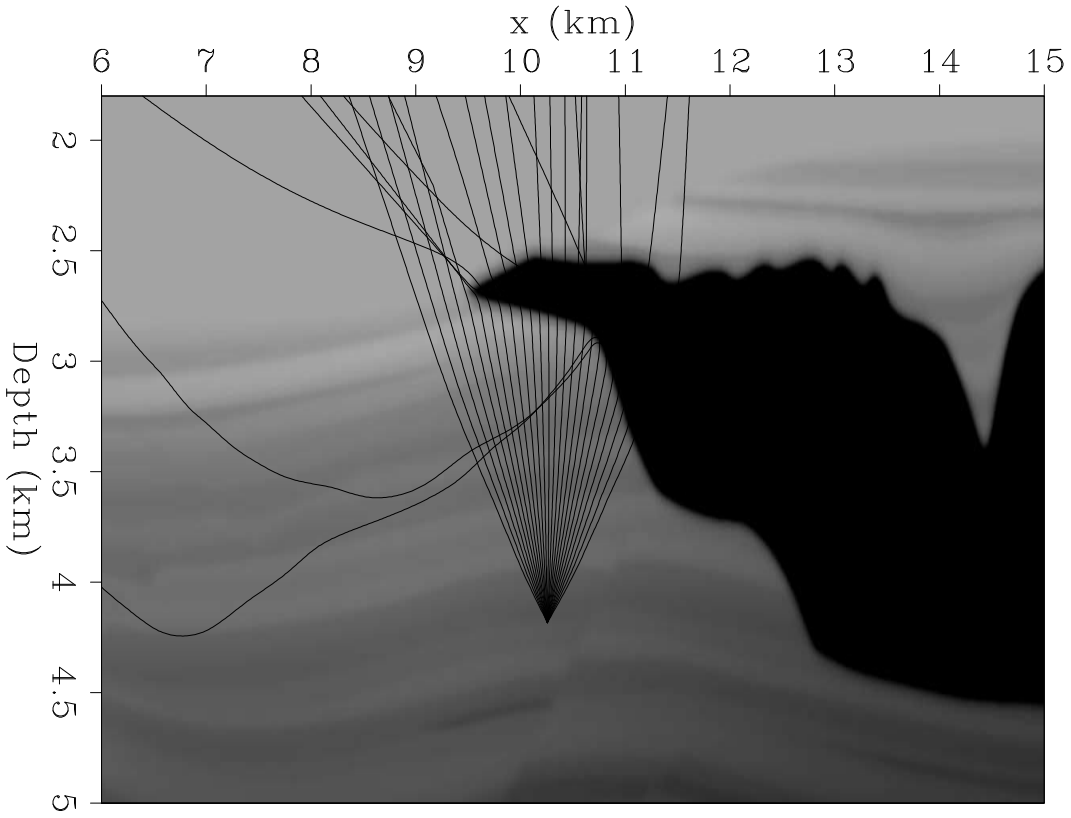

Figure 1.2: Model of a complex subsurface. The rays emanating from the point at depth 4.25 km and x location 10 km represent seismic energy that is trying to reach the surface. As the energy encounters the salt body (shown in black), some of it is directed away from the receivers that exist at the surface. intro-ray.up [ER]

areas often try to improve the signal-to-noise ratio. One of the simplest ways to do this is to apply some type of weighting (scaling) to the image after migration. One common example of this attempted improvement is automatic gain control (AGC). There are other better ways to a apply weighting such as the illumination-dependent operator described by Rickett (2001). Unfortunately, these weighting methods can easily increase the level of noise as well as the signal level.

Other methods to improve imaging in poorly illuminated areas often manipulate the migration algorithm itself. For example, it is well known that long-time industry standard prestack Kirchhoff migration will not perform well in areas like those beneath salt edges. Kirchhoff

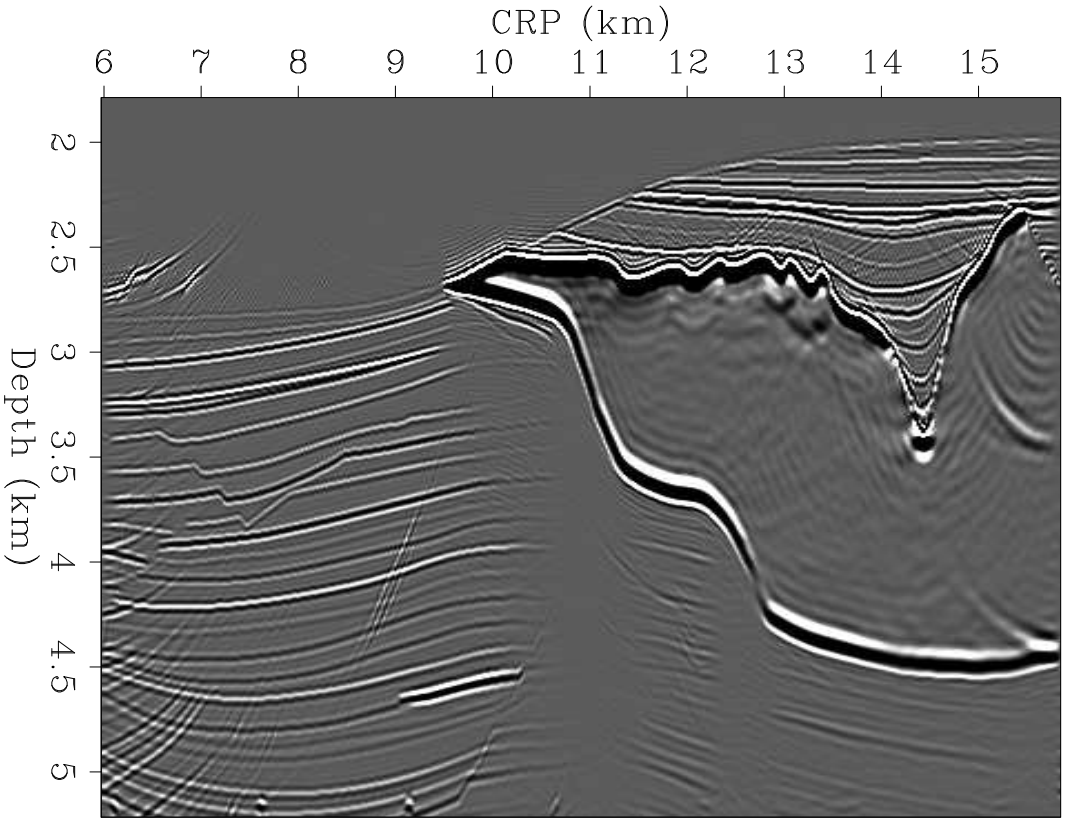

Figure 1.3: Image produced by migration from the data recorded over the subsurface in Figure 1.1. The events seen clearly on the left side of the image die out as they go beneath the salt. These are the shadow zones. intro-stack.mig [CR]

migration tries to add up all of the energy in the recorded data that can be connected to a point in the subsurface with "rays" that trace a path through the subsurface from the seismic source to the receivers. Results from such migration algorithms contain poorly illuminated areas that are full of artifacts, many of which are caused by multipathing (ten Kroode et al., 1994). These artifacts can be reduced by using a Kirchhoff algorithm that creates an image in reflection angle space (Xu et al., 2001). However, even this Kirchhoff algorithm will produce a result with shadow zones beneath the salt edges. One reason for this occurrence is that Kirchhoff methods impose an implicit high frequency assumption on the wave equation. They use ray-based theories of wave propagation in the subsurface, which break down around large velocity contrasts like those at salt boundaries.

Fortunately, we now have the computational power to use migration algorithms that are based on the wave equation without making a high frequency assumption. An example of this type of algorithm is downward-continuation migration. Downward continuation (source-receiver) migration uses the Double Square Root equation to push the wavefield recorded at the surface back into the subsurface, which "moves" the seismic energy to its proper depth. Since this algorithm uses the whole recorded wavefield rather than making a high frequency assumption, it has less severe illumination problems in areas of large velocity contrasts. This can be further improved by reducing multipathing artifacts with a downward-continuation migration algorithm that creates an image in reflection angle space (Prucha et al., 1999).

These are just a few of the possible methods to improve imaging in poorly illuminated areas. The examples described here are sufficient background for the work that will be presented in this thesis.

OVERVIEW OF THESIS

This thesis will show that it is possible to improve imaging in areas of poor illumination. This is accomplished through the use of regularized inversion with model preconditioning.

Imaging with migration

Chapter 2 of this thesis more thoroughly explains the problems encountered when attempting to image areas with strong velocity contrasts using migration. The migration algorithms it describes are designed to produce an image with angle-domain common image gathers (ADCIGs). The creation of ADCIGs helps to reduce artifacts caused by multipathing, a problem that is also explained in Chapter 2 and which is common in areas with strong velocity contrasts.

I will first explain how multipathing occurs in conventional shot- and offset-domain type migration. Then I will review a Kirchhoff migration that produces ADCIGs (Xu et al., 1998). As with most Kirchhoff methods, this does not necessarily perform well in areas with strong velocity contrasts. Therefore, I will introduce a wave-equation based migration that produces ADCIGs.

The migration algorithm used in this thesis is called downward-continuation migration (Prucha et al., 1999). It uses the Double Square Root (DSR) equation to downward continue the wavefield recorded at the surface, then at each depth step performs slant stacking (Schultz and Claerbout, 1978) to create the ADCIGs. The slant stacking step creates an offset ray parameter axis in the resulting image, which is equivalent to reflection angle. The DSR equation allows me to use all of the information recorded at the surface rather than making the type of high frequency assumption a Kirchhoff method requires. By slant stacking at each depth step, the algorithm can handle lateral velocity variations, unlike the method described by Ottolini and Claerbout (1984).

Although downward-continuation migration reduces artifacts seen in traditional shot- and offset-domain migration and Kirchhoff methods that create ADCIGs, it still has difficulty with poor illumination. In areas with strong velocity contrasts, the resulting image will have shadow zones. Migration is not capable of properly imaging these areas.

Imaging with inversion

When we try to image the subsurface, we are attempting to reverse the way the seismic energy traveled (propagated). Migration methods have difficulty imaging complex areas because migration algorithms cannot accurately reverse the propagation in these areas. Imaging these areas requires an algorithm that is able to *invert* the propagation.

Chapter 3 explains the new imaging technique that I am using to improve imaging of complex areas. This method is a Regularized Inversion with model Preconditioning (RIP). The inversion uses downward-continuation migration (Prucha et al., 1999) and its adjoint (matrix transpose) in an iterative conjugate gradient scheme to help extract all of the useful information from the recorded data. In addition, the regularization allows me to introduce *a priori* knowledge of what the resulting model (image) should look like to the inversion problem. By preconditioning the model, I can reduce the number of iterations needed to get an acceptable result.

I implement the regularization with two different schemes. My *geophysical* RIP acts to regularize amplitudes along the offset ray parameter (reflection angle) axis of the image. Poor

illumination will manifest itself as gaps along the offset ray parameter axis, so the regularization tries to fill these gaps. My *geological* RIP acts to regularize amplitudes along chosen dips in the common reflection point-depth space of the image. This scheme tries to fill in the shadow zones directly, by imposing an idea of the dips we expect to see in the model upon the inversion problem. Using these regularization schemes in the iterative conjugate gradient inversion will keep us from introducing elements in the model that conflict with the existing data.

Chapter 3 also examines several significant considerations for the use of RIP. First, the use of RIP for imaging is a relatively expensive procedure. Therefore, I compare the result of RIP with the result of model-space weighting, a cheap and commonly used method for trying to improve imaging in shadow zones. Second, geological RIP makes assumptions about the dips that may exist in the shadow zones. I investigate the result of using the wrong dips in a geological RIP scheme. In the geophysical RIP scheme, the regularization assumes that the correct velocity is being used for the downward continuation step. By experimenting with using incorrect velocity models, I test the importance of this assumption on the result of the regularized inversion. Finally, the regularization in the geophysical RIP scheme acts on the amplitudes, so I look at the effect of geophysical RIP on amplitude variation with offset ray parameter (angle).

Real data results

Chapters 2 and 3 use synthetic datasets to demonstrate the concepts explained therein. The true value of the RIP method should be judged by its effect on real data. Chapter 4 shows the result of using RIP on real seismic data. I apply geophysical and geological RIP to real 2-D data, and geophysical RIP to real 3-D data.

ASSUMPTIONS

All seismic processing depends on the processing steps already performed on the data (preprocessing). In the case of the inversion I demonstrate in this thesis, the preprocessing includes

velocity analysis. This means that for the datasets I will be dealing with, I assume the velocity model of the subsurface is correct. The regularized inversion method I am presenting is not intended as a tool for velocity estimation.

Chapter 2

Migration in complex areas

Migration is an attempt to construct a *model* of the earth's *subsurface* from *data* recorded at the earth's *surface*. The raw data is parameterized by the shot and receiver locations of the survey. This makes it natural for us to migrate the data in terms of shot and receiver locations, common midpoint (CMP) locations, and offset, which are all *surface-related* coordinates. Unfortunately, these surface-related migration methods often fail in areas where the subsurface is complex for reasons such as reflector ambiguity due to multipathing.

Multipathing is a phenomenon in which a single event in the data recorded at one surface location could be caused by reflectors at two or more subsurface model space locations. This reflector ambiguity will contribute to imaging artifacts when *surface-related* migration is performed. It can also cause additional problems such as non-flat events in common image gathers that render velocity analysis ambiguous (Nolan and Symes, 1996). If we do not limit ourselves to the *surface-related* domains for migration and turn to a *subsurface-related* domain like the reflection angle domain, the problems caused by multipathing can be avoided. In the *subsurface-related* domain, we deal with specific points in the subsurface and energy that arrives at and departs from these points at specific angles. Using these *subsurface-related* coordinates means there will not be reflector ambiguity, and thus no multipathing.

The artifacts caused by multipathing energy can cause serious problems for one of the

most commonly used migration schemes: Kirchhoff migration using surface-related coordinates. Although much work has been done to try to modify surface-related Kirchhoff migration to better handle areas with complex subsurfaces (Biondi, 2001; Akbar et al., 1998; Hokstad and Sollie, 1998; Audebert et al., 1997), Kirchhoff methods are fundamentally based on a high frequency assumption, which is known to break down in very complex areas. Fortunately, other migration methods such as downward-continuation migration do not make this assumption. Additionally, downward-continuation migration is well suited to be used in the subsurface-related reflection angle domain.

In this chapter, I will examine the phenomenon of multipathing as it relates to the surface-related shot and offset domains. I will then explain how the artifacts resulting from multipathing can be avoided in the subsurface-related reflection angle domain. I will review how Kirchhoff migration can be performed in the reflection angle domain, then introduce a subsurface-related downward-continuation migration method that is less likely to have imaging artifacts than the Kirchhoff method. Finally, I will show that even the downward-continuation method will not provide a perfect image of a very complex subsurface at least in part because of poor illumination.

SURFACE-RELATED DOMAINS: SHOT AND OFFSET

Shot locations and offsets are parameterized according to their location on the earth's surface where the seismic data is recorded. Seismic processing using these surface-related coordinates has been researched by geophysicists for decades. The kinematics of shot domain common image gathers and offset domain image gathers are well understood in constant velocity and $v(z)$ media (Claerbout, 1995; Dobrin and Savit, 1988; Yilmaz, 1987). Difficulties arise when we begin considering complex subsurfaces with rapid lateral velocity variations. Even in 2-D it is easy to construct a model for which an individual common shot gather or common offset gather can contain two events from two points in the subsurface that arrive at the same time and are indistinguishable. In order to examine such cases, let us first review basic survey geometry. Figure 2.1, from Claerbout (1995), shows the relationship between the source, receiver, midpoint locations and offsets, as well as the relationships between various common

image gathers and common image sections. The top part of Figure 2.1 shows a simple survey geometry over a single flat subsurface reflector: the single source (s) is connected to each receiver (g) by rays that reflect at the flat reflector. The lower part of Figure 2.1 shows various ways we can arrange the data based on the relation of the shot and receiver. The axes are labeled to indicate the source location (s), receiver location (g), offset (h) which is the difference between the receiver and shot locations ($h = g - s$), and the midpoint location (y) which is halfway between the source and receiver ($y = (s+g)/2$). Based on this diagram, we can organize the raw data in many surface-related ways: in common shot gathers, common receiver gathers, common midpoint gathers, and constant offset sections.

As seen in Figure 2.1, an individual common shot gather can be parameterized by the receiver location r. If two raypaths between the same source and receiver exist such that they have the same receiver ray parameter p_r and the two-way traveltime along each is the same, it is impossible to distinguish between the two reflector locations (Nolan and Symes, 1996). Figure 2.2 shows a very simple case of this so-called multipathing.

Figure 2.1 also shows that an individual common offset gather can be parameterized by midpoint m. Suppose that the midpoint ray parameter $p_m = p_s + p_r$ is the same for two raypaths with the same traveltimes. Once again, the two raypaths represent the same data space event, and the location of the reflector causing this event is ambiguous. Figure 2.3 shows a case of multipathing where $p_{s1} = -p_{r1}$ and $p_{s2} = -p_{r2}$ so that $p_{m1} = p_{m2} = 0$.

These simple cases clearly show that processing that uses these surface-related domains can be easily tricked. If we limit ourselves to the shot and offset domains, we may not be able to separate energy returning to the surface from different points in the subsurface. Even worse, we frequently want to try to extract additional information from the model, such as rock properties from amplitude analysis. If our analyses are carried out in surface-related coordinates such as offset, we will be seeing not only effects of multipathing, but less severe effects as the seismic energy passes through the subsurface between the surface and the point we have defined in terms of common midpoint. Relying on surface-related coordinates puts our analysis at the mercy of the accuracy of our subsurface model, which was built based on imaging methods using the surface-related coordinates itself. Fortunately, we can turn to a *subsurface-related* domain: the reflection angle domain.

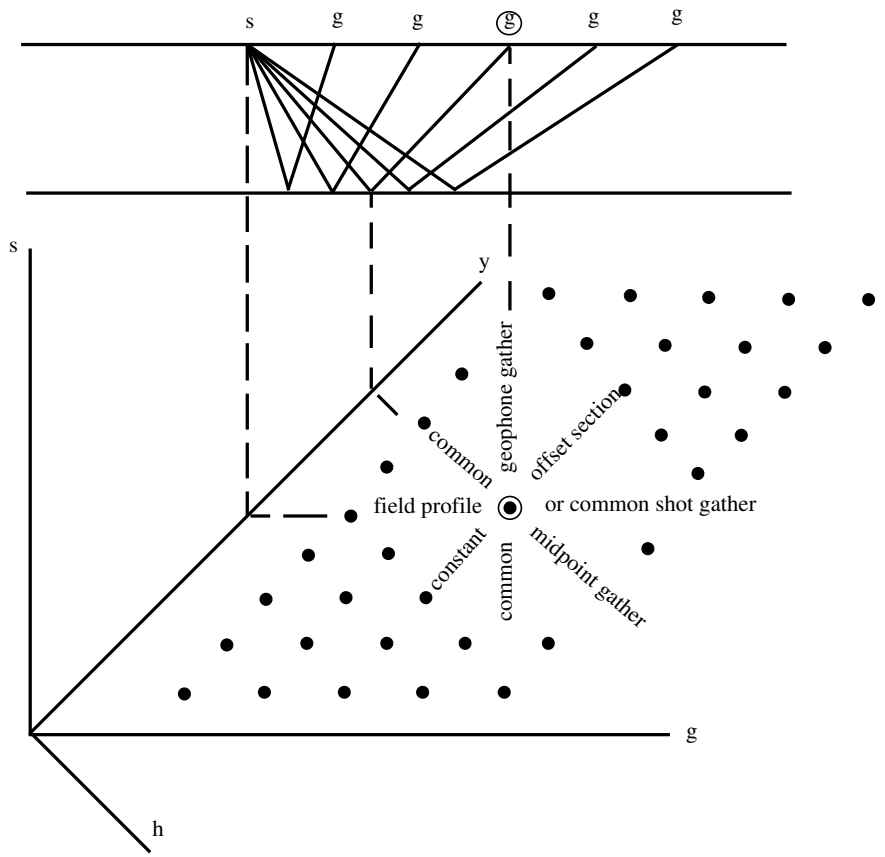

Figure 2.1: The relationships of the *surface-related* parameters source (s) and receiver (g) locations, and their sections and gathers. The top part shows a simple survey geometry over a single flat subsurface reflector: the single source (s) is connected to each receiver (g) by rays that reflect at the flat reflector. The lower part shows various ways we can arrange the data based on the relation of the shot and receiver. The axes are labeled to indicate the source location (s), receiver location (g), offset (h) which is the difference between the receiver and shot locations ($h = g - s$), and the midpoint location (y), which is halfway between the source and receiver ($y = (s+g)/2$). (From Claerbout (1995)) angdom-sg [NR]

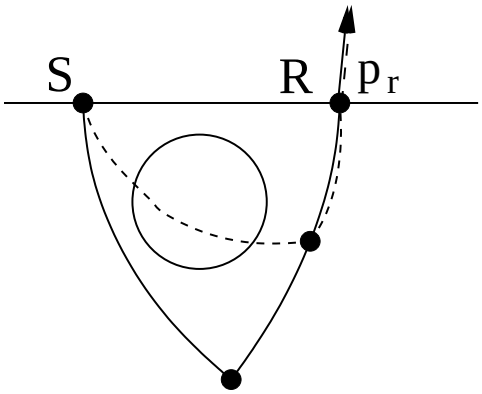

Figure 2.2: Raypaths through a fairly simple velocity model consisting of a weak vertical velocity gradient and a strong low velocity lens. An individual shot gather will contain energy that travels along both of these raypaths. The low velocity lens allows both traveltimes and receiver ray parameters p_r to be identical. angdom-shot1 [NR]

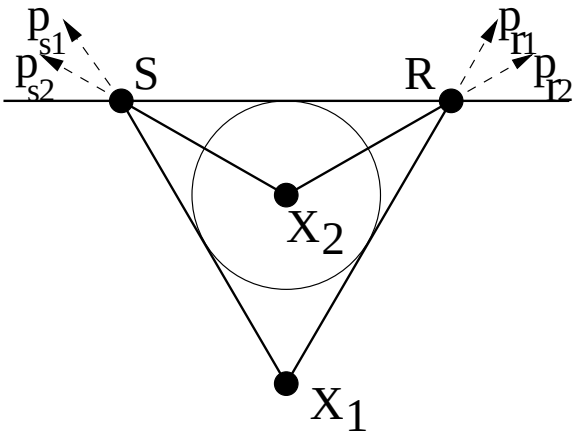

Figure 2.3: Raypaths through a simple constant velocity velocity model with a low velocity lens. An individual common offset gather will contain energy that travels along both of these raypaths. The arrivals will have identical traveltimes and midpoint ray parameters. angdom-offset1 [NR]

SUBSURFACE-RELATED DOMAIN: REFLECTION ANGLE

In complex areas, it is clear that we need to operate in a different domain, one that is related to the subsurface. Several authors have suggested angle-domain imaging as a solution for the reflector ambiguity (Xu et al., 1998; Prucha et al., 1999; Brandsberg-Dahl et al., 1999). This subsurface-related domain has many benefits. Since we are dealing with the model itself through the reflection angles rather than some approximation in surface-related coordinates, we are more likely to be able to get accurate rock properties. For example, amplitude variation with angle (AVA) analysis is more likely to be reliable than amplitude variation with offset (AVO) analysis. Velocity analysis in the reflection angle domain produces better velocity models and multiple arrivals can also be dealt with well (Sava and Guitton, 2003). Additionally, I will argue below that an event in an angle section uniquely determines a ray couple, which in turn uniquely locates the reflector. Thus imaging artifacts due to multipathing are eliminated in this domain.

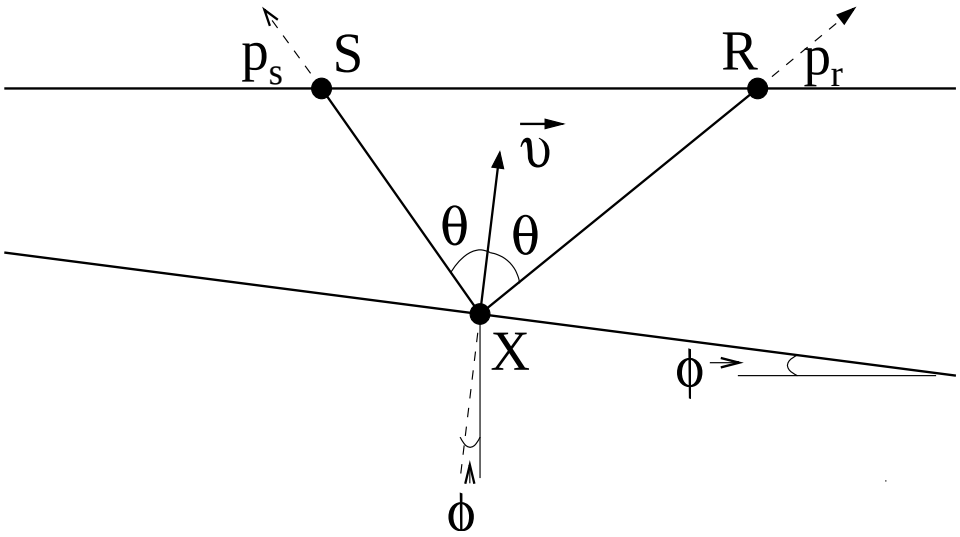

Figure 2.4: Defining the angle domain. The reflector element is completely defined by its subsurface location **x** and its dip vector ν. This reflector element will be represented at the surface by an event element defined by s, p_s, r, p_r, t, the source position, source ray parameter, receiver position, receiver ray parameter, and two way travel time, respectively. The connection of the reflector element to the event element comes from the incident and reflected rays that define the opening angle θ. angdom-rangle2 [NR]

For this discussion of multipathing I will limit the model to 2-D; it is similar in 3-D, with additional considerations such as azimuth. In Figure 2.4, consider a reflector element in the subsurface. This reflector element is completely defined by its subsurface location **x** and a dip vector ν that is normal to the dip of the reflector ϕ at that point. This reflector element will be represented at the surface by an event element defined by s, p_s, r, p_r, t, which are the source position, source ray parameter, receiver position, receiver ray parameter, and two way travel time, respectively. The connection of the reflector element to the event element comes from the incident and reflected rays that define the opening angle θ.

Given the definition of the reflector element, event element, and opening angle, we can state that an event in an angle (θ) gather cannot be duplicated by multipathing. To do this, I assume the *Traveltime Injectivity Condition* (ten Kroode et al., 1994): a pair of rays and a total (two-way) travel time determines at most one reflector element. In that case, the event in the angle domain is compatible with at most one reflector element ($\mathbf{x}, \nu$). A more rigorous discussion of the absence of multipathing in the angle domain has been done by Stolk and Symes (2002).

SEISMIC WAVE PROPAGATION

From the discussion of kinematics just seen, it is clear that the presence of artifacts will be diminished by carrying out processing in the angle domain. Understanding the kinematics allows us to develop methods to image the subsurface based on the idea of "reversing" seismic wave propagation. Before we can explore imaging methods in the angle domain, we must first review some basic equations for wave propagation in the subsurface. For simplicity, I will examine equations relating to the well-known 2-D acoustic case. A straightforward derivation of them can be found in Claerbout (1985).

The 2-D acoustic wave equation can be written as

$$\frac{\partial^2 P}{\partial t^2} = v^2 \left(\frac{\partial^2 P}{\partial x^2} + \frac{\partial^2 P}{\partial z^2} \right) \tag{2.1}$$

where P is the pressure wave traveling at time t through the subsurface defined by lateral

location x and depth z with velocity v.

We can now obtain the dispersion relation of the 2-D acoustic wave equation by substituting the trial solution

$$P = \exp(-i\omega t + i k_x x + i k_z z) \tag{2.2}$$

where ω is frequency, k_x is lateral wavenumber and k_z is vertical wavenumber to give us:

$$\frac{\omega^2}{v^2} = k_x^2 + k_z^2 \, . \tag{2.3}$$

Given this understanding of wave propagation through the subsurface, we can now explore methods of imaging the subsurface by "reversing" the propagation.

KIRCHHOFF MIGRATION METHODS

Kirchhoff methods using surface-related coordinates are well understood and have been used for decades (Berryhill, 1979; Schneider, 1978). The Kirchhoff equation that is the basis for Kirchhoff migration simply states that the wavefield at a given point $U(x,y,z,t)$ is a summation of waves propagating from other points at earlier times. When applied to migration in the *surface-related* domain, the Kirchhoff equation becomes the simple act of summing over the hyperbolas that are generated along the offset axis with different curvature depending on v.

When we turn to the subsurface-related angle domain, its kinematics make constructing a Kirchhoff type (summation) migration algorithm straightforward. Xu et al. (1998) described how to generate angle domain common image gathers (ADCIGs) in the depth domain by simply summing over all dip vectors ν for each point in the subsurface. Their methodology for creating an ADCIG from data recorded at the surface (d(s,r,t)) can be simply written as:

$$a(\mathbf{x},\theta) = \int d\nu w(\nu,\theta,\mathbf{x}) d(s,r,t) \tag{2.4}$$

where $a(\mathbf{x},\theta)$ is the ADCIG for reflection angle θ at subsurface position $\mathbf{x}$. The summation is over normal vectors ν (summing over all dips at position $\mathbf{x}$). The traveltimes used in this angle

domain Kirchhoff method vary with v. A weighting operator $w(v,\theta,\mathbf{x})$ that is dependent on the subsurface position and the dip and reflection angle at that position is applied to the data. This weighting operator handles issues such as amplitudes, that do not deal with the presence or absence of events. I refer you to Xu et al. (2001); Brandsberg-Dahl et al. (1999) for more detailed information on angle-domain Kirchhoff methods.

Problems with Kirchhoff methods

Although the simplicity of migration by Kirchhoff methods is attractive, many authors have demonstrated that Kirchhoff methods are not optimal for areas with complex subsurfaces (Geoltrain and Brac, 1993; O'Brien and Etgen, 1998). Stolk and Symes (2002) demonstrated that Kirchhoff methods in the angle domain may still have artifacts in strongly refracting media, even when using the correct velocity and all arrivals. The problem at the heart of the Kirchhoff methods is its high frequency assumption. The Kirchhoff equation explicitly assumes that the behavior of the seismic waves can be adequately described through the use of rays and that the image can be obtained by summing over a given number of these rays rather than using all of the energy present in the data. This assumption breaks down for very complex subsurfaces. Fortunately, other methods based on the wave equation do not have this high frequency assumption and do use all of the energy present in the data. In this thesis, the imaging method I will use is downward-continuation migration.

DOWNWARD-CONTINUATION MIGRATION METHODS

Recent advances in computing power make it practical for us to use downward-continuation methods that are more computationally expensive than Kirchhoff methods. Stolk and Symes (2002) showed that wave equation methods do not suffer from any of the artifacts related to multipathing that are seen in the offset domain or the artifacts seen in angle-domain Kirchhoff methods. In this section, I will explain how I perform migration with downward continuation and how I generate angle-domain common image gathers (ADCIGs) through slant stacking.

Downward continuation

Downward continuation is a process in which we "push" the data recorded at the surface down into the earth to obtain the wavefield at each depth in the subsurface. When we use the correct velocity to push the wavefield deeper, energy that was reflected at some point in the subsurface gets moved back to the reflection point [1]. The process of downward continuation is essentially a phase shift applied to the wavefield recorded at the surface (U_{z0}) (Claerbout, 1985) so that it becomes the wavefield at some depth (U_z). This is expressed mathematically as:

$$U_{z+\Delta z} = e^{ik_z \Delta z} U_z \tag{2.5}$$

where k_z can be found from the dispersion relation (equation (2.3)). Rearranging equation (2.3), we find that:

$$k_z = \sqrt{\frac{\omega^2}{v^2} - k_x^2} \tag{2.6}$$

which you may recognize as the Single Square Root (SSR) equation. This equation is only valid for constant velocity or velocity that varies only with depth. The inability to handle lateral velocity variations makes this equation not directly applicable in complex areas. To be able to handle lateral velocity variations, we first need to handle the source and receiver wavefields separately.

Fortunately, the SSR equation can be modified to handle the source and receiver wavefields separately. This modification is called the Double Square Root (DSR) equation (equation (2.7)):

$$k_z = \sqrt{\frac{\omega^2}{v(\mathbf{s},z)^2} - \frac{1}{4}\left[\left(k_{m_x} - k_{h_x}\right)^2 + \left(k_{m_y} - k_{h_y}\right)^2\right]}$$

[1] This is a simplification: if the earth has a strong velocity gradient with depth, the seismic energy will actually overturn and simple downward continuation will not move the energy to its true reflection point. This energy becomes evanescent and disappears.

$$+ \quad \sqrt{\frac{\omega^2}{v(\mathbf{r},z)^2} - \frac{1}{4}\left[\left(k_{m_x}+k_{h_x}\right)^2 + \left(k_{m_y}+k_{h_y}\right)^2\right]} \tag{2.7}$$

which is the 3-D equation where k_{m_x} and k_{m_y} are the midpoint horizontal wavenumbers and k_{h_x} and k_{h_y} are the offset horizontal wavenumbers. The velocities $v(\mathbf{s},z)$ and $v(\mathbf{r},z)$ are the velocities at a given depth that are associated with the downward-continued source and receiver wavefields, respectively. The $v(\mathbf{s},z)$ and $v(\mathbf{r},z)$ allow us to have subsurface models with laterally varying velocities [2].

When the DSR equation is used to obtain the prestack wavefield at depth ($U(\omega,\mathbf{m},\mathbf{h};z)$) and the velocities used for the downward continuation are correct, the result is to collapse all of the energy to zero-offset. If we were only interested in the zero-offset information, we could then extract an image from the downward-continued wavefield at zero time:

$$U(\omega,\mathbf{m},\mathbf{h};z=0) \quad \stackrel{\text{DSR}}{\Longrightarrow} \quad U(\omega,\mathbf{m},\mathbf{h};z) \tag{2.8}$$

$$U(\omega,\mathbf{m},\mathbf{h};z) \quad \stackrel{Imaging}{\Longrightarrow} \quad U(t=0,\mathbf{m},\mathbf{h};z). \tag{2.9}$$

However, since this image will only contain the zero offset information (left panel in Figure 2.5), it has limited diagnostic information for velocity updating, and no information on the amplitude variation with reflection angle (AVA). If we extract the image at this point only, we are losing valuable information that exists in the data.

Slant stacking

To take advantage of the information that non-zero offsets provide, we can perform a slant stack (Schultz and Claerbout, 1978) along the offset axis at each depth step before imaging. In this way we obtain an image as a function of the offset ray parameters p_{hx} and p_{hy}:

[2] This DSR equation is a simplification of what is done in practice. Algorithms for downward continuation require so-called reference velocities to be picked for each depth step rather than using the "true" velocities and interpolation. These migration schemes are known as Phase Shift Plus Interpolation (Stoffa et al., 1990).

$$U(\omega,\mathbf{m},\mathbf{h};z=0) \overset{\text{DSR}}{\Longrightarrow} U(\omega,\mathbf{m},\mathbf{h};z) \tag{2.10}$$

$$U(\omega,\mathbf{m},\mathbf{h};z) \overset{\textit{Slant stack}}{\Longrightarrow} U(\tau,\mathbf{m},\mathbf{p_h};z) \tag{2.11}$$

$$U(\tau,\mathbf{m},\mathbf{p_h};z) \overset{\textit{Imaging}}{\Longrightarrow} U(\tau=0,\mathbf{m},\mathbf{p_h};z). \tag{2.12}$$

With this method we can extract angle-domain common image gathers (CIGs) from the new wavefield $U(\tau=0,\mathbf{m},\mathbf{p_h};z)$ at fixed midpoint locations (Prucha et al., 1999). The right panel in Figure 2.5 shows the angle-domain CIG corresponding to the downward-continued offset gather shown in the left panel. By downward continuing the wavefields with the DSR equation and slant stacking at every depth step, this method can handle lateral velocity variations, unlike the slant stacking method proposed by Ottolini and Claerbout (1984).

Strictly speaking, the CIGs obtained by this procedure are function of the offset ray parameters $\mathbf{p_h}$ and not of the opening angle θ. However, in 2-D p_{hx} is linked to θ by the following simple trigonometric relationship (a similar relationship can be found for the 3-D problem):

$$\frac{\partial t}{\partial h} = p_{hx} = \frac{2\sin\theta\cos\phi}{V(z,m)}, \tag{2.13}$$

where ϕ is the geological dip along the in-line direction and $V(z,m)$ is the velocity function. A rigorous treatment of CIGs in 3-D can be found in Biondi (1999).

Sava et al. (2001) demonstrated that it is possible to perform downward-continuation migration in such a way as to get CIGs that have an axis of reflection angle rather than offset ray parameter. This method of obtaining CIGs is based on the relationship between the reflection angle θ and the local subsurface offset as

$$\tan\theta = \frac{k_h}{k_z} \tag{2.14}$$

where k_h is the local subsurface offset wavenumber. Since the offset involved in their methodology is related to the subsurface rather than the surface, the CIGs produced will be free of many of the artifacts seen in CIGs from surface related techniques.

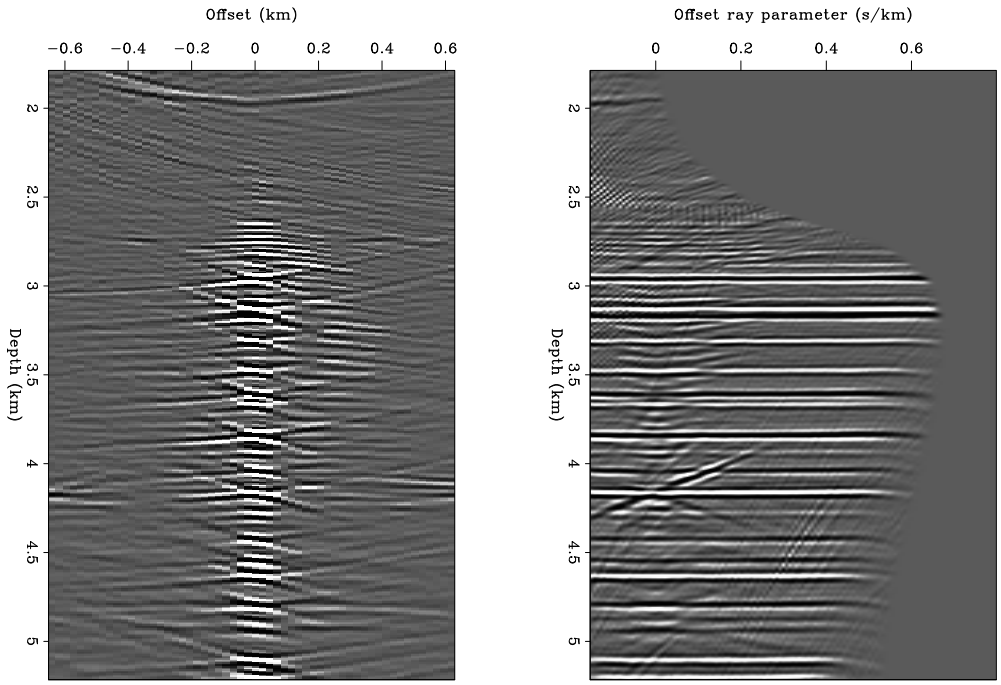

Figure 2.5: Left: Offset panel after downward continuation. Right: Angle-domain CIG angdom-hcig.pcig [CR]

Problems in ADCIGs

Although the angle domain allows us to avoid multipathing, in complex media it will still be plagued by problems such as poor illumination. Poor illumination can be caused by energy being lost by leaving the survey area, energy becoming evanescent at boundaries such as salt interfaces, and focusing/defocusing caused by the complex overburden. In the angle domain, energy leaving the survey may do so at some middle range of reflection angles. Figure 2.6 demonstrates this with raytracing through a simple velocity model provided by The Rice Inversion Project. The maximum offset recorded in this model is 3000 meters, so rays that are separated by more than 3000 meters at the surface represent energy that is lost. The velocity model consists of one horizontal layer beneath a strong low velocity lens. It is clear that some of the energy is leaving the bounds of the survey. This will result in the shadow zones in the common ray parameter section and the holes in the angle domain CIG seen in Figure 2.7. The poor illumination can be seen most clearly in the depth slice (top panel of Fig. 2.7). If there

were no illumination problem, the triangle would be solid black. The white streaks through the triangle are caused by the lost energy.

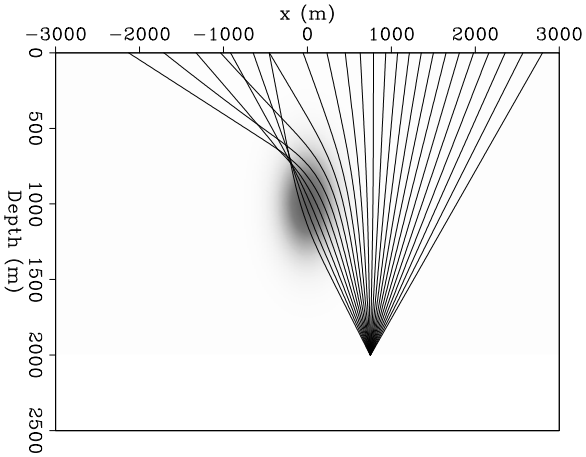

Figure 2.6: Raytracing through a velocity model with a strong low velocity lens. The maximum offset recorded in this model is 3000 meters, so rays that are separated by more than 3000 meters at the surface represent energy that is lost. angdom-symesray [ER]

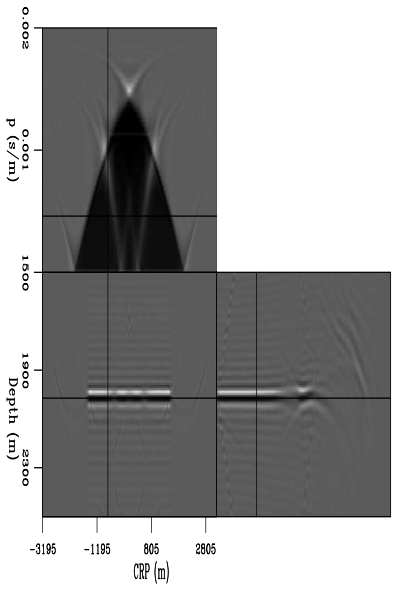

Figure 2.7: Migration result from the velocity model shown in Figure 2.6. The common p_{hx} section (left panel) has shadow zones positive and negative 600m in CRP. The ADCIG (right panel) has clear "holes" in the events caused by energy leaving the bounds of the survey, as demonstrated by Figure 2.6. The depth slice (top panel) shows the illumination problem as white streaks through the black triangle. angdom-holey [CR]

Chapter 3

Imaging by inversion

In the previous chapter I explained that the common image gathers that can be obtained from downward-continuation migration are more likely to have fewer artifacts, particularly those caused by multipathing, than other migration methods. Unfortunately, in areas where the subsurface is very complex, especially in areas of strong velocity contrasts such as near salt bodies, migration can not provide a complete model due to poor illumination. In this chapter I will explain how to use downward-continuation migration as an operator in an iterative least-squares inversion scheme. I will also explain how I stabilize the inversion by regularizing the output model.

DOWNWARD-CONTINUATION MIGRATION AS AN IMAGING OPERATOR

Migration is an operator that generates a subsurface model from recorded seismic data. In this section I will explain that migration is an adjoint operator. I will also explain that migration can be used along with its forward operator in an inversion process to create a subsurface image that is superior to that from migration alone.

Adjoint vs. inverse operators

When collecting seismic data, we are injecting seismic energy into the earth which propagates to some point in the subsurface and reflects back to the surface. To create a model of the subsurface, we want to reverse this process. There are two different ways to go through this reversal: with an adjoint operation or with an inverse operation. The downward-continuation migration described in the previous chapter is an adjoint to seismic wave propagation, not an inverse. Claerbout (1995) explains that an adjoint is a matrix transpose. This means that it is an approximation that is not able to accurately "undo" the wave propagation, especially in complex areas. In such areas, the adjoint operator will be unable to account for seismic energy that leaves the survey area or becomes evanescent. In the case of the downward-continuation migration used in this thesis, overturned rays are not properly handled. If we use the inverse operation, which is more computationally expensive than an adjoint operation, it will do a better job of reversing the propagation. However, applying the true inverse is computationally infeasible for the huge matrices we face in seismic imaging. Fortunately, we can make the adjoint more like an inverse through a least-squares scheme, which will not be as computationally intensive as a true inverse.

Least-squares inversion

In order to approximate the inverse of seismic wave propagation, we can use the migration operator in a least-squares inversion problem (Nemeth et al., 1999; Duquet and Marfurt, 1999). The seismic wave propagation is a linear operator (**L**) which gives us the seismic data (**d**) from the ideal subsurface model (**m**) as seen by:

$$\mathbf{d} = \mathbf{L}\mathbf{m}. \tag{3.1}$$

Once again, a migration operator such as downward-continuation migration is the adjoint of the wave propagation ($\mathbf{L}'$). A direct least-squares solution for the model from this equation is

$$\left(\mathbf{L}'\mathbf{L}\right)^{-1}\mathbf{L}'\mathbf{d} \;=\; \mathbf{m}. \tag{3.2}$$

However, the size of the seismic imaging problem makes it unreasonable to invert $\left(\mathbf{L}'\mathbf{L}\right)$ directly. Fortunately, we can approximate the inverse by using $\mathbf{L}'$ and $\mathbf{L}$ in an iterative conjugate-gradient scheme. This amounts to minimizing the objective function:

$$min\{Q(\mathbf{m}) \;=\; ||\mathbf{L}\mathbf{m}-\mathbf{d}||^2\}. \tag{3.3}$$

I choose to write this equation in a more intuitive form known as a fitting goal:

$$\mathbf{0} \;\approx\; \mathbf{L}\mathbf{m}-\mathbf{d} \tag{3.4}$$

Given this formulation of the imaging problem, it is interesting to consider its relationship to the illumination problems discussed in the previous chapter. Essentially, the shadow zones are related to the null space of the inversion. We are missing elements of the data (**d**) that correspond to certain reflection angles at certain subsurface locations. Model locations that correspond to the null space in the data can fill with noise, possibly causing the inversion to diverge.

REGULARIZED LEAST-SQUARES INVERSION

Regularized inversion

To stabilize the inversion, I use a form of Tikhonov regularization (Tikhonov and Arsenin, 1977). This makes the objective function:

$$min\{Q(\mathbf{m}) \;=\; ||\mathbf{W}(\mathbf{L}\mathbf{m}-\mathbf{d})||^2+\epsilon^2\,||\mathbf{A}\mathbf{m}||^2\}. \tag{3.5}$$

A is the regularization operator, and the parameter ϵ is a Lagrange multiplier that allows us to determine how strong our regularization will be. Note that I have also added the weighting

function **W**. By using an iterative approach, we can create **W** in such a way as to allow us to "expand" the data space so that the "new" events we generate in the model space with the regularization can be propagated to points outside of the true survey geometry, essentially allowing us to keep this energy in the iterative inversion scheme. **W** can also allow us to include the Jacobian (Sava and Biondi, 2001) so that the amplitudes of the events are correct.

This objective function can be written in terms of the more intuitive fitting goals:

$$\mathbf{0} \approx \mathbf{W}(\mathbf{Lm} - \mathbf{d}) \tag{3.6}$$

$$\mathbf{0} \approx \epsilon \mathbf{Am}. \tag{3.7}$$

The first fitting goal is the "data fitting goal," meaning that it is responsible for making a model that is consistent with the data. The second fitting goal is the "model styling goal," meaning that it allows us to impose some idea of what the model should look like using the regularization operator **A**. If we iterate until convergence, solving both fitting goals at the same time, the data fitting goal will prevent the regularization from creating anything in the model that conflicts with the recorded data. The regularization of the model will prevent the noise in the null space of the inversion from blowing up, helps clean up artifacts, and helps to fill in the shadow zones. Unfortunately, **A** is generally a poorly conditioned matrix, thereby making the iterative inversion converge slowly.

Regularized Inversion with model Preconditioning (RIP)

To speed the convergence of the inversion, we can reformulate the inversion problem as a Regularized Inversion with model Preconditioning (RIP) through the use of a preconditioning operator **S**. This operator should be as close to the inverse of the regularization operator as possible so that $\mathbf{AS} \approx \mathbf{I}$. By mapping the multi-dimensional regularization operator **A** to helical space and applying polynomial division, we can apply the exact inverse so that $\mathbf{S} = \mathbf{A}^{-1}$ (Claerbout, 1998). We also use the preconditioning transformation $\mathbf{m} = \mathbf{Sp}$ (Fomel et al., 1997). My objective function then becomes:

$$min\{Q(\mathbf{p}) \;=\; ||\mathbf{W}(\mathbf{LSp}-\mathbf{d})||^2+\epsilon^2\;||\mathbf{Ip}||^2\}. \tag{3.8}$$

In fitting goals this is:

$$\mathbf{0} \;\approx\; \mathbf{W}(\mathbf{LSp}-\mathbf{d}) \tag{3.9}$$

$$\mathbf{0} \;\approx\; \epsilon\mathbf{Ip}. \tag{3.10}$$

Now the model styling goal contains the identity operator **I**, which is very well conditioned. This will allow the iterative inversion to converge faster.

Regularization schemes and operators

To choose a regularization (**A**) operator, we must decide what we expect the model to look like. Ideally, **A** should be the inverse model covariance (Tarantola, 1986). The model space generated by my downward-continuation migration method is a cube with the axes depth (z), common reflection point (CRP), and offset ray parameter (p_h) for a 2-D dataset. For a 3-D dataset, this model space becomes five dimensional, with axes of z, CRP_x, CRP_y, p_{hx} and p_{hy}. We can expect seismic events to behave in particular ways along these axes.

Assuming that the correct velocity model was used by the migration operator, events along the p_h axis should be horizontal with no moveout, as seen in Figure 3.1. This figure shows the downward-continuation migration result of a subset of the SMAART JV Sigsbee2A dataset. The corresponding correct velocity model can be seen in Figure 3.2, which is the stratigraphic model that the velocity models in Figures 1.1 and 1.2 are based on. Those figures include raytracing to demonstrate the illumination problems beneath the salt edge, which can be seen as a decrease in amplitudes in the oval shown in Figure 3.1. In addition to the expected flat events along p_h, we can assume that the reflectivity (seismic amplitude) along reflection angles should vary smoothly (Shuey, 1985; Richter, 1941), and any sudden changes in amplitude are caused by illumination problems, as explained in the previous chapter and indicated in

Figure 3.1 by arrows. Since we believe the model should vary smoothly as a function of angle, we would expect the amplitude difference as a function of angle to be small, meaning that we can simply minimize the model styling goal using a derivative operator as the regularization operator. This is my *geophysical regularization* scheme, and is denoted as $\mathbf{A_f}$.

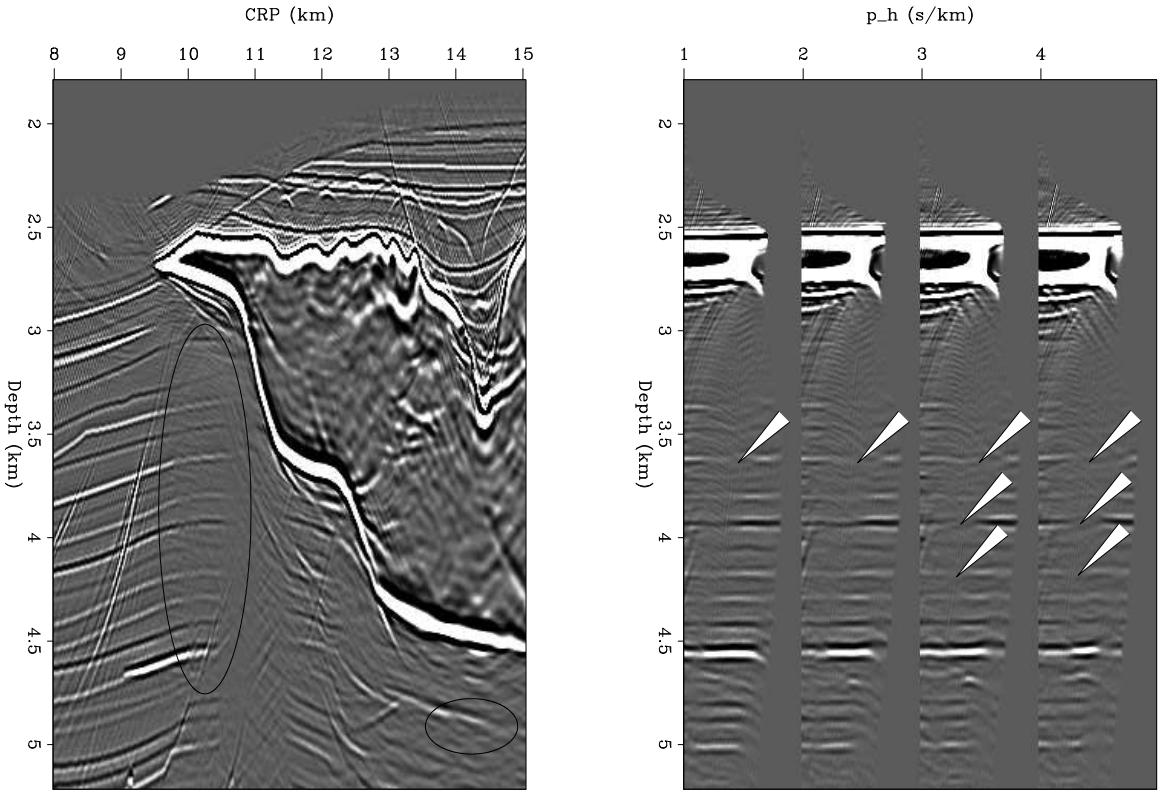

Figure 3.1: Downward continuation migration result for part of the Sigsbee2A model. Left: common offset ray parameter section. Ovals indicate interesting areas of poor illumination. Right: four CIGs taken from between CRP 10.0 km and 10.25 km. Arrows indicate holes in the events. precop-zig.mig [CR]

We may also have a good idea of the way seismic events should behave in the CRP-depth plane. An interpreter can pick horizons from a migration result, and can even extend the horizons into areas of poor illumination. Alternatively (or additionally), we might have a good geologic model of the subsurface. We also know that the amplitudes along the events really shouldn't decrease suddenly when the reflectors enter a shadow zone such as that under salt, so we want to minimize this abrupt change. If we do have an interpretation or geologic model

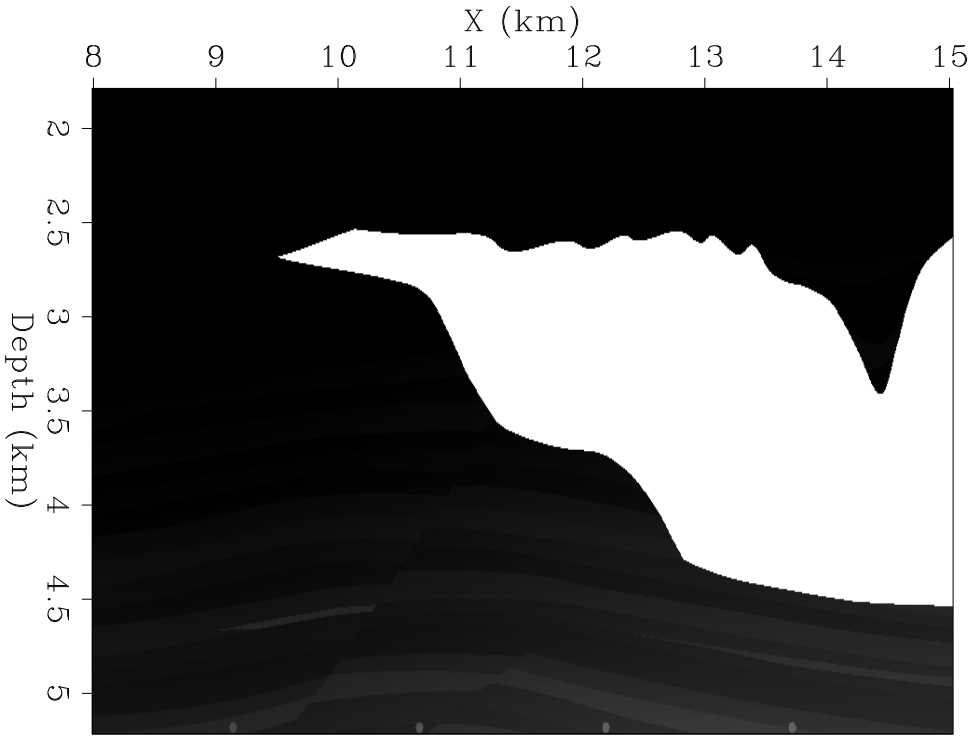

Figure 3.2: Velocity model for part of the Sigsbee2A model. precop-vel.corvel [ER]

we trust, we should be able to use this information to regularize the inversion in the CRP-depth plane. This is my *geological regularization* scheme, and is denoted as $\mathbf{A_l}$.

There are several operators that could be used to implement these regularization schemes, particularly the geophysical regularization scheme. One way to regularize the model along the p_h axis is simply to make $\mathbf{A_f}$ a derivative filter, which is a simple filter with two coefficients: "1 $-\rho$". ρ is a number less than or equal to 1, and helps to control the strength of the regularization. However, this may not provide a symmetrical effect on the amplitudes. By applying this filter and its mirror image "-ρ 1", a symmetrical response can be ensured. The result of using this type of filter for my geophysical regularized inversion with model preconditioning (RIP) for a part of the Sigsbee2A dataset can be seen in Figure 3.3. Note in particular the way the holes along the p_h axis are being filled in (indicated by the arrows) and how much cleaner the shadow zones are. The amplitudes inside the oval are more consistent. Another possible $\mathbf{A_f}$ is a steering filter composed of dip annihilator filters that act horizontally

(Clapp et al., 1997).

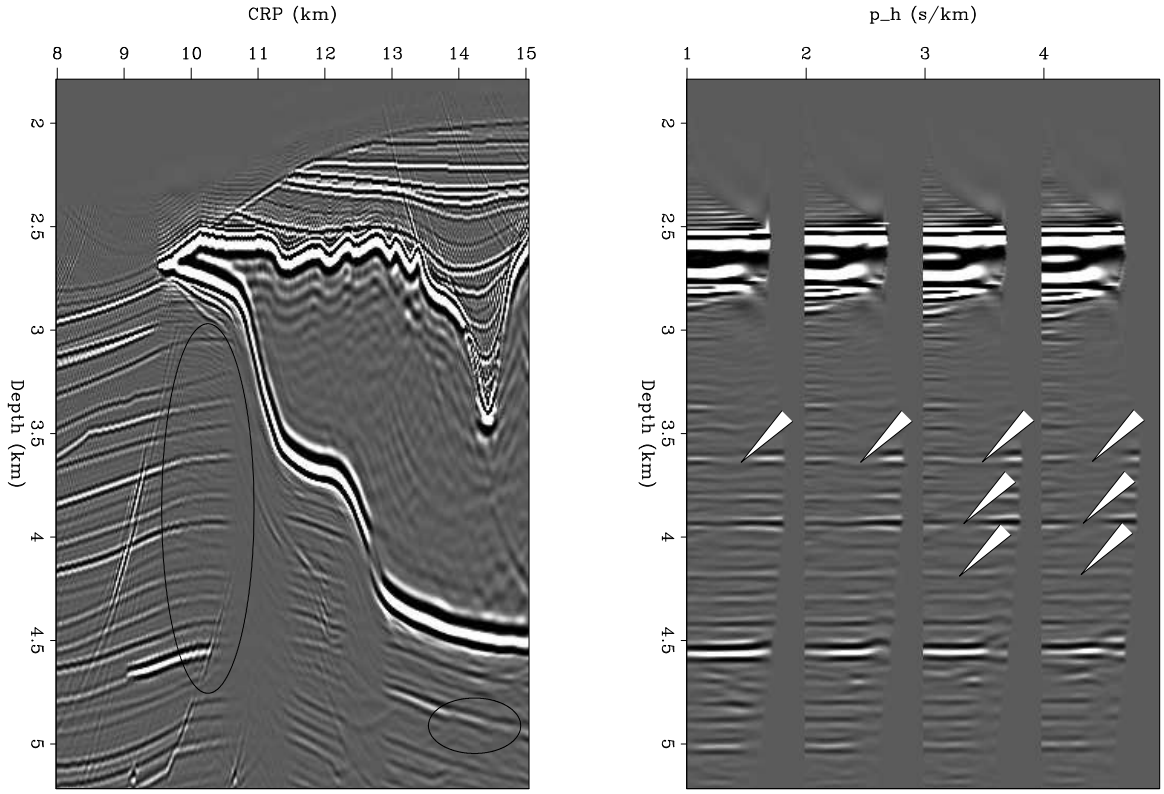

Figure 3.3: Result of 10 iterations of geophysical RIP for part of the Sigsbee2A model. Left: common offset ray parameter section. The amplitudes and continuity within the ovals is improved compared to Figure 3.1. Right: four CIGs taken from between CRP 10.0 km and 10.25 km. The holes indicated by the arrows are largely filled in. The artifacts that existed in the shadow zones are cleaned up. precop-zig.geop.10it [CR]

The versatility of the steering filter allows it to be used in ways other than just horizontal smoothing along the p_{hx} axis. It can also be used to implement the geological regularization scheme, meaning that it can act along predetermined dips in the CRP-depth plane. An interpretation of the structural events can be used to generate a dip annihilator filter at every model point. All of these individual dip annihilator filters are then combined together to make the steering filter itself. This steering filter will then attempt to honor the interpreter's ideas of what dips should exist, particularly in areas that are in shadow zones. I choose to combine this with the geophysical regularization, resulting in a regularization operator $\mathbf{A_f A_l}$. For simplicity, I will still refer to this combined regularization operator as geological regularization.

An example of reflectors picked from the migration result to be used in constructing a steering filter can be seen in Figure 3.4. For this case, I have not picked reflectors under the salt. As a result, the dip annihilator filters for each point in the model beneath the salt will match those at the salt bottom, i.e. the dips of the sediments beneath the salt are assumed to be similar to the dip of the salt bottom. The result of geological RIP using these reflectors on the small part of the Sigsbee2A dataset is in Figure 3.5. After 8 iterations, the holes in the CIGs are filled in and the amplitudes of the reflectors indicated by ovals are more consistent. The area under the salt shows that where the dip of the salt bottom is low, the dip of the subsalt sediments is similar and therefore the events are enhanced. Where the salt bottom has a steep dip, the subsalt sediments do not match that dip and therefore the events are wiped out - the data do not support the dips proposed by the model regularization.

Since this is a synthetic model, we can also pick the exact reflectors from the reflectivity model. I have overlaid these reflectors on the migration model in Figure 3.6. The result of 8 iterations of geological RIP using these reflectors can be seen in Figure 3.7. Comparing this result with Figure 3.5, note in particular the more anticlinal behavior of the events between $CRP = 9.5km$ and $CRP = 12.5km$. The shadow zones are partially filled in, in a reasonable way, as compared to both the migration result (Fig. 3.1) and the geophysical RIP result (Fig. 3.3). In the common image gathers (right panels of figures already referred to), both of the geological RIP results have entirely filled the gaps indicated by the arrows, but the result using the reflectors from the reflectivity model has improved the amplitudes of other events as well. It is clear that geological RIP can improve the image, particularly when the picked reflectors are accurate.

We also must choose an ϵ. A large ϵ means that the regularization will be strong (we will be enforcing our idea of the model more) and a small ϵ means the regularization is not strong (we rely on the data more). Choosing a balanced ϵ will help to fill the null space in a reasonable way.

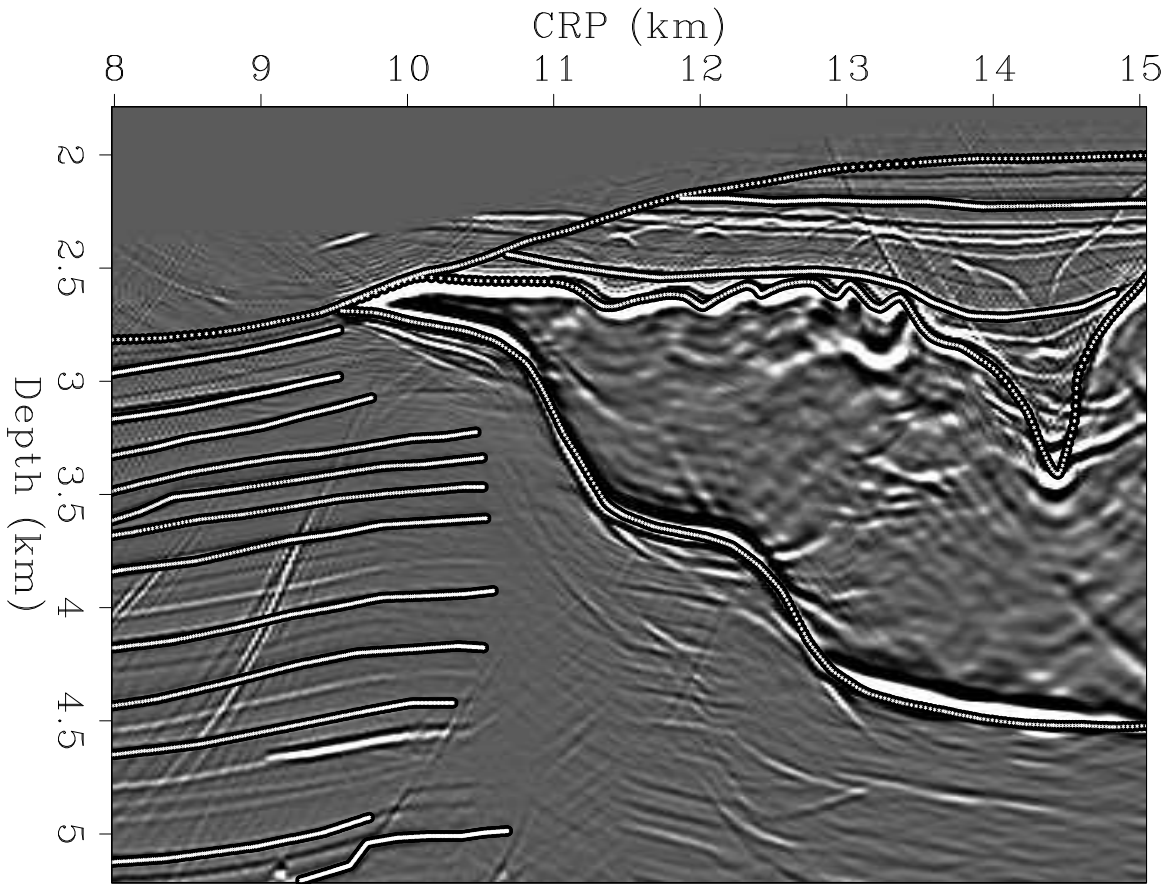

Figure 3.4: Reflectors picked from the migration result for part of the Sigsbee2A model, overlaid on the stack of the migration result. precop-reflectors [CR]

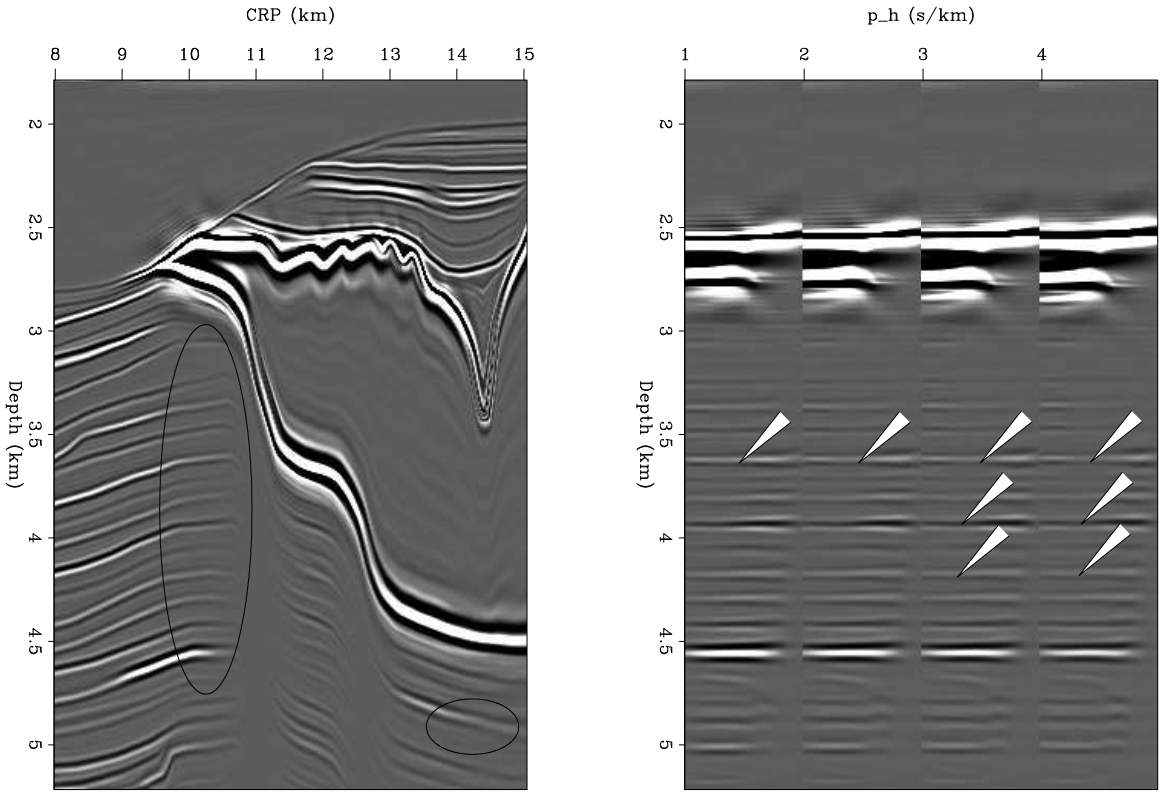

Figure 3.5: Result of 8 iterations of geological RIP for part of the Sigsbee2A model. Left: common offset ray parameter section. The amplitudes and continuity within the ovals is improved compared to Figure 3.1 and Figure 3.3. Right: four CIGs taken from between CRP 10.0 km and 10.25 km. The holes indicated by the arrows are completely filled in. precop-zig.geol.8it [CR]

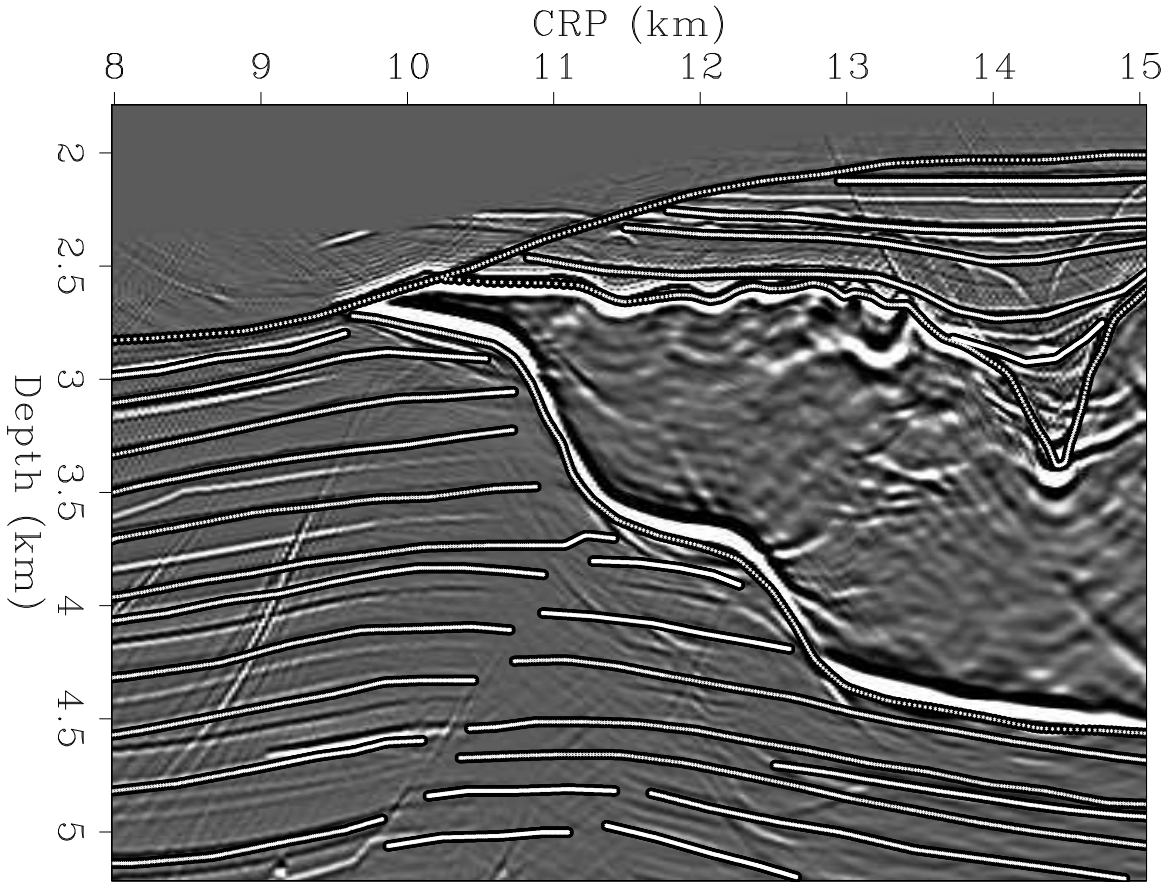

Figure 3.6: Reflectors picked from the actual reflectivity model for part of the Sigsbee2A model, overlaid on the stack of the migration result. precop-refsreflect [CR]

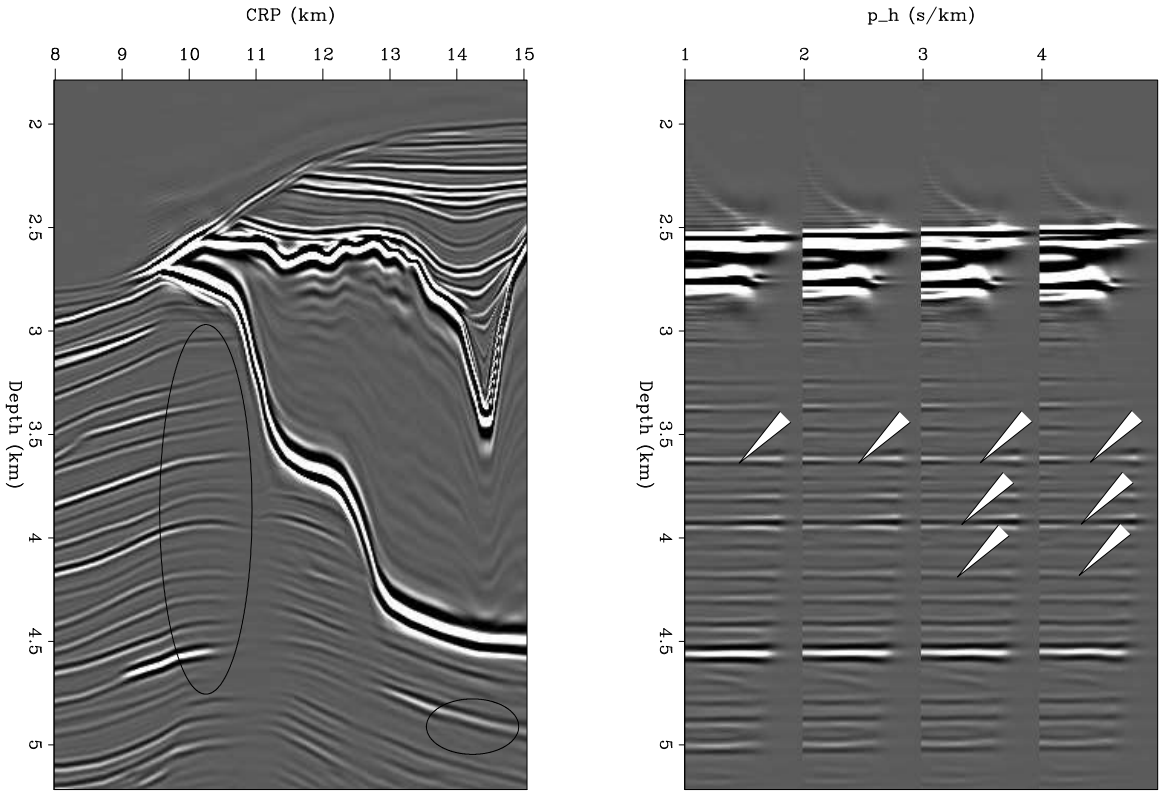

Figure 3.7: Result of 8 iterations of geological RIP for part of the Sigsbee2A model, using the reflectors picked from the actual reflectivity model. Left: common offset ray parameter section. The amplitudes and continuity within the ovals is improved compared to Figure 3.1 and Figure 3.3. Right: four CIGs taken from between CRP 10.0 km and 10.25 km. The holes indicated by the arrows are completely filled in. precop-zig.geolall.8it [CR]

Effects of model regularization on the data space

The model regularization schemes I am proposing are designed to compensate for the seismic energy that is lost due to complex subsurfaces. Much of the energy is lost because it is directed outside of the bounds of the seismic survey. The regularized model is in essence expanding the data space through the data fitting goal (3.6). To demonstrate this, I use the simple synthetic dataset with a single reflector below a low velocity lens. The velocity model can be seen in Figure 2.6 and the result of downward-continuation migration is in Figure 3.9. The actual synthetic data can be seen in Figure 3.8. The data is displayed as a flattened cube with a time slice at the top, a common offset panel in the lower left and a common midpoint (CMP) gather in the lower right. The triangular shape of the data as viewed in the time slice is caused by the finite extents of the survey. The missing energy that has left the bounds of the survey is manifested as holes in the CIGs as seen in the migration result (Figure 3.9). Theoretically, if the survey was larger in extent, this energy would be recorded and the migration would not have holes.

Regularized inversion with model preconditioning (RIP) tries to create a model in which we compensate for the lost seismic energy. In this case, we are in essence reconstructing the energy that leaves the survey bounds. Performing 3 iterations of geophysical RIP fills in the holes in the CIGs (Figure 3.10). To examine the effects of this on the data space, we apply the adjoint of downward-continuation migration to this result. Figure 3.11 shows the data space associated with the result of RIP. Comparing this with Figure 3.8, the triangular shape of the original data is still visible, but data has actually been extended beyond its original extents, albeit at a lower amplitude. Hence, model regularization is actually expanding the data space.

RIP IN PRACTICE

Regularized inversion with model preconditioning (RIP) can be used for any large inversion problem. In this section, I will explain how I have formulated it to best solve the problem of poor illumination in seismic imaging.

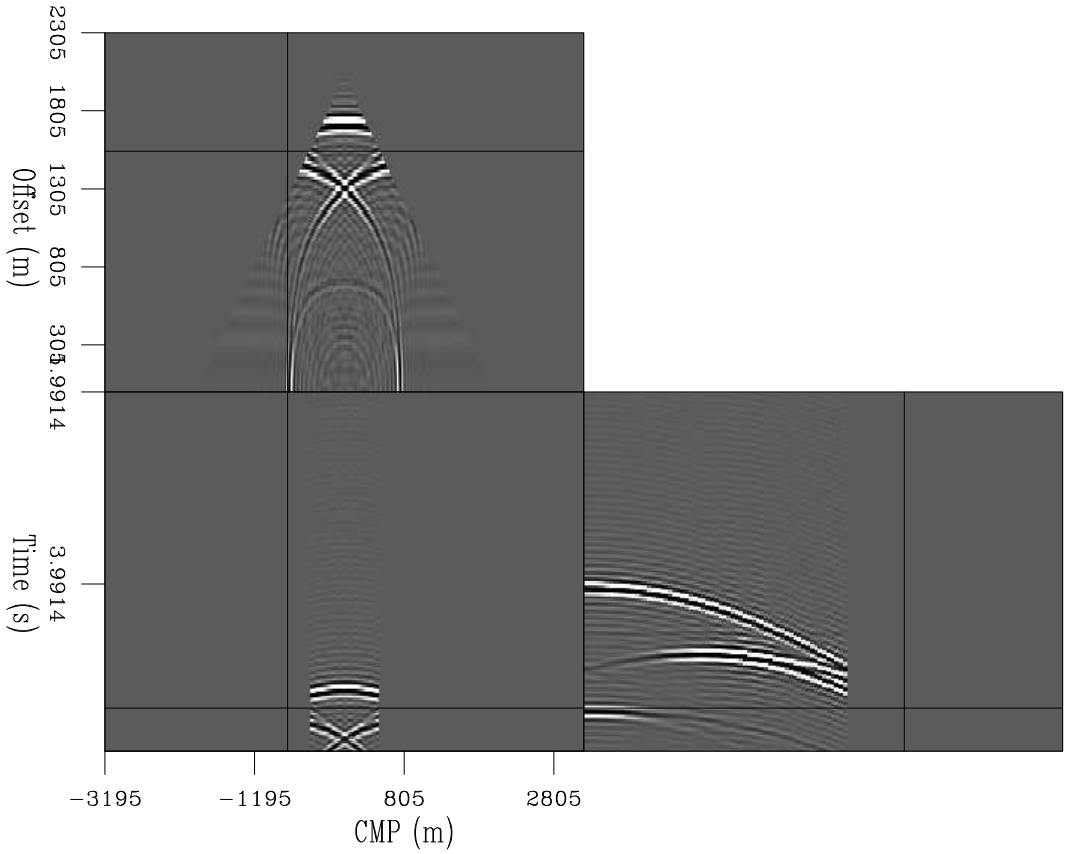

Figure 3.8: The recorded data corresponding to a synthesized seismic survey over the velocity model in Figure 2.6. The triangular shaped extent of the data seen in the time slice (top) is caused by the limited survey geometry. precop-dat.data [ER]

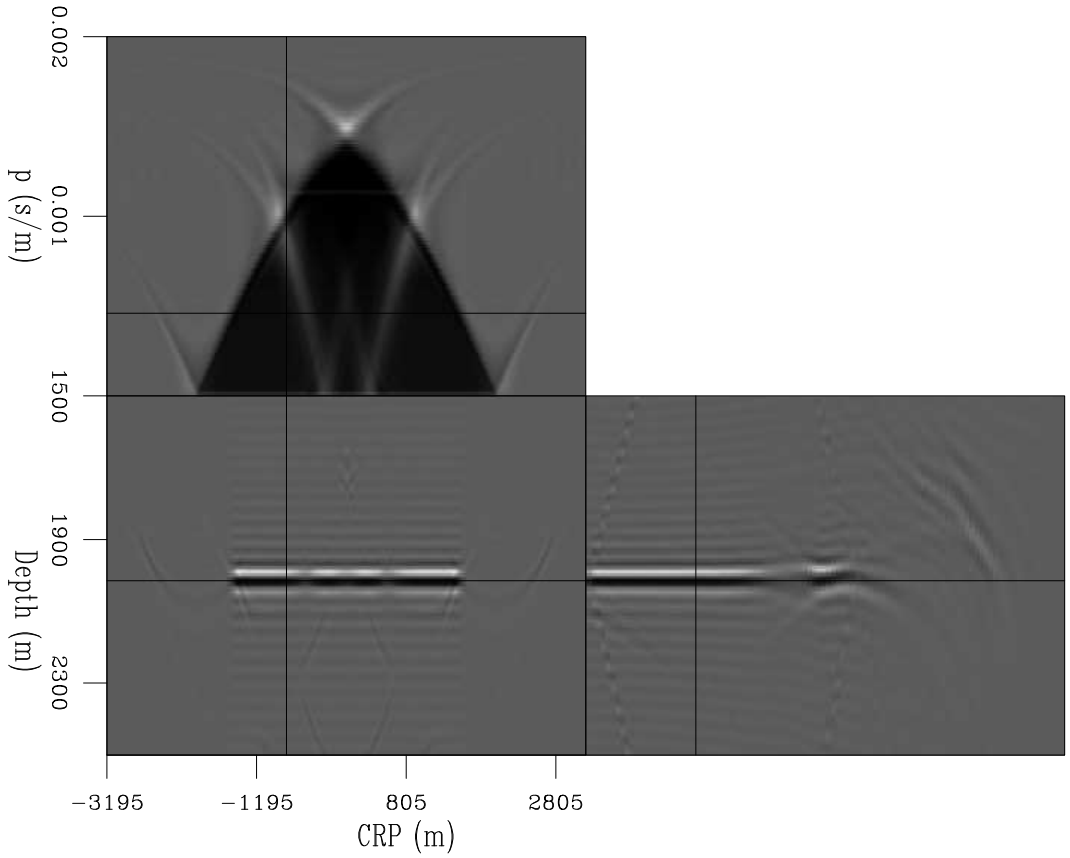

Figure 3.9: The result of migrating the data in Figure 3.8. Note the holes in the CIGs indicating poor illumination caused by seismic energy being directed outside of the survey area. precop-symes.mig [CR]

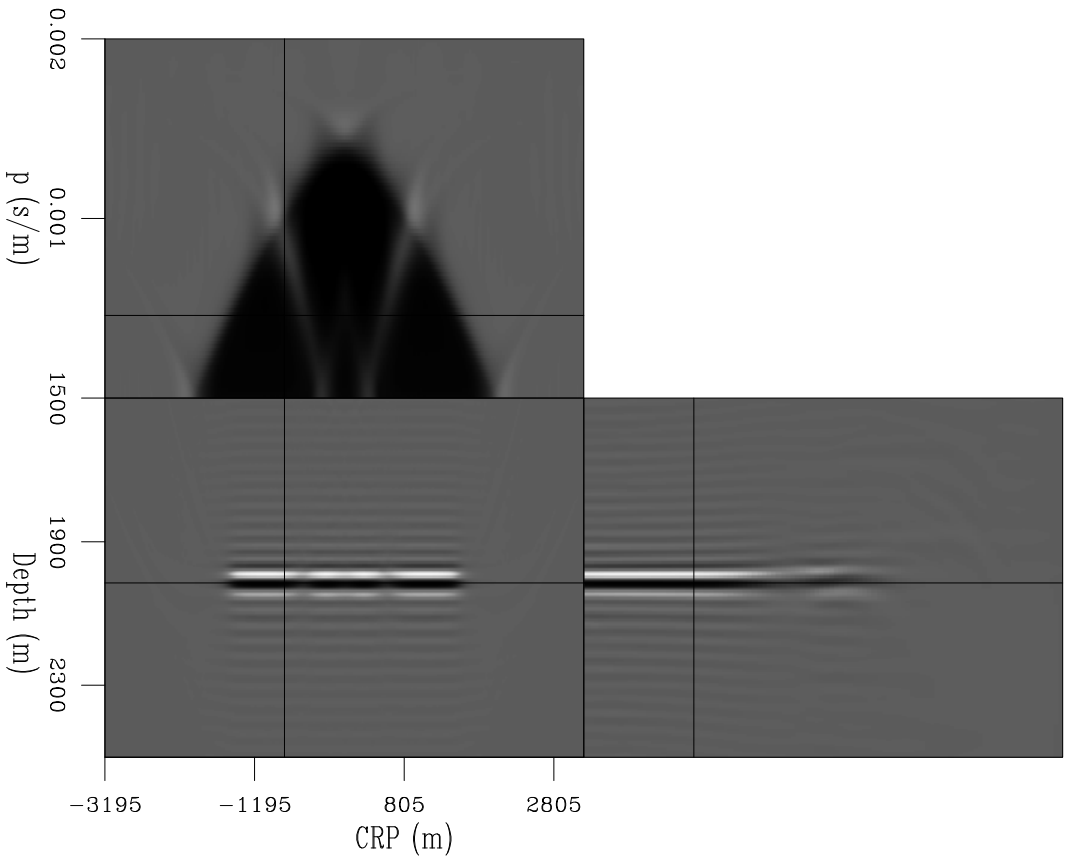

Figure 3.10: Result after 3 iterations of geophysical RIP. The holes in the CIGs seen in Figure 3.9 have been largely filled in. precop-symes.1dprec3it [CR]

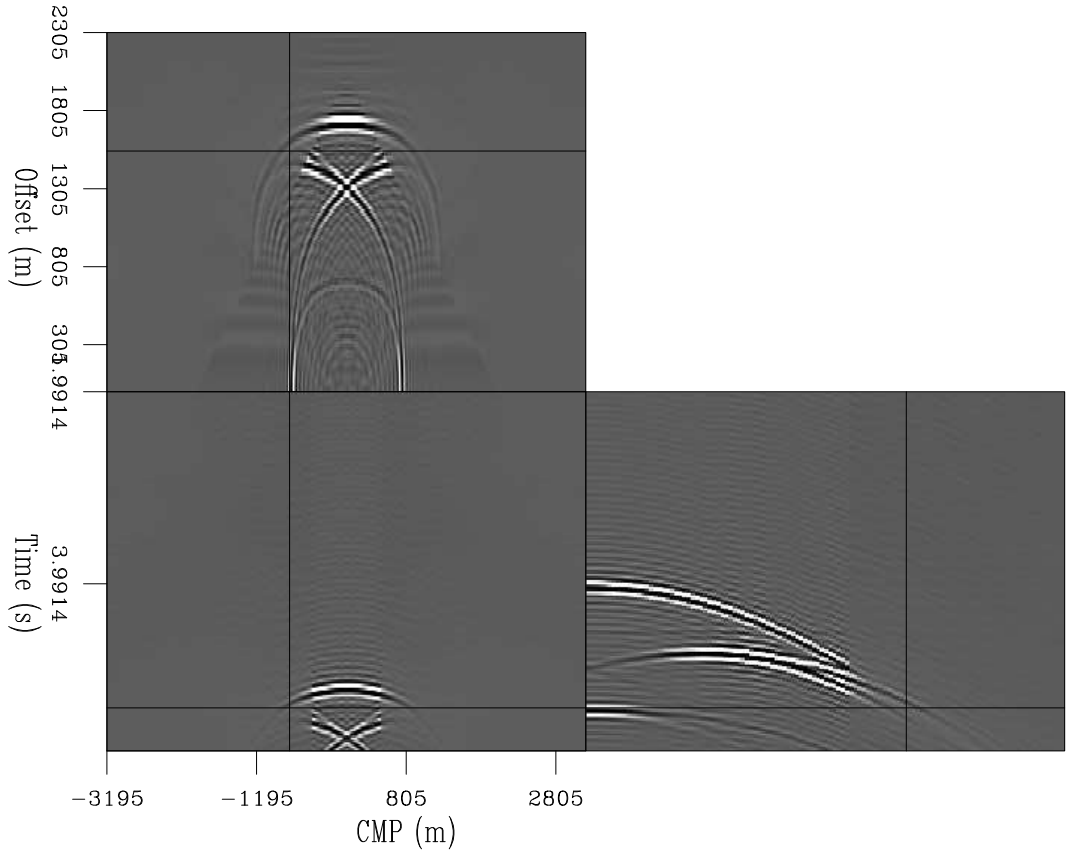

Figure 3.11: The "expanded" data after 3 iterations of geophysical RIP. The regularization of the model space has filled in areas from which the seismic data was directed outside of the survey area. This has "extended" the data beyond the limits seen in Figure 3.8. precop-dat.data_extended.3it1eps [CR]

Expanded fitting goals

The simple fitting goals seen in a previous section (3.9) do not reflect what must be done to use RIP in practice. The seismic imaging results in this thesis are obtained using these fitting goals:

$$\mathbf{0} \approx \mathbf{W_g W_u W_c (LSp - d)} \tag{3.11}$$

$$\mathbf{0} \approx \epsilon \mathbf{Ip}. \tag{3.12}$$

$\mathbf{W_g}$ is a mask that allows us to pad the offsets and frequencies. $\mathbf{W_c}$ is weighting operator that allows us to apply the Jacobian and mask out angles beyond the critical angle. $\mathbf{W_u}$ is a user-defined mask that can be used to further limit the ray parameters, generally to smooth in depth the effect of masking beyond the critical angle. $\mathbf{S}$ now has two possible definitions. It can be the inverse of the geophysical regularization operator $\mathbf{A_f}$ or it can be the inverse of the cascade of the geophysical regularization operator and the geological regularization operator $\mathbf{A_f A_l}$.

In practice, the downward continuation migration operator $\mathbf{L}'$ needs to be modified. First, to reduce artifacts, I have included absorbing boundaries to reduce edge effects. Second, to reduce the computational cost of the inversion, I have designed the migration operator so that it has a variable depth step option so that the inversion can take one step through the whole water column.

Accommodating the model space regularization in the data space

Although $\mathbf{W_c}$ and $\mathbf{W_u}$ are useful for obtaining a clean inversion result, $\mathbf{W_g}$ is vital in the regularized inversion process. The regularization of the model compensates for poor illumination, some of which is caused by energy leaving the extents of the survey. Since the regularization helps to recover this energy, we need to be able to map it into the data space when the forward operation $\mathbf{L}$ is performed within the conjugate-gradient iteration. This means that we need to

pad the offset axis in the data space. However, we don't want to include this energy in the residual space, so we use the weighting operator $\mathbf{W_g}$ to mask it out.

In addition to the "recovered" data along the offset axis, regularization will also introduce frequencies that were not in the recorded data. This occurs because the regularization may be designed in a way that mixes the images corresponding to different aperture angles. When this occurs, it has the effect of equalizing the vertical wavenumber content across the angle axis. The shorter wavelengths are spread from the near-vertical incidence images toward the wide-aperture angle images and the longer wavelengths are spread from far angles to near angles. A sketch of how this occurs can be seen in Figure 3.12. The plane on the left is the model space where the regularization is acting. For the purpose of this explanation, assume that the regularization spreads energy fully between the horizontal lines. When this is mapped to the data space (right plane), those bounding lines curve as shown. The dashed lines show the frequency range of the original data. As with the offset axis, the data space must be padded along the frequency axis to allow the "recovery" of the frequencies as well.

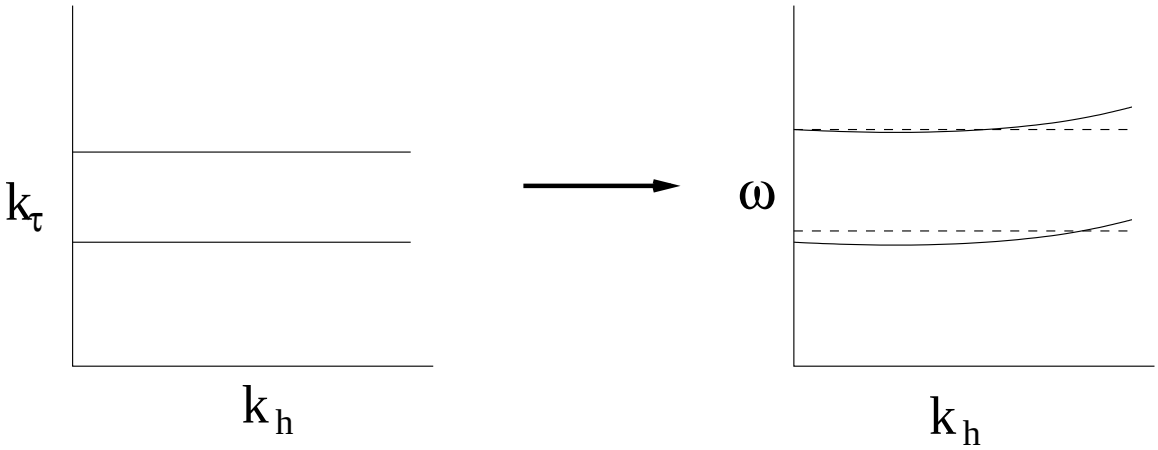

Figure 3.12: Constant velocity example of "lost" frequencies. Left: model space where regularization spreads energy throughout the region bounded by the two horizontal lines. Right: data space where the two bounding lines now curve upward. The dashed lines indicate the frequency range of the original data. precop-freqpad [NR]

RIP VS. MODEL SPACE WEIGHTING

Iterative least-squares inversion is a computationally expensive way to equalize amplitudes in areas of poor illumination. A less expensive method to equalize amplitudes is simple weighting in the model space. Model space weighting operators can be applied to an image after it has been produced by a migration operator. Rickett (2001) suggested using the velocity model and a downward-continuation operator to give us an appropriate weighting operator that will compensate for illumination.

In this section, I will first review the method proposed by Rickett (2001) for the construction of a model space weighting operator. I will then apply this weighting operator to a complex synthetic model with clear illumination problems. Finally, I will compare the model space weighted results with the more expensive preconditioned inversion method I have introduced in this chapter.

Rickett (2001) described a simple *a posteriori* diagonal weighting operator $\mathbf{W}_\mathrm{m}$. To approximate $\mathbf{W}_\mathrm{m}$, we begin by formulating our imaging operation as

$$\mathbf{W}_\mathrm{m}^2 \mathbf{L}'\mathbf{d} \;\approx\; \mathbf{m}. \tag{3.13}$$

The question now is how to get $\mathbf{W}_\mathrm{m}$. Claerbout and Nichols (1994) showed that by applying a forward operator and its adjoint to a reference model, we will get a weighting function with the correct physical units. Rickett (2001) took it a step further to show that for illumination, we can find the approximate weighting function in this manner:

$$\mathbf{W}_\mathrm{m}^2 = \frac{\mathbf{diag}(< \mathbf{m}_\mathrm{ref} >)}{\mathbf{diag}(< \mathbf{L}'\mathbf{L}\,\mathbf{m}_\mathrm{ref} >) + \epsilon^2 \mathbf{I}}. \tag{3.14}$$

Here $\mathbf{m}_\mathrm{ref}$ is the chosen reference model, ϵ is a damping parameter related to the signal-to-noise ratio, and the $<>$ indicate that we take the smoothed analytic signal envelopes. ϵ ensures that we will not be dividing by zero.

In order to examine this weighting operator, I chose to work with the subset of the Sigsbee2A dataset I have shown before. This dataset has a salt body with strong shadow zones

beneath its edges. The velocity model can be seen in Figure 3.2.

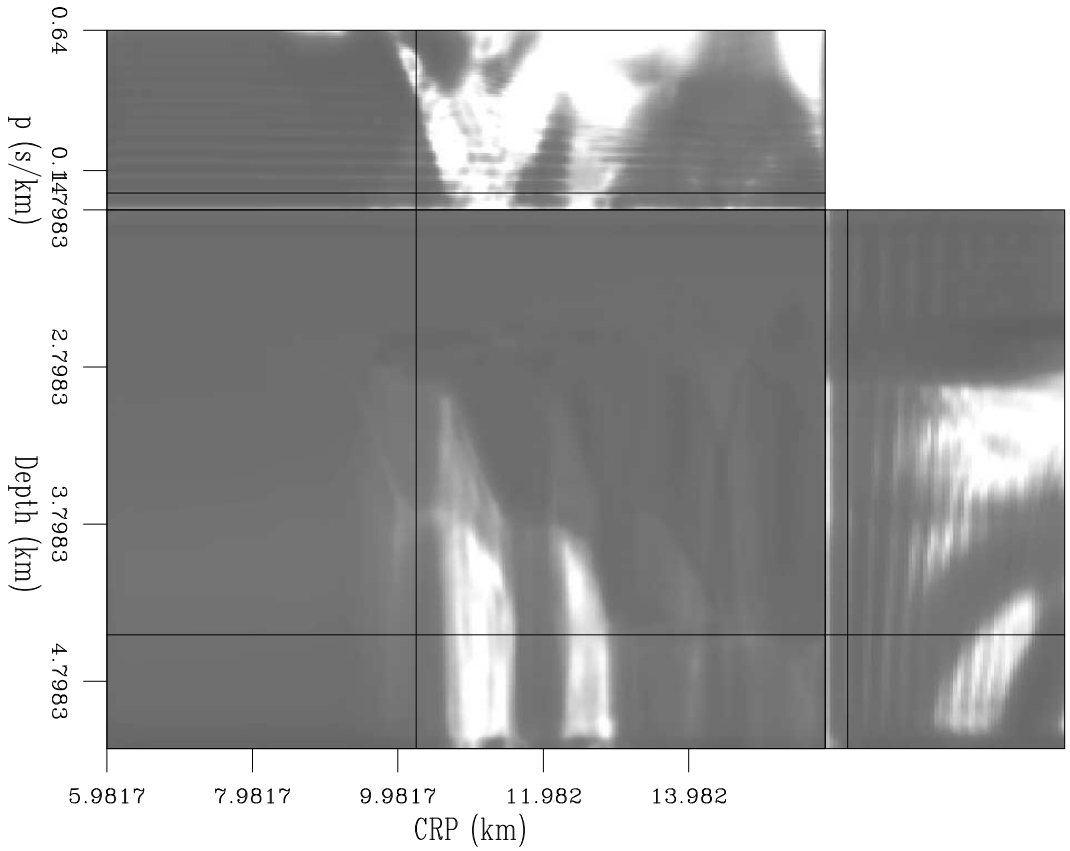

Figure 3.13: The weighting operator ($\mathbf{W}_m^2$) produced using flat layers as the reference model. precop-illumin [CR]

I chose to use flat layers as the reference model, as suggested by Rickett (2001). I modeled the data that would be produced from these flat layers with the adjoint of the migration scheme described in the previous subsection, using the velocity model from Figure 3.2. I then migrated that data to get the weighting operator defined in equation (3.14). Figure 3.13 shows this weighting operator.

The weighting operator in Figure 3.13 is displayed as a flattened cube. The front of the cube shows a common ray parameter slice in which the high values of the weighting operator can be seen in the shadow zones. The top of the cube is shown above the common ray parameter slice and shows a depth slice. In this depth slice, we can see that the weighting

operator indicates that the subsalt illumination along CRPs is becoming worse with larger ray parameters. The side of the cube shows a ray parameter gather taken from a CRP at the salt edge. This view shows how illumination varies along ray parameter and with depth. It also shows some vertical striping that I believe is caused by the way I took the smoothed analytic signal envelope. We must keep this in mind as we apply this weighting function to the image.

Figure 3.14 shows an enlarged view of the stacks in the area at the salt edge for the downward-continuation migration (left panel), the model space weighted result (center), and the preconditioned inversion result (right panel). In the migration result, the noise in the shadow zones is not very strong, but the upswinging artifacts (particularly below a depth of 4.25 kilometers) can easily cause misinterpretation. The model space weighted result has extended the reflectors farther under the salt than the migration result, but it also has increased noise under the salt and strengthened the upswinging artifacts. The inversion result has done a better job of extending the reflectors beneath the salt and has fewer artifacts than either of the other results. The inversion result has eliminated the upswinging artifacts seen in both the migration and the model space weighted result. However, the inversion result has a computational cost approximately seven times [1] greater than the weighted result.

To summarize, although the model space weighting operator does help improve the amplitudes in poorly illuminated areas of seismic images, it does not do as good a job as the least-squares inversion. This is largely due to the fact that the weighting operator increases the amplitude of the noise as well as that of the signal. Regularized least-squares inversion does a better job compensating for poor illumination in areas with low signal-to-noise ratios and helps to reduce artifacts.

REGULARIZATION CONSIDERATIONS

There are several issues that must be considered when using the proposed regularized inversion with model preconditioning. First, the geological regularization scheme that can be used for

[1]Note that the cost of generating the model space weighting operator is equal to two migrations and is applied to a migrated image, making the total cost equal to three migrations. The regularized inversion has a cost of two migrations for each iteration, making the total cost equal to twenty migrations.

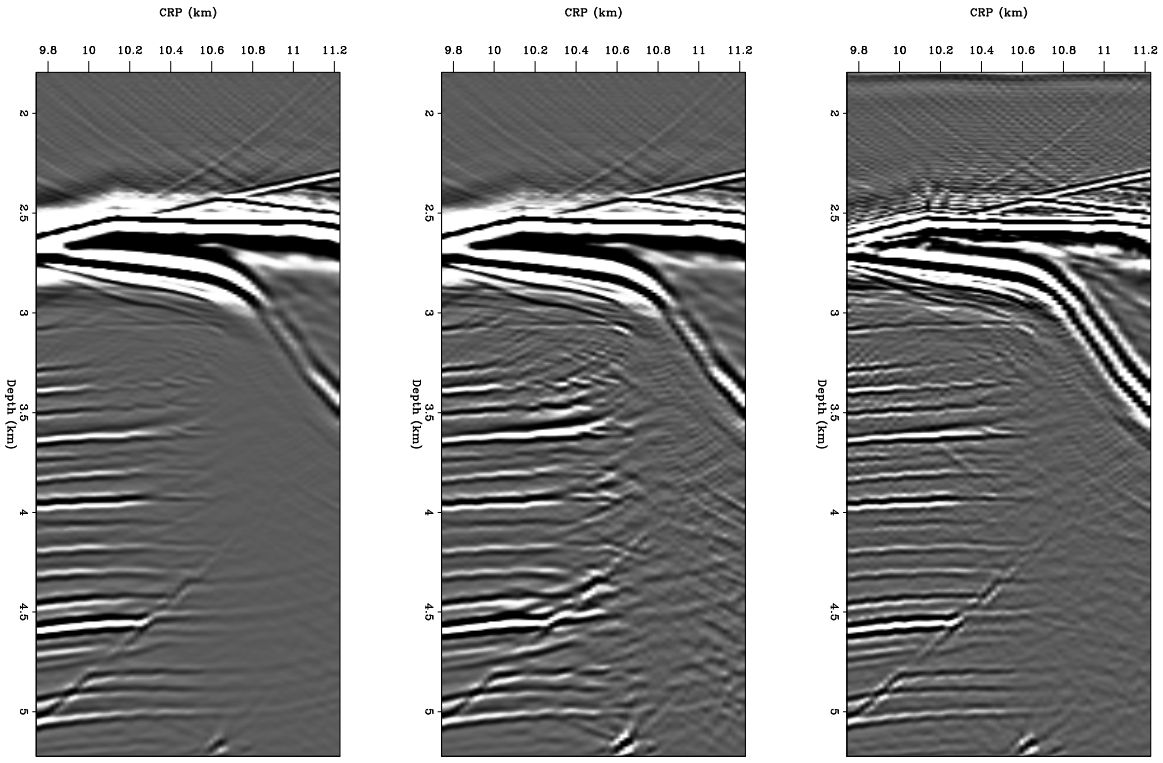

Figure 3.14: Results enlarged from CRP = 9.75km to CRP = 11.25km. Left: stack of migration. Center: stack of model space weighted result. Right: stack of result after 10 iterations of geophysical RIP. precop-zoom [CR]

RIP depends on the user's interpretation or geological model, so what if the regularization operator is wrong? I will show the result of applying the "wrong" regularization operator during RIP. On a related note, the geophysical regularization scheme assumes that the correct velocity model has been used, so there is no moveout along the $\mathbf{p_h}$ axis. I will experiment with several incorrect velocity models and show the results. Finally, since my RIP method does regularize the amplitudes of model along the $\mathbf{p_h}$ axis, we need to know how it will affect any real AVA that might exist in the CIGs.

Regularization operator accuracy

It is clear that the geological inversion is strongly dependent on the regularization operator. Since this operator may be constructed from picked reflectors, it is important to know what happens if the reflector is not picked well. To examine this, I created a regularization operator from the "reflectors" picked in Figure 3.15. In this figure, note that the picked reflectors cross the correct dips at the depths between 3 and 3.4 kilometers and 3.7 and 4.1 kilometers. They cross themselves at depth 4.5 kilometers. The picked reflector beginning at depth 3.75 km follows the correct dip for the most part, but ignores the slight change in dip at the fault at CMP position 7.2 km. The water bottom has been correctly picked. The picked reflector beginning at depth 4.2 km follows the correct dip, but continues well into the shadow zone where it may or may not be correct. Also within the shadow zone is a completely absurd picked reflector put there to see if any event can be created there. Finally, note that the top and bottom of the salt have not been picked at all. This will leave the preconditioning operator in the salt area to be interpolated from the picked reflectors. In this section, I will refer to the dips and reflectors from the migration result as "real" or "correct" and the dips and reflectors used for the inversion as "picked."

The result of using this regularization operator for geological RIP is seen in Figure 3.16. As expected, the result isn't good. In the areas where the picked dips were considerably wrong, such as at the left side between 3 and 3.4 kilometers and 3.7 and 4.1 kilometers, there are almost no events at all in the result. This is also true for the "M" shaped picked reflector in the shadow zone area. In these areas, the data fitting goal from equation (3.9) has rejected

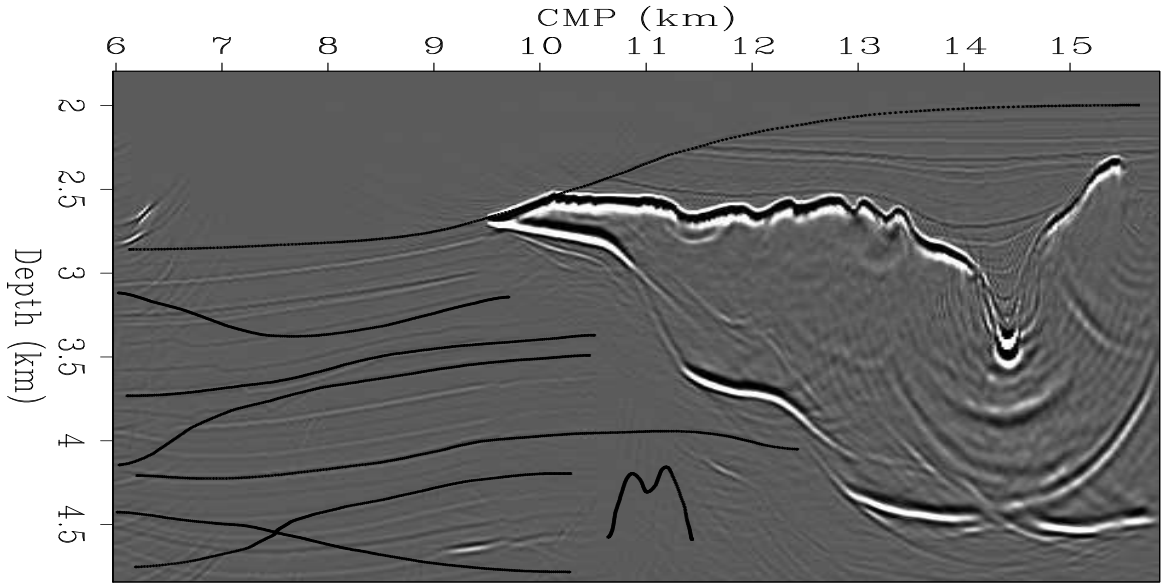

Figure 3.15: Migration result with the picked "reflectors" overlaid. These reflectors do not match the correct reflectors and should produce a bad result. precop-reftest [CR]

the attempted regularization, essentially canceling out all of the image. However, elsewhere in the shadow zone, where the picked dips are reasonable, there is good continuation of the real events underneath the salt. In the area where the picked reflectors cross, there is a similar canceling of energy, but it is reassuring to see that the inversion has handled the crossing dips without becoming unstable. Finally, it is clear that not picking the salt boundaries has caused major problems. Since no picked dips were provided in the area of the salt, the steering filter interpolated the dip of the water bottom down through this region. The result shows strong events where the dip of the water bottom is similar to that of the salt boundaries, but very low energy elsewhere, once again due to the rejection of the regularization by the data fitting goal.

This experiment showed that the inversion will reject dips that are incorrectly picked where data exists. The data fitting goal (3.9) assures that picked dips that generate an event which interferes with the data are rejected. Picked dips that generate an event that doesn't interfere with existing data are allowed. Picked dips that cross, or meet at a point can be accommodated by the inversion. It is necessary to pick reflectors wherever the dominant dip changes.

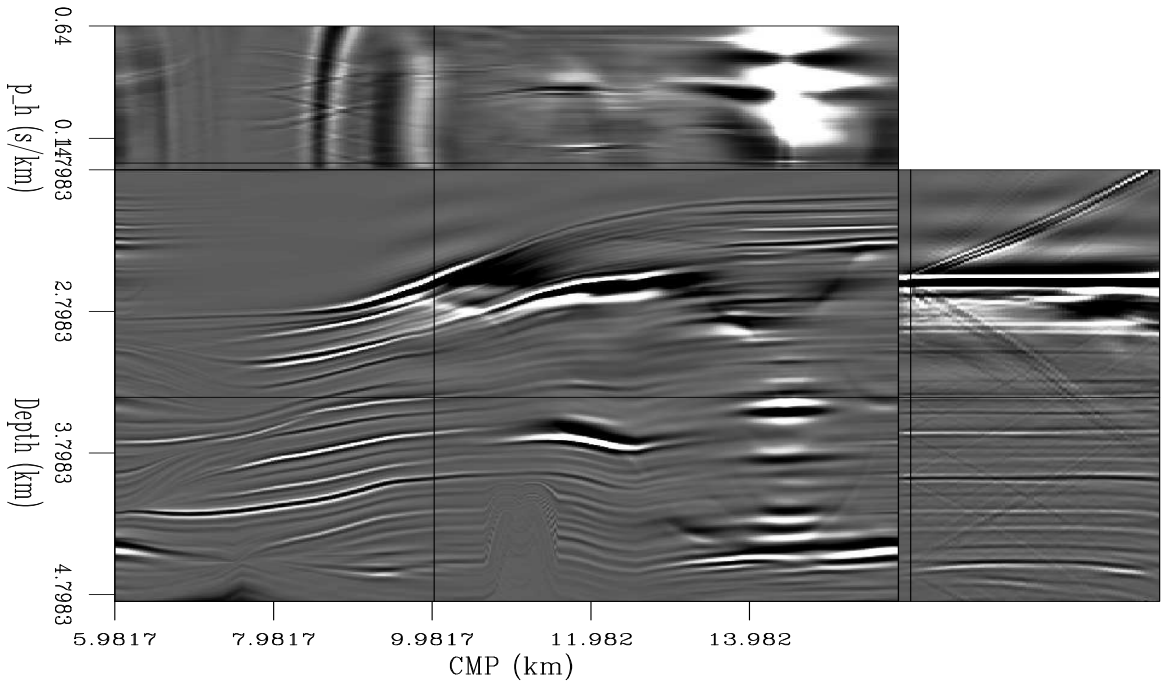

Figure 3.16: Result of 3 iterations of the geologically regularized result with badly picked reflectors. precop-2dfilttest [CR]

Velocity sensitivity

The difficulties of imaging below salt edges are compounded by the difficulty of generating an accurate velocity model in these areas. The majority of imaging techniques require an accurate velocity model in order to produce a well focused result. The geophysical regularization scheme in particular expects the events to be flat along the offset ray parameter axis - that is, that the correct velocity be used.

I applied the geophysical RIP scheme to the Sigsbee2A dataset, using different velocity models. The correct velocity model can be seen in Figure 3.2. The result of migration using the correct velocities is Figure 3.1. The result of 3 iterations of geophysical RIP using the correct velocities is in Figure 3.17.

To test the sensitivity of the geophysical RIP, the first incorrect velocity model I tested simply scaled up the correct velocities by 5%. As expected, the migration result using this

velocity model (Figure 3.18) shows the events positioned deeper than they should be and moveout along the offset ray parameter axis.

Recall that the geophysical regularization operator acts horizontally along the offset ray parameter axis. It is this sensitivity that we are interested in observing in the result of 3 iterations of geophysical RIP using the high velocity model (Figure 3.19). Note that once again the geophysical RIP has cleaned up many of the artifacts. In the CRP-depth panel, the events extend farther under the salt, in a similar way to the inversion result using the correct velocity (Figure 3.17). The more interesting result is the CIG panel. The inversion is still successfully filling in the holes along the events at the mid-range of offset ray parameters. At large p_h, where the moveout is more pronounced, the regularization has made some attempt to change the dips to be more horizontal, but the moveout is still visible. This means that this result is most likely not safe to use for velocity analysis, but this inversion technique was never intended as a velocity tool. Overall, this result indicates that this technique can produce a better image than migration alone, even when the velocity model is incorrect by up to 5%.

A more extreme velocity model I tested was a severely smoothed one (Figure 3.20). This model has been smoothed so much that the canyon in the top of the salt has disappeared. As expected, the migration result from this model isn't very good (Figure 3.21). The depth positioning of events is fairly good away from the salt, but becomes poor near the salt. The salt top and bottom are very poorly imaged. The events in the CIG panel appear to be mostly random.

The result of 3 iterations of geophysical RIP using this smoothed velocity model can be seen in Figure 3.22. Although many of the artifacts have been cleaned up, overall the image is not any better than the migration result. The events in the CIG panel are more horizontal, but they are not more believable than the events in the CIG of the migration result. This is a reassuring result, as it indicates that the regularization was not able to artificially introduce events where the data indicated otherwise.

The results of geophysical RIP with incorrect velocity models are encouraging. As long as the velocity model is not too inaccurate, the regularization operator behaves as it would for the correct velocity model and produces a better image than migration alone. In the case of a

highly inaccurate model, the inversion itself prevents us from producing an image that would conflict with the known data. Overall, as long as the velocity model is reasonably close to correct, the assumption of zero moveout made by the geophysical regularization operator is acceptable.

Amplitude considerations

Geophysical RIP acts along the $\mathbf{p_h}$ (or angle) axis, therefore it may affect any amplitude variation with angle (AVA) that should exist due to rock properties rather than illumination problems. Although it is technically possible to extract information about rock properties from the actual magnitude of the amplitudes for a given event, generally AVA analysis is more concerned with the trend of the amplitude variation along the event. In this section, I will use a simple synthetic model to examine the effect of geophysical RIP on AVA trends.

The synthetic model used here is a simple 4 flat layer model, with different velocity contrasts at each of the three interfaces 3.23. The velocity for the top layer is 1.5 km/s, the second layer is 1.75 km/s, the third layer is 2.5 km/s and the deepest layer is 3.75 km/s. I created the synthetic data for this model with finite difference modeling.

For this simple model, it is clear that we have no illumination problems. There is no need to use RIP at all. Applying geophysical RIP can only affect the AVA, without improving the image at all. Therefore, this model is a "worst case scenario" for the geophysical RIP scheme.

Effects of migration operator

I first investigated the effects of my downward-continuation migration operator on the AVA. I migrated the synthetic data using the correct velocity model and extracted my calculated amplitudes along each of the three interfaces. These results can be seen in Figure 3.24. In each of the panels, the solid line represents the theoretical AVA values (calculated following the example of de Bruin et al. (1990)) and the dots show the AVA values obtained after migration. The horizontal axis is shown in offset ray parameter (p_h). Based on the relationship in equation (2.13), the range of opening angles for the shallowest interface (left panel of Figure 3.24) is $0^o - 44^o$, the range for the second interface (center panel of Figure 3.24) is

$0^o - 46^o$, and the range for the deepest interface (right panel of Figure 3.24) is $0^o - 68^o$. Overall, the results for each of the three interfaces are good. The calculated values for the second and third interfaces are not as consistent as the shallowest interface, partly due to the presence of more migration artifacts at depth. In the case of the deepest interface, it is also an effect of the survey geometry: we cannot expect the deep event to have reliable amplitude information at large p_h (larger than an opening angle of 36^o) because the common midpoint and offset ranges of the seismic data are limited, so energy reflecting at large angles from the deep event are lost. Additionally, I have neglected the $\frac{2cos(\theta)}{V(m,z)}$ weighting factor explained by Wapenaar et al. (1999) and Sava et al. (2001), so the amplitudes after migration should have a stronger upward trend than theoretically expected. However, the overall trends of all of the calculated AVA values are fairly accurate.

Effects of RIP

Having obtained satisfactory AVA results with my downward-continuation migration operator, I moved on to test my geophysically Regularized Inversion with model Preconditioning (RIP). For this test, I set ϵ to zero. Although this essentially sets the model styling goal of fitting goals (3.8) to zero, I am preconditioning the problem so I am still regularizing the inversion through the $\mathbf{A^{-1}}$ in the data fitting goal. Using this formulation, I ran tests using 5, 10 and 15 iterations. The results after 5 iterations can be seen in Figure 3.25. The results after 10 iterations are shown in Figure 3.26 and the results after 15 iterations are shown in Figure 3.27.

For all three exercises, we notice that the shallowest interface (left panels) has developed an artificial increasing trend. This is partly due to an edge effect at the small p_h, and partially due to the effects of the regularization. It is more pronounced for this interface because the true AVA trend is expected to be almost flat. The edge effect at small p_h is present for the other two interfaces as well.

Looking at the results for the second interface (center panels of Figures 3.25 through 3.27), it appears that our results after regularized inversion are more accurate than the result we saw from the migration (center panel of Figure 3.24). For the second interface, other than the edge effect at small p_h, the AVA trend is quite accurate after 5, 10 and 15 iterations. The best result for the second interface appears to be that after 10 iterations. The result after 15 iterations is

deteriorating slightly as the inversion is trying harder to accommodate artifacts that exist in the data.

The results for the deepest interface (right panels of Figures 3.25 through 3.27) are also better than the result from the migration (right panel of Figure 3.24). They have the same problems at large p_h due to survey geometry, and have the edge effect at small p_h seen for the other interfaces, but the AVA trend between these two extremes is close to the expected trend. Due to the known problem at large p_h, I have actually chosen to turn the regularization operator off halfway along the p_h axis to keep the inversion from spending all of its effort trying to correct the sudden decrease in amplitude. Once again, it seems that the AVA trend in the result after 10 iterations is the best.

The geophysical RIP scheme does affect the amplitudes along the p_h axis, but it can be designed in a way that does not destroy the AVA information. If AVA analysis is desired, the strength of regularization and the number of iterations becomes even more important than if we are just concerned with imaging. Since geophysical RIP is most useful where illumination problems exist, the choice of regularization strength and the number of iterations becomes a balancing act between compensating for the poor illumination which interferes with AVA analysis and preserving the AVA trends.

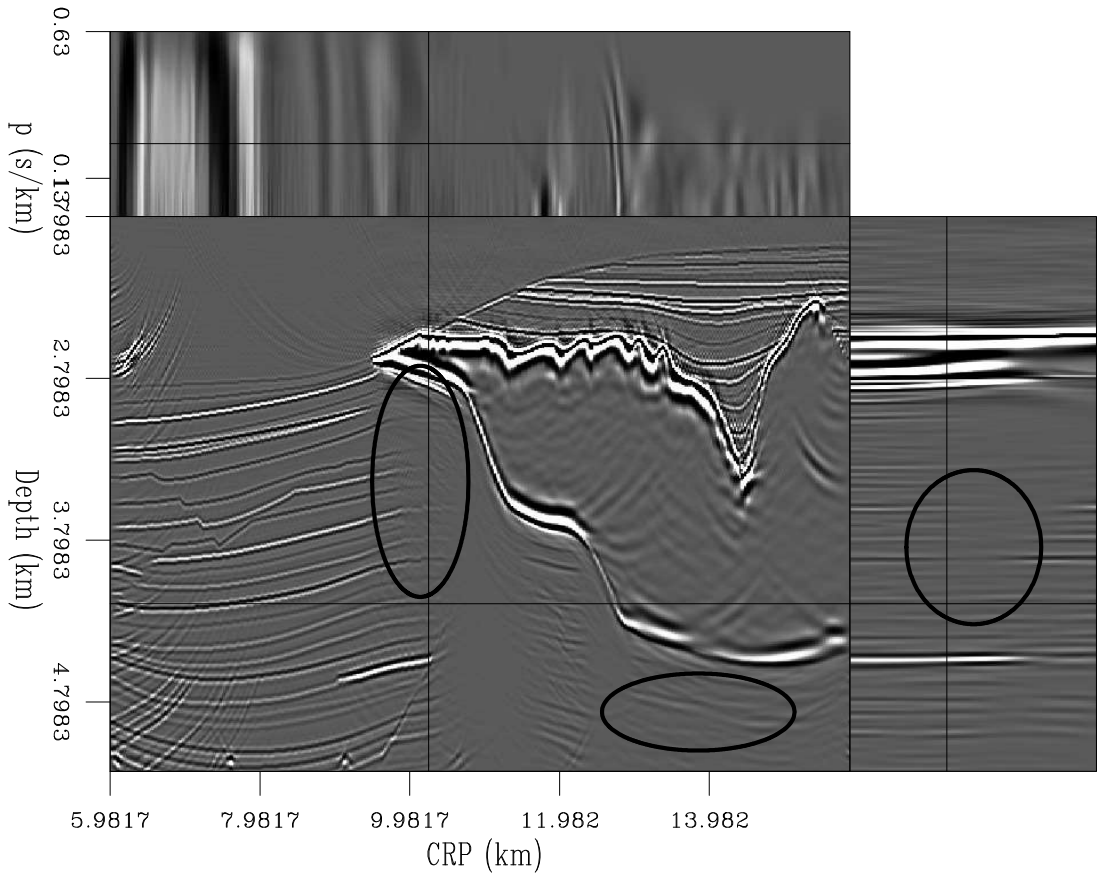

Figure 3.17: The result of 3 iterations of geophysical RIP inversion using the correct velocity model. Note the more consistent amplitudes of events as they pass beneath the salt in the CRP-depth panel and the lack of artifacts obscuring events beneath the salt (inside ovals). In the offset ray parameter-depth panel note the filling in of the holes in the events at the mid-range of offset ray parameters (inside ovals). precop-geop.corvel [CR]

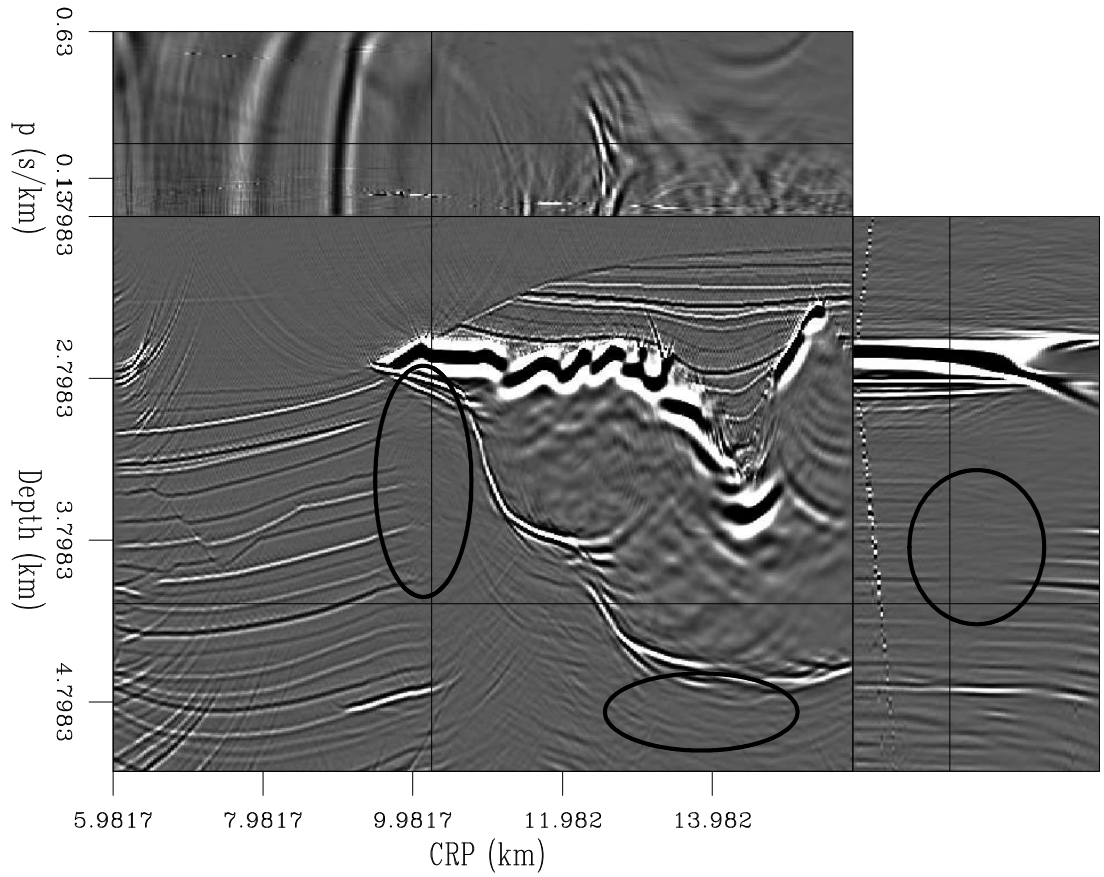

Figure 3.18: The result of downward-continuation migration using a velocity model 5% higher than the correct model. The events are all positioned deeper than they should be and there is moveout along the offset ray parameter axis. The ovals still indicate the loss of amplitudes under the salt edge and the poor imaging beneath the salt in the CRP-depth panel and holes in the events in the p_h panel. precop-mig.hivel [CR]

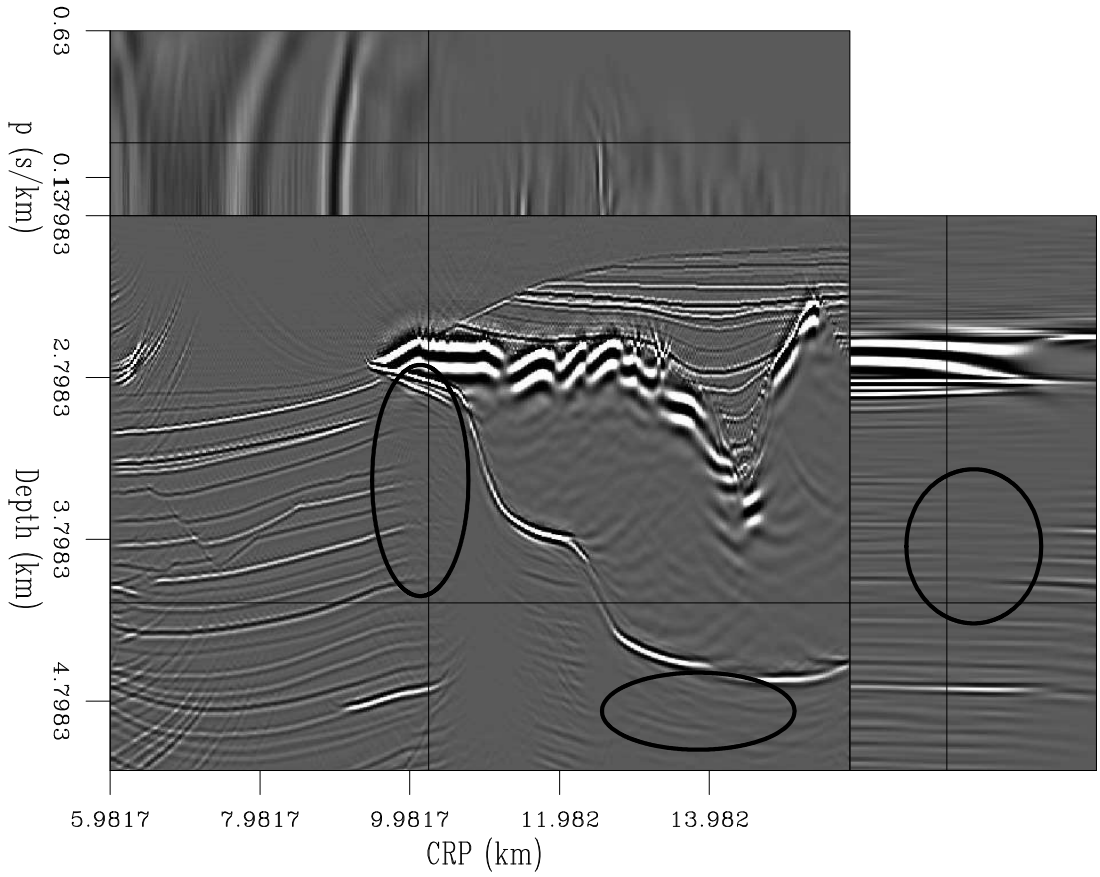

Figure 3.19: The result of 3 iterations of regularized inversion using the 5% scaled up velocity model. Despite the use of the incorrect velocity model, the image is quite comparable to the result using the correct velocity (Figure 3.17). In the CRP-depth panel, the events extend farther under the salt and events under the salt can be seen (inside the ovals). In the p_h-depth panel, the holes in the events are filled in (inside the oval). precop-geop.hivel [CR]

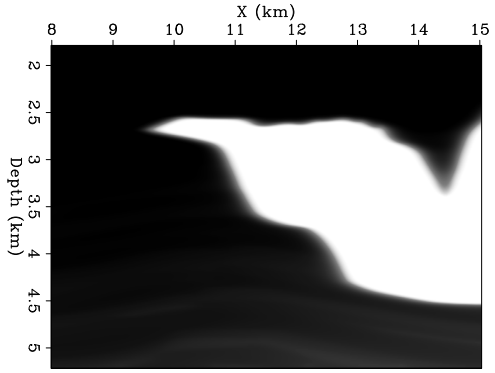

Figure 3.20: The smoothed velocity model. Note that the canyon in the top of the salt has disappeared. precop-vel.smoothvel [ER]

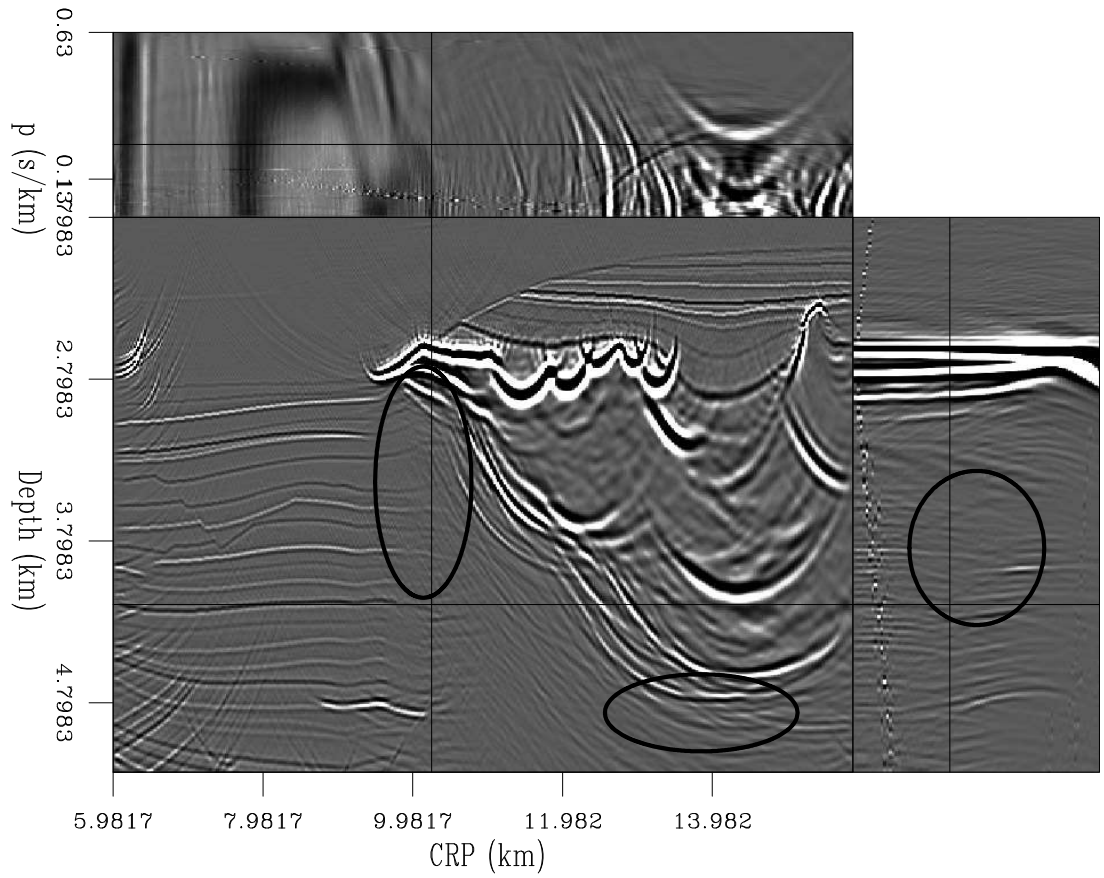

Figure 3.21: The result of downward-continuation migration using a severely smoothed velocity model. The events in the CRP-depth panel are properly imaged away from the salt but are mispositioned near the salt. The offset ray parameter-depth panel is completely uninformative. The ovals indicate the same absolute regions as the ovals in 3.17. precop-mig.smoothvel [CR]

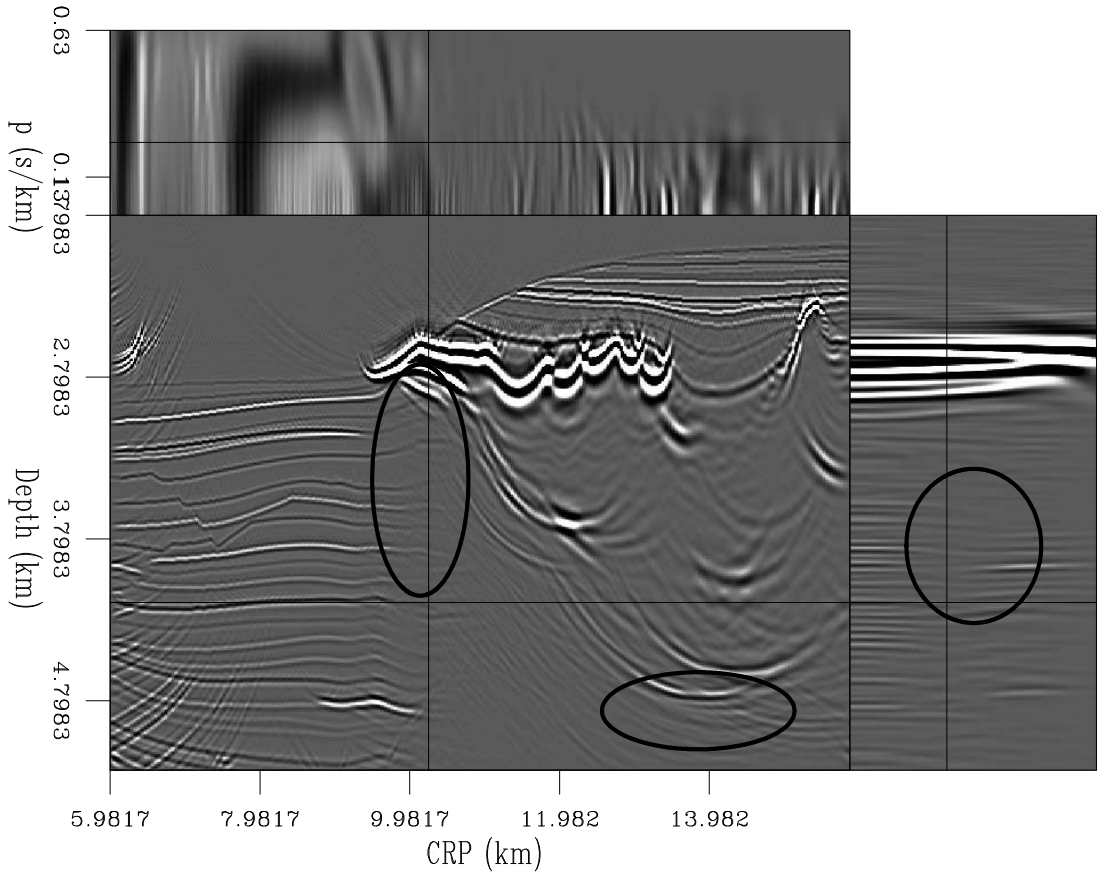

Figure 3.22: The result of 3 iterations of preconditioned inversion using the smoothed velocity model. The result is cleaner than the migration result, but not more believable. The ovals indicate the same absolute regions as the ovals in 3.17. precop-geop.smoothvel [CR]

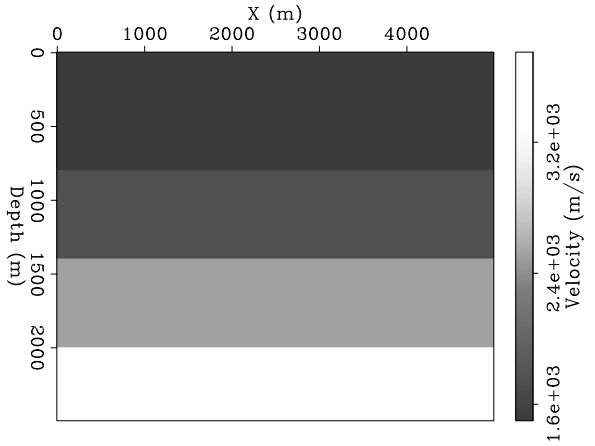

Figure 3.23: Velocity model to test the effect of geophysical RIP on AVA. precop-ampvel [ER]

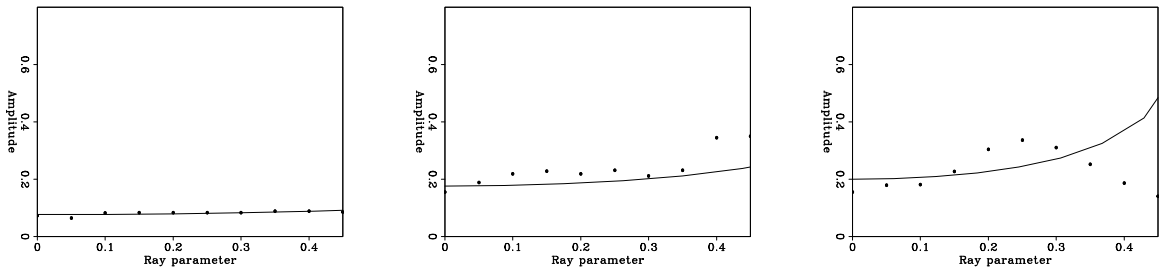

Figure 3.24: Amplitude variation with p_h. Left panel shows the results for the shallowest interface as seen in Figure 3.23, center panel for the second interface, and right panel for the deepest interface. The solid line shows the theoretical value and the dots show the values obtained from the image after downward-continuation migration. precop-ava.comp.mig [CR]

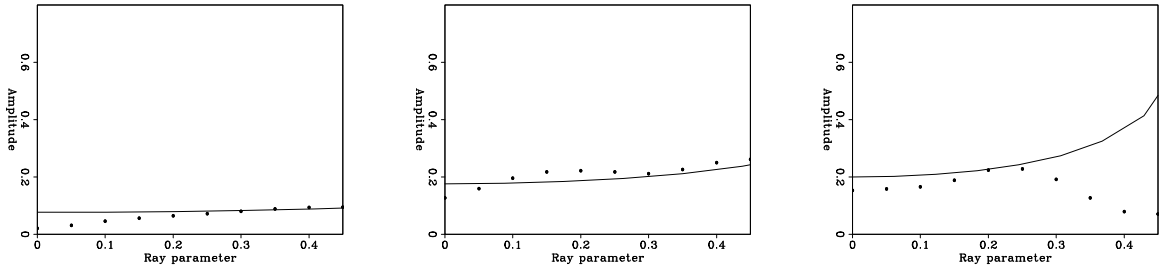

Figure 3.25: Amplitude variation with p_h for geophysical regularization after 5 iterations. Left panel shows the results for the shallowest interface as seen in Figure 3.23, center panel for the second interface, and right panel for the deepest interface. The solid line shows the theoretical value and the dots show the values obtained after inversion. precop-ava.comp.5it0eps [CR]

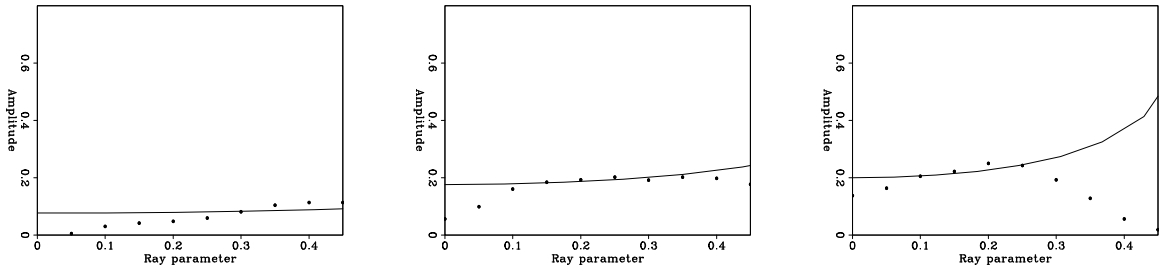

Figure 3.26: Amplitude variation with p_h for geophysical regularization after 10 iterations. Left panel shows the results for the shallowest interface as seen in Figure 3.23, center panel for the second interface, and right panel for the deepest interface. The solid line shows the theoretical value and the dots show the values obtained after inversion. precop-ava.comp.10it0eps [CR]

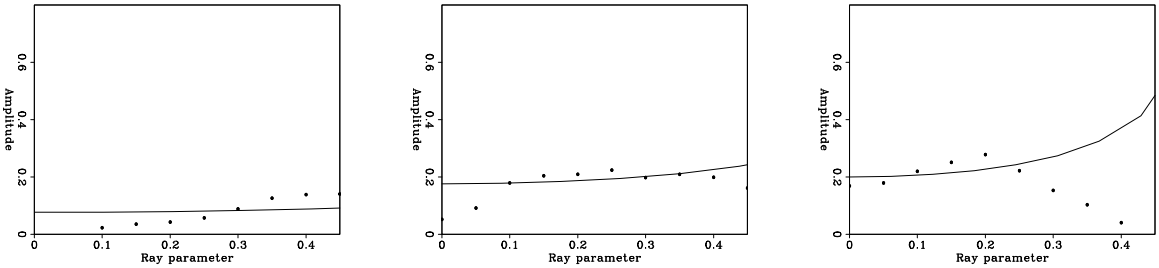

Figure 3.27: Amplitude variation with p_h for geophysical regularization after 15 iterations. Left panel shows the results for the shallowest interface as seen in Figure 3.23, center panel for the second interface, and right panel for the deepest interface. The solid line shows the theoretical value and the dots show the values obtained after inversion. precop-ava.comp.15it0eps [CR]

Chapter 4

Real data results

The true advantages of regularized inversion with model preconditioning (RIP) can be seen when applying it to real data. In this chapter, I apply both geophysical and geological RIP to real 2-D data. I also apply geophysical RIP to real 3-D data. The migration and RIP results shown in this chapter do not have axis information for the depth axis at the request of the sponsors who provided the data.

THE DATASET

The dataset upon which I have chosen to demonstrate RIP is a subset of the real 3-D Gulf of Mexico dataset provided to SEP by BP and ExxonMobil. The portion of the 3-D velocity model for the subset I am using can be seen in Figure 4.1. This subset contains 600 inline positions and 72 crossline positions. The salt body on the right side causes significant shadow zones that may mask potential hydrocarbon reservoirs. There are known 3-D faults in the sediments away from the salt and it is likely that more faults exist beneath salt in the shadow zones. The velocity model is believed to be accurate, which is important given the nature of my geophysical regularization operator (Clapp, 2003).

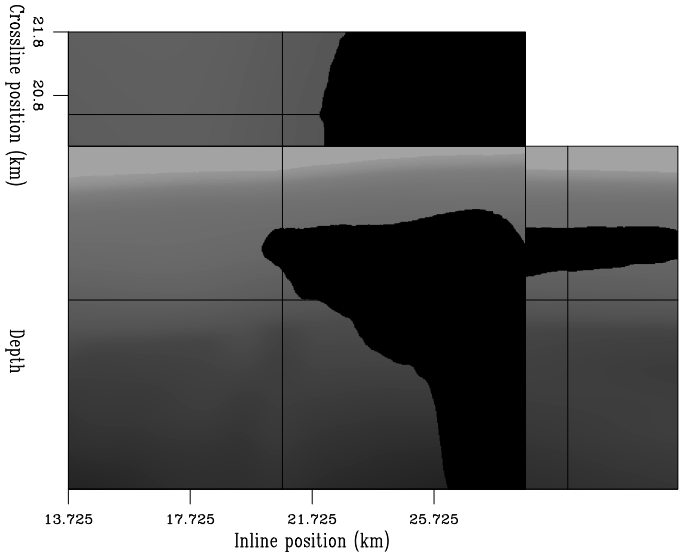

Figure 4.1: Subset of the BP Gulf of Mexico velocity model. real-bpvel [CR]

2-D RESULTS

To test RIP on a real 2-D example, I extracted a single line from the subset of the deep water BP Gulf of Mexico dataset. This line is located at the crossline position of 20 km, chosen in an attempt to minimize the 3-D effects of the salt structure. However, this line will still be affected by the 3-D faults known to run through this volume.

Geophysical RIP

As described in the previous chapter, the regularization operator used for geophysical RIP acts along the offset ray parameter axis. To set the strength of regularization (see the fitting goals (3.9)) for this real data example, I chose $\epsilon = .001$ by trial and error. I performed 6 iterations which was chosen based on data space residuals, as will be explained later. The result can be seen in Figures 4.2 through 4.5. In each of these, the migration result is displayed above the geophysical RIP result. Both show a common ray parameter section on the left and a common image gather (CIG) on the right. The vertical lines indicate which CRP location and offset ray parameter value the panels are taken from. The effect of the regularization is clearest in the CIGs. The common ray parameter sections also show the effects. All of these results show

a crisper image after RIP, with fewer artifacts. To see the improvements more clearly, I have zoomed in on the area beneath the salt in Figures 4.6 through 4.9.

In Figures 4.6 through 4.9, the same ovals are shown on the migration result (top) and the geophysical RIP result (bottom). Figures 4.6 and 4.7 have particularly clear examples of the holes in the common image gather being filled. The whole common ray parameter section is cleaner than the one from the migration result. The subsalt reflectors are extending into the shadow zones everywhere, particularly in the areas indicated by the ovals. Geophysical RIP produces a cleaner result with better illumination than migration.

It is also interesting to stack (sum along the offset ray parameter axis) the results (Figure 4.10). Once again, the stack of the migration result is shown on top and the stack of the result after 6 iterations of geophysical RIP is on the bottom. The ovals indicate where the reflectors extend farther into the shadow zones. In the RIP result, some reflectors can be seen almost all the way through the poorly illuminated areas. Also, the artifacts seen in the stack of the migration result are reduced in the RIP result.

As mentioned earlier, I chose to display the RIP results after 6 iterations based on an examination of the data space residuals as the least-squares inversion was performed. The data space residuals for each iteration can be seen in Figure 4.11. Each row is a collection of CMP gathers taken from locations across the whole survey. I have taken the envelope of the energy and clipped the high values, which appear as solid black regions. The first row is the original data, the second row shows the same CMP gathers after 2 iterations, the third row is after 4 iterations, fourth row after 6 iterations, fifth row after 8 iterations and sixth after 10 iterations. The salt body begins at a CMP location between the fifth and sixth gathers shown.

The biggest change in the residual energy occurs within the first two iterations, as would be expected. We see that the residual energy away from the salt decreases quickly (the black areas decrease). The residual energy associated with the salt also decreases, with the exception of energy beginning around 3.75 seconds that is caused by converted waves that my acoustic code cannot properly handle. The small change in residual energy between the sixth and tenth iterations indicates that the inversion is nearing convergence. Therefore, we expect very little change in the image after 6 iterations.

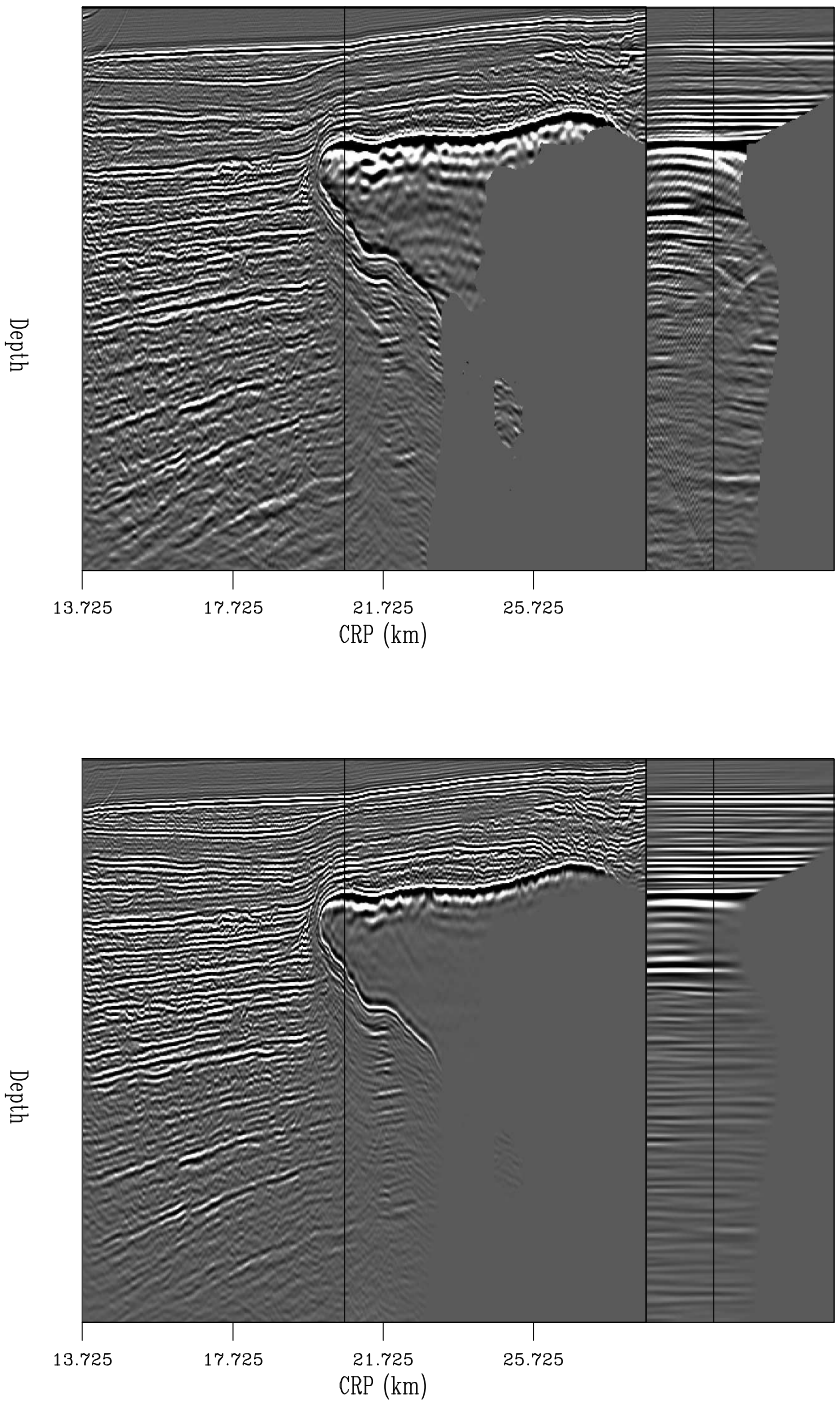

Figure 4.2: Top: result of downward-continuation migration of 2-D line. Left part is a common offset ray parameter section at $p_h = .265$, right part is a common image gather from $CRP = 20.675$. Bottom: result of 6 iterations of geophysical RIP. real-bp2d.1 [CR,M]

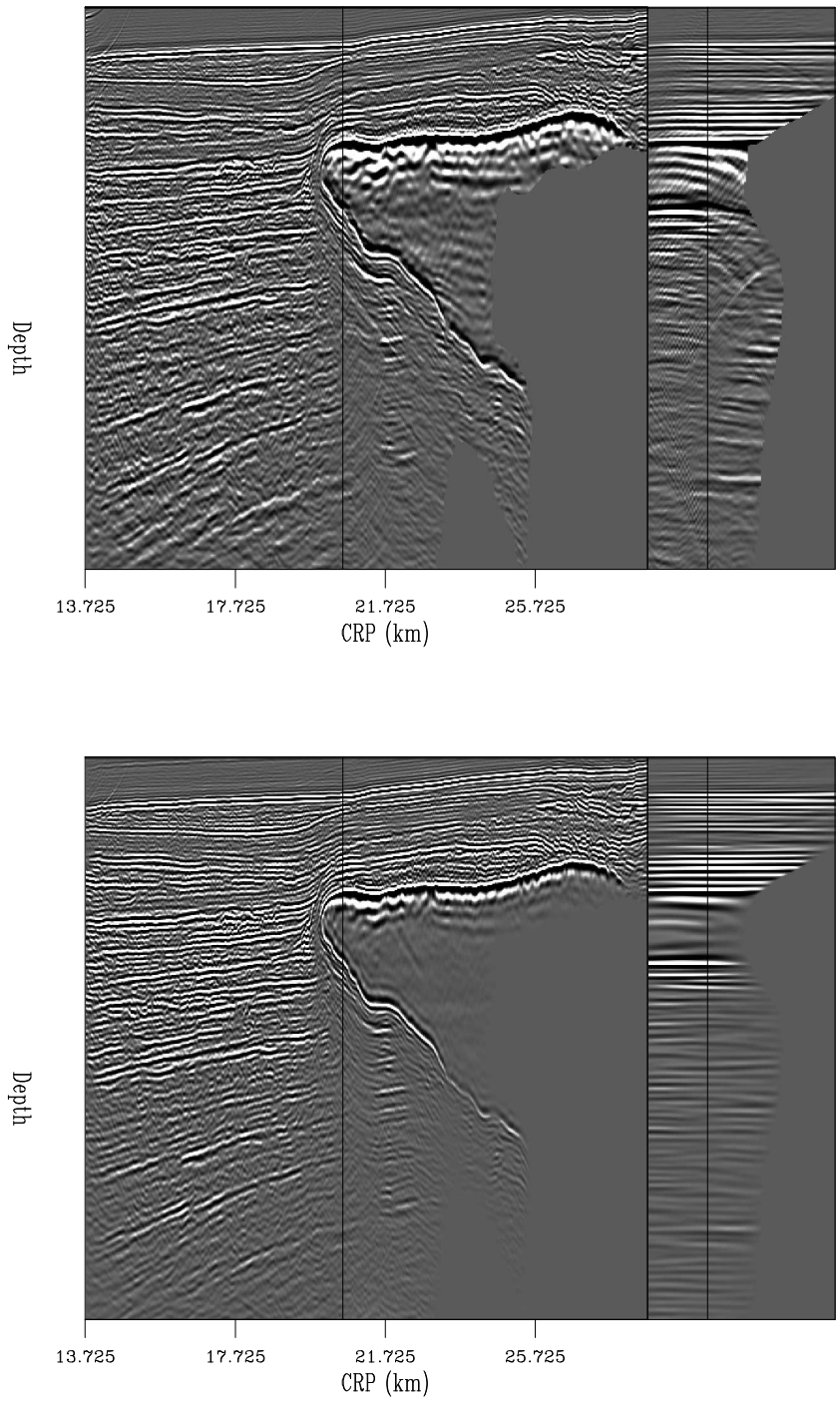

Figure 4.3: Top: result of downward-continuation migration of 2-D line. Left part is a common offset ray parameter section at $p_h = .235$, right part is a common image gather from $CRP = 20.575$. Bottom: result of 6 iterations of geophysical RIP. real-bp2d.4 [CR,M]

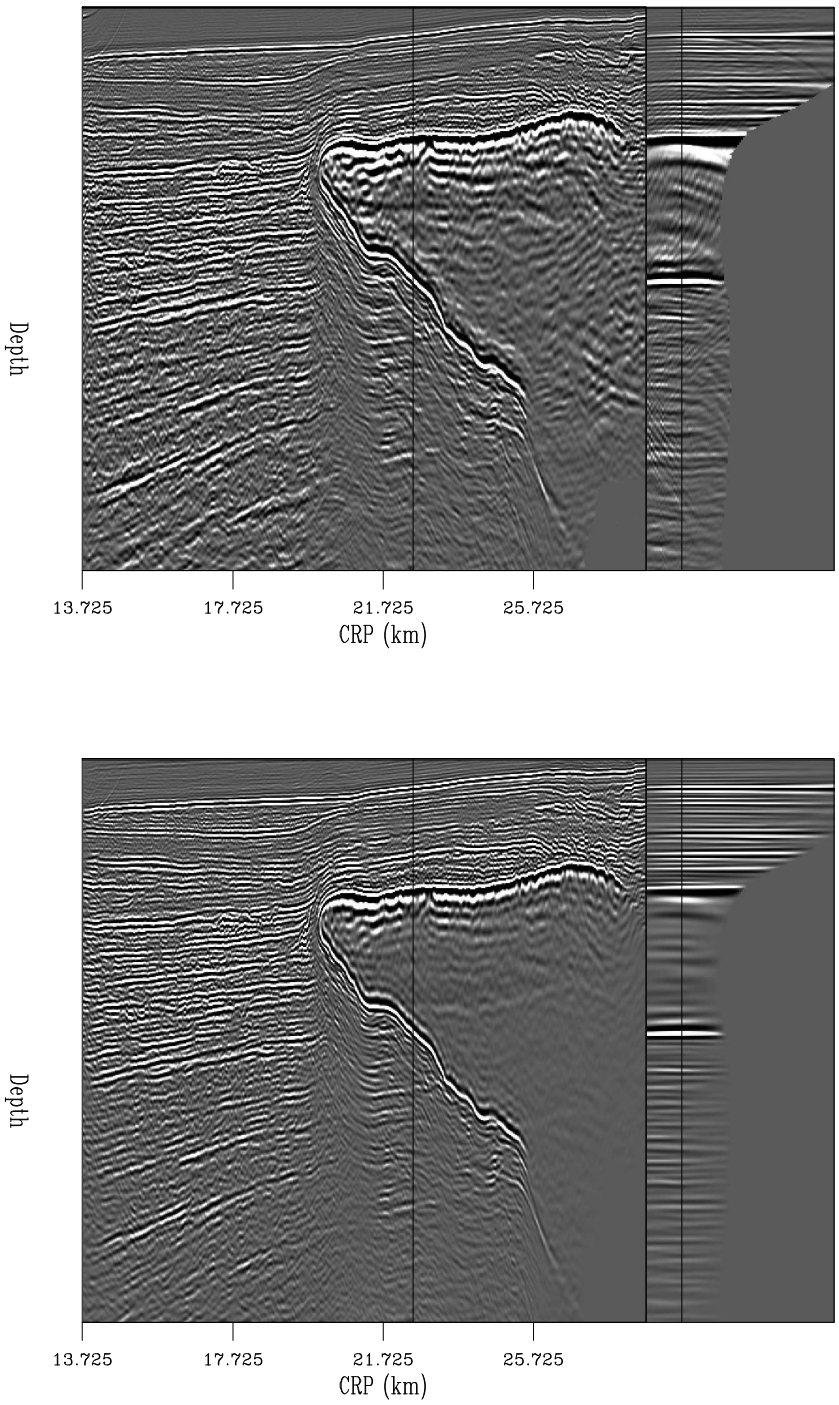

Figure 4.4: Top: result of downward-continuation migration of 2-D line. Left part is a common offset ray parameter section at $p_h = .1375$, right part is a common image gather from $CRP = 22.5$. Bottom: result of 6 iterations of geophysical RIP. real-bp2d.3 [CR,M]

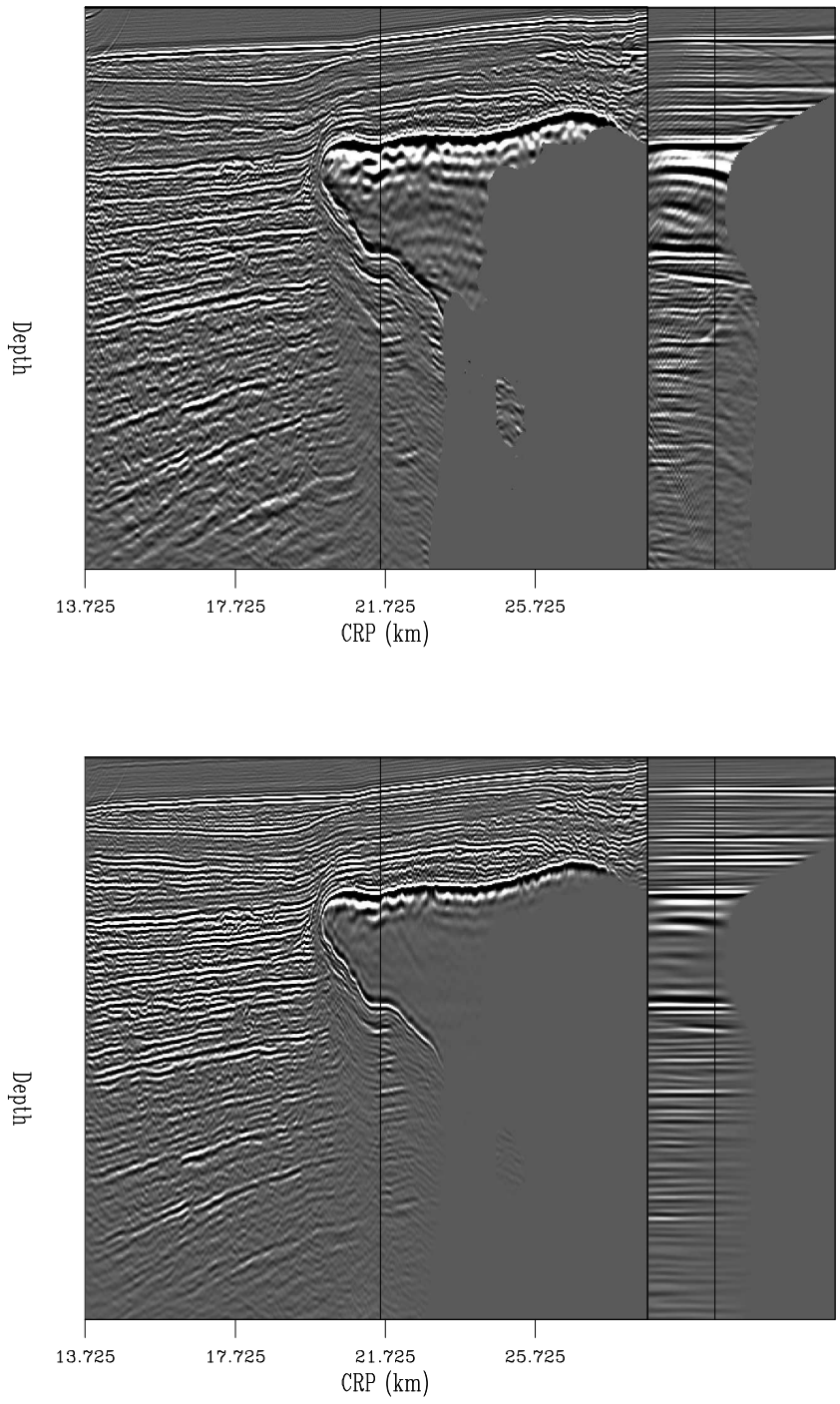

Figure 4.5: Top: result of downward-continuation migration of 2-D line. Left part is a common offset ray parameter section at $p_h = .265$, right part is a common image gather from $CRP = 21.575$. Bottom: result of 6 iterations of geophysical RIP. real-bp2d.2 [CR,M]

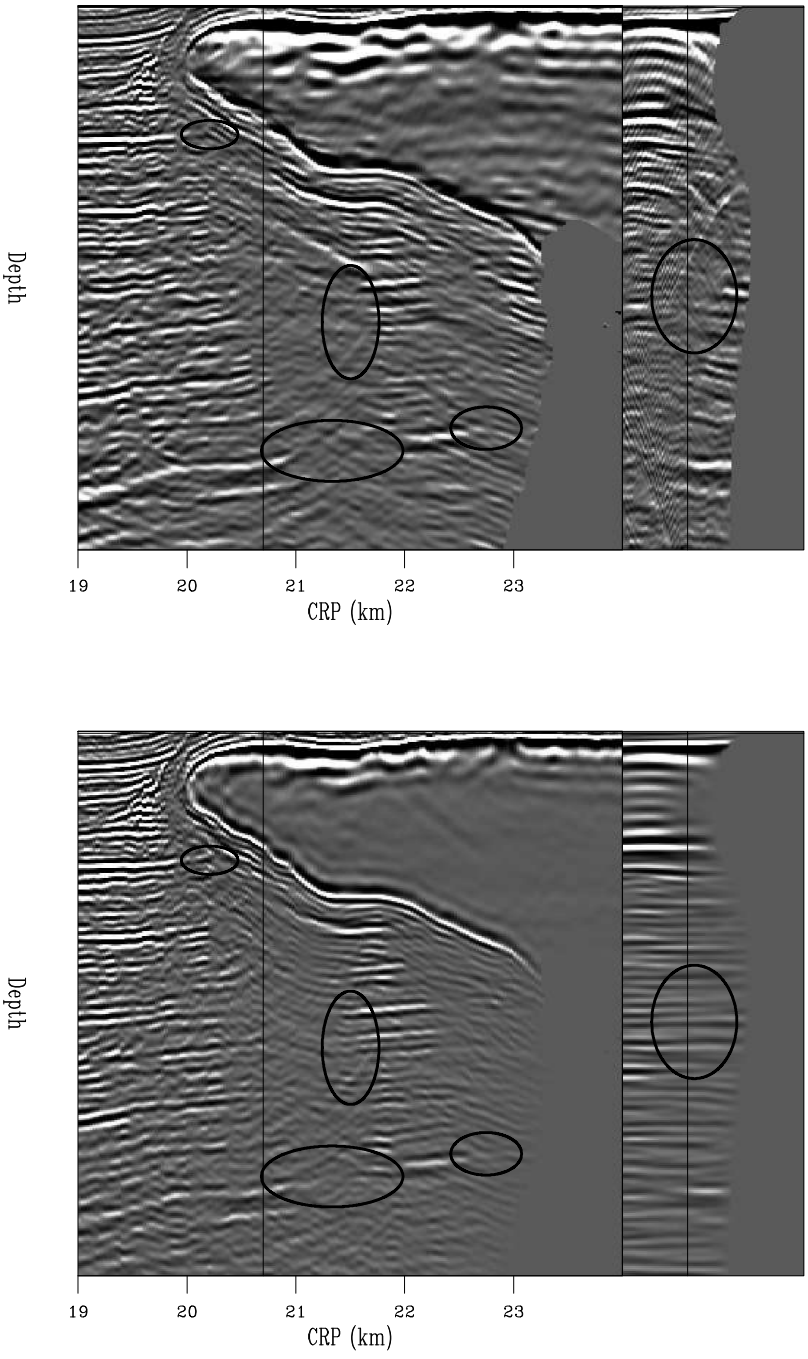

Figure 4.6: Zoomed portion of Figure 4.2. Top: result of downward-continuation migration of 2-D line. Left part is a common offset ray parameter section at $p_h = .265$, right part is a common image gather from $CRP = 20.675$. Bottom: result of 6 iterations of geophysical RIP. Ovals indicate areas where poor illumination exists in the migration result and is improved in the RIP result. real-zbp2d.1 [CR,M]

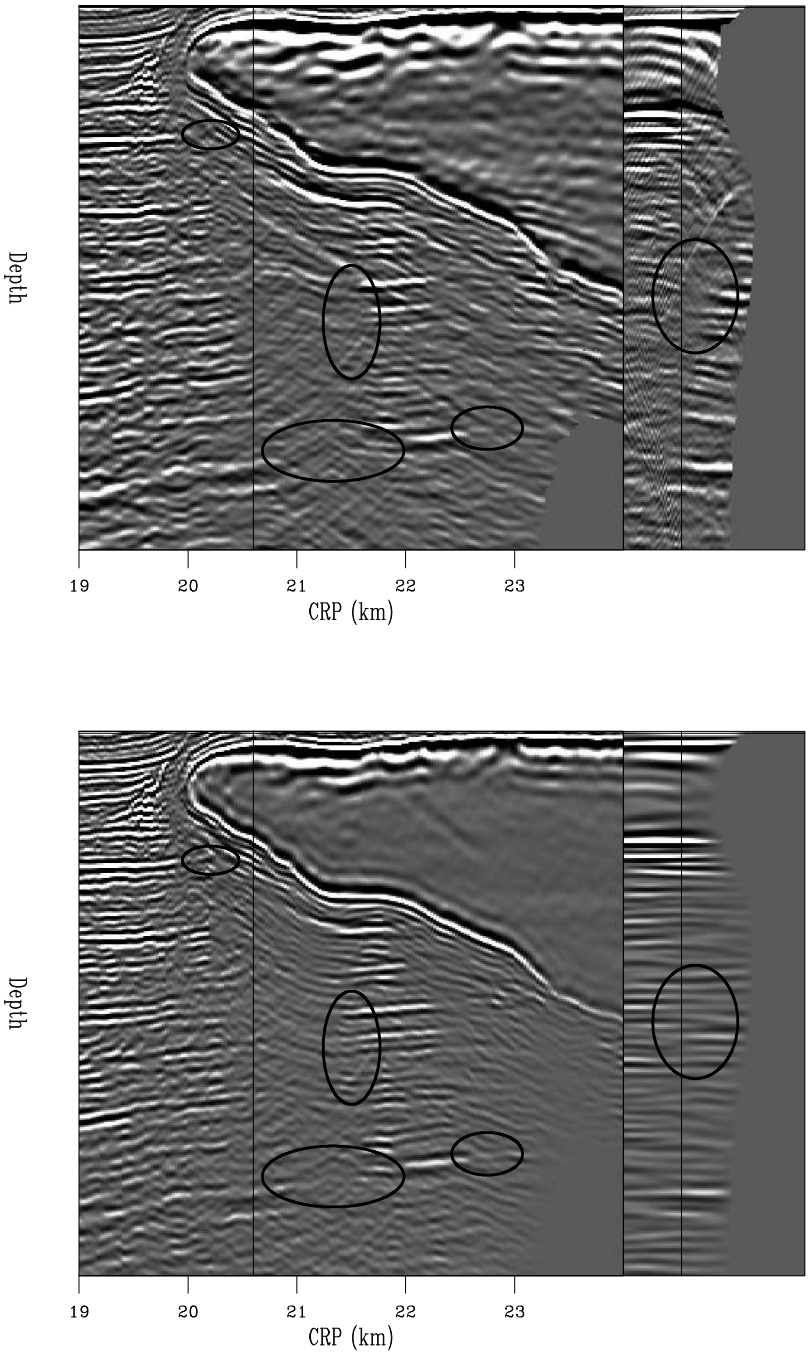

Figure 4.7: Zoomed portion of Figure 4.3. Top: result of downward-continuation migration of 2-D line. Left part is a common offset ray parameter section at $p_h = .235$, right part is a common image gather from $CRP = 20.575$. Bottom: result of 6 iterations of geophysical RIP. Ovals indicate areas where poor illumination exists in the migration result and is improved in the RIP result. real-zbp2d.4 [CR,M]

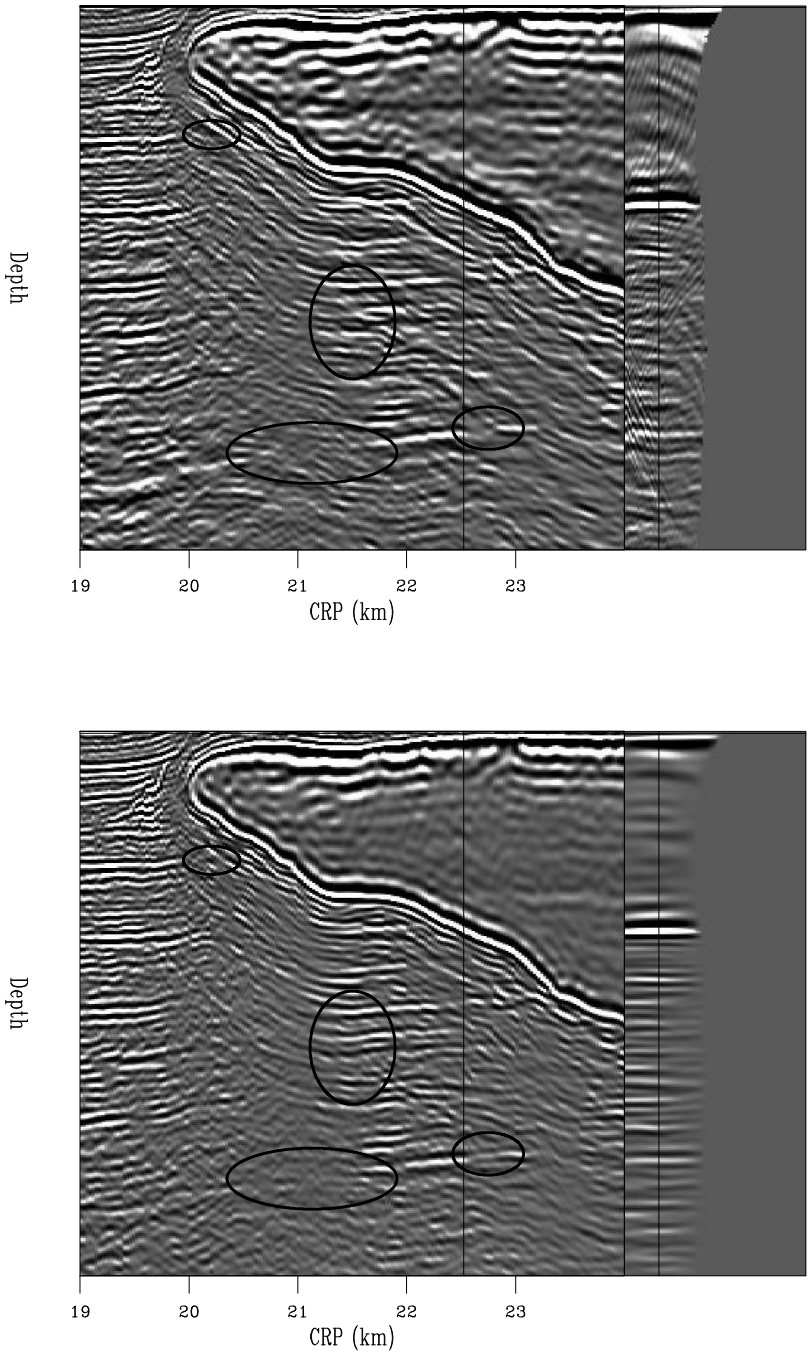

Figure 4.8: Zoomed portion of Figure 4.4. Top: result of downward-continuation migration of 2-D line. Left part is a common offset ray parameter section at $p_h = .1375$, right part is a common image gather from $CRP = 22.5$. Bottom: result of 6 iterations of geophysical RIP. Ovals indicate areas where poor illumination exists in the migration result and is improved in the RIP result. real-zbp2d.3 [CR,M]

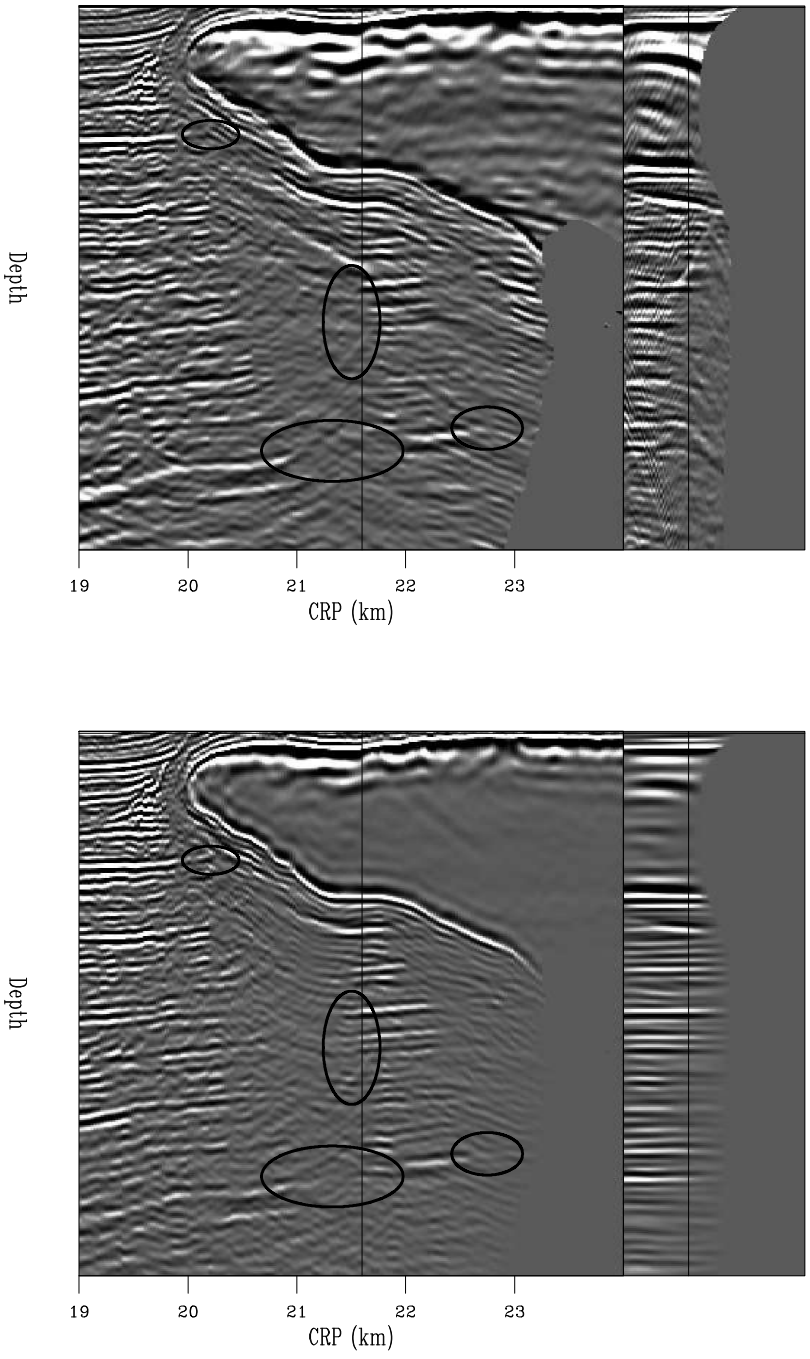

Figure 4.9: Zoomed portion of Figure 4.5. Top: result of downward-continuation migration of 2-D line. Left part is a common offset ray parameter section at $p_h = .265$, right part is a common image gather from $CRP = 21.575$. Bottom: result of 6 iterations of geophysical RIP. Ovals indicate areas where poor illumination exists in the migration result and is improved in the RIP result. real-zbp2d.2 [CR,M]

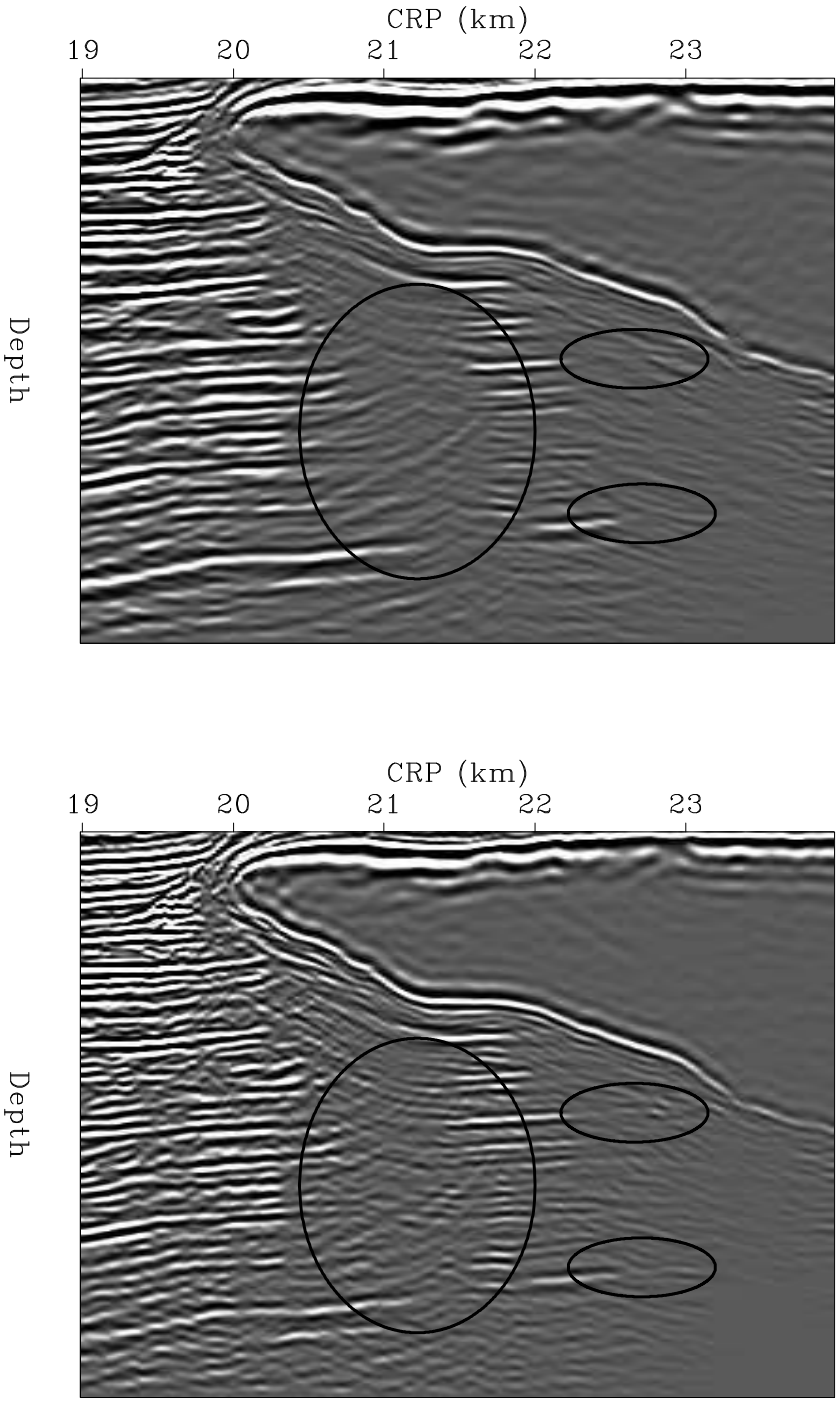

Figure 4.10: Top: stack of the result of downward-continuation migration of 2-D line. Bottom: stack of the result of 6 iterations of geophysical RIP. Ovals indicate areas where poor illumination exists in the migration result and is improved in the RIP result. real-zstackbp2d [CR,M]

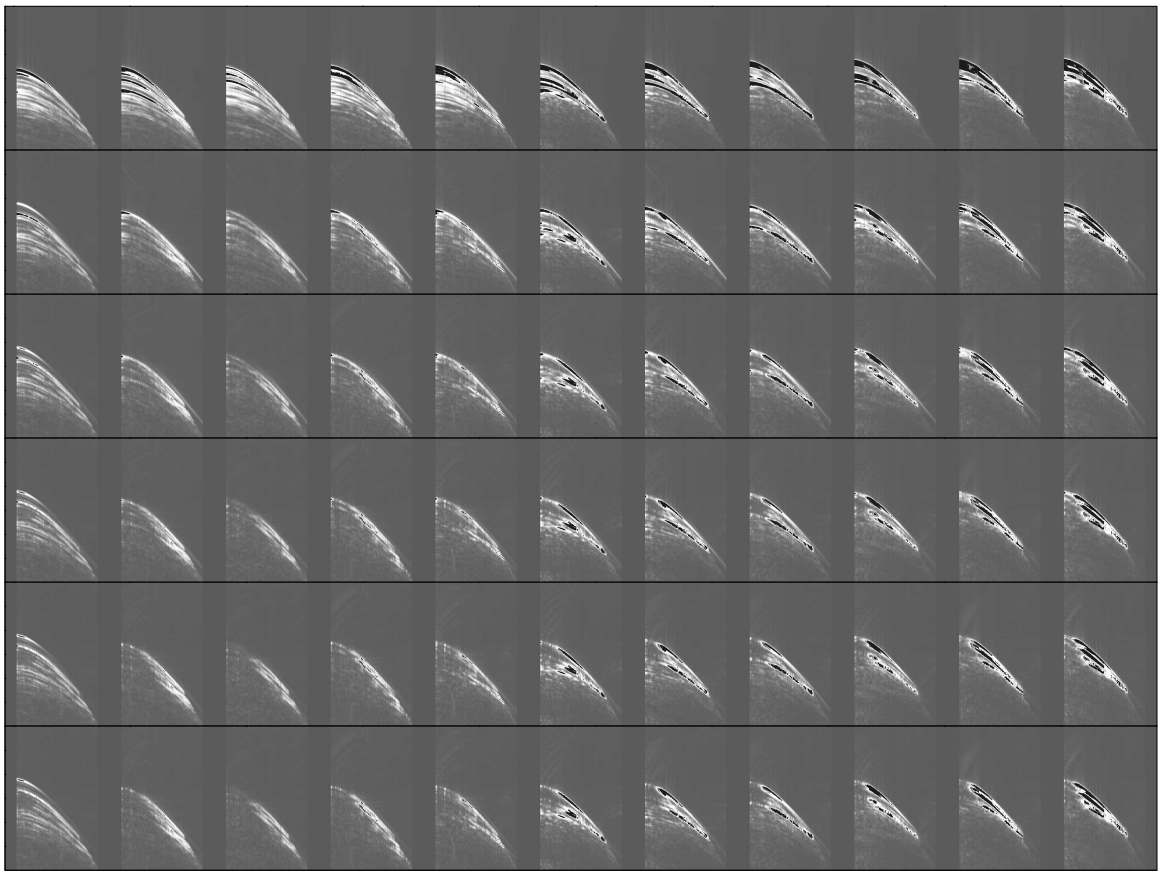

Figure 4.11: Comparison of the data space residuals from RIP with geophysical regularization. The vertical axis is time, the horizontal axis is offset. Each row is a collection of CMP gathers taken from locations across the whole survey, taking the envelope of the energy and clipping the high values (indicated by black). The first row is the original data, the second row shows the same CMP gathers after 2 iterations, the third row is after 4 iterations, fourth row after 6 iterations, fifth row after 8 iterations and sixth after 10 iterations. real-comp.resid [CR,M]

Geological RIP

Geological RIP allows us to incorporate a geological idea of what the model should look like into the inversion problem. I have picked several reflectors in the migration result (Figure 4.12) and used them to create a steering filter that is used to regularize the model along with the geophysical regularization.

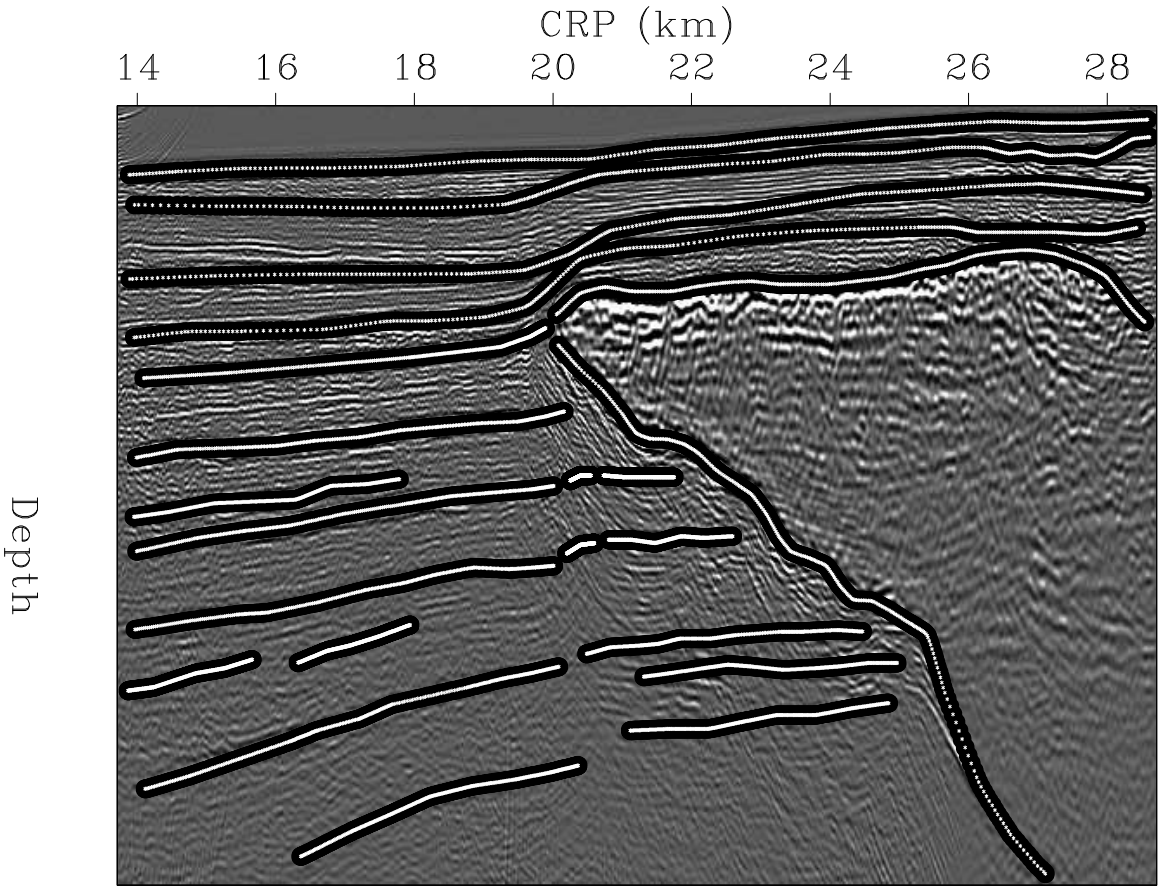

Figure 4.12: Migration result overlaid by the reflectors picked for geological regularization. real-bp.refl [CR]

The result of 6 iterations of geological RIP using the reflectors from Figure 4.12 can be seen in Figure 4.13. Once again, the migration result is displayed on top and the inversion result is displayed on the bottom. It can also be compared to the geophysical RIP result in Figure 4.2, which shows the same common ray parameter section and common image gather.

The geological RIP result has even fewer artifacts than the geophysical RIP result and shows more reflector continuity in the shadow zones. However, the faults are less defined in the geological RIP result.

3-D RESULTS

To apply RIP to 3-D data, I chose to change my migration operator from the downward-continuation migration described in Chapter 2 to common azimuth migration (Biondi and Palacharla, 1996). This helps to keep my computational needs relatively low for a 3-D imaging problem. It also means that I will only be handling the inline offsets, so geophysical RIP will only be acting along the inline offset ray parameter. I have chosen to apply only geophysical RIP on this 3-D problem.

Comparison of 3-D stacked results

The stack of the common azimuth migration (CAM) result (upper panels of Figures 4.14 and 4.15) of this 3-D cube is good, indicating that the velocity model is fairly accurate. There are 3-D faults visible away from the salt. Under the salt, the shadow zones caused by poor illumination are easy to identify, although they are full of noise and artifacts.

I performed 7 iterations of 3-D geophysical RIP. The result of the stack can be seen in the lower panels of Figure 4.14 and Figure 4.15. The two figures display different inline, crossline, and depth slices, but the types of improvements are the same. In both figures, ovals on the stacked migration result and the stacked geophysical RIP result indicate particular areas where RIP has improved the image. The improvements are fairly modest, due to the small number of iterations performed.

The ovals marked as “A” appear on the depth slices and indicate increased resolution of faults that are located away from the salt, but whose imaging depends on energy that has been affected by passing through the salt. The ovals marked as “B” indicate reflectors close beneath the nose of the salt which have more consistent amplitudes in the RIP results. The greatest improvement can be seen in oval “C”, where the migration results show a strong up-sweeping

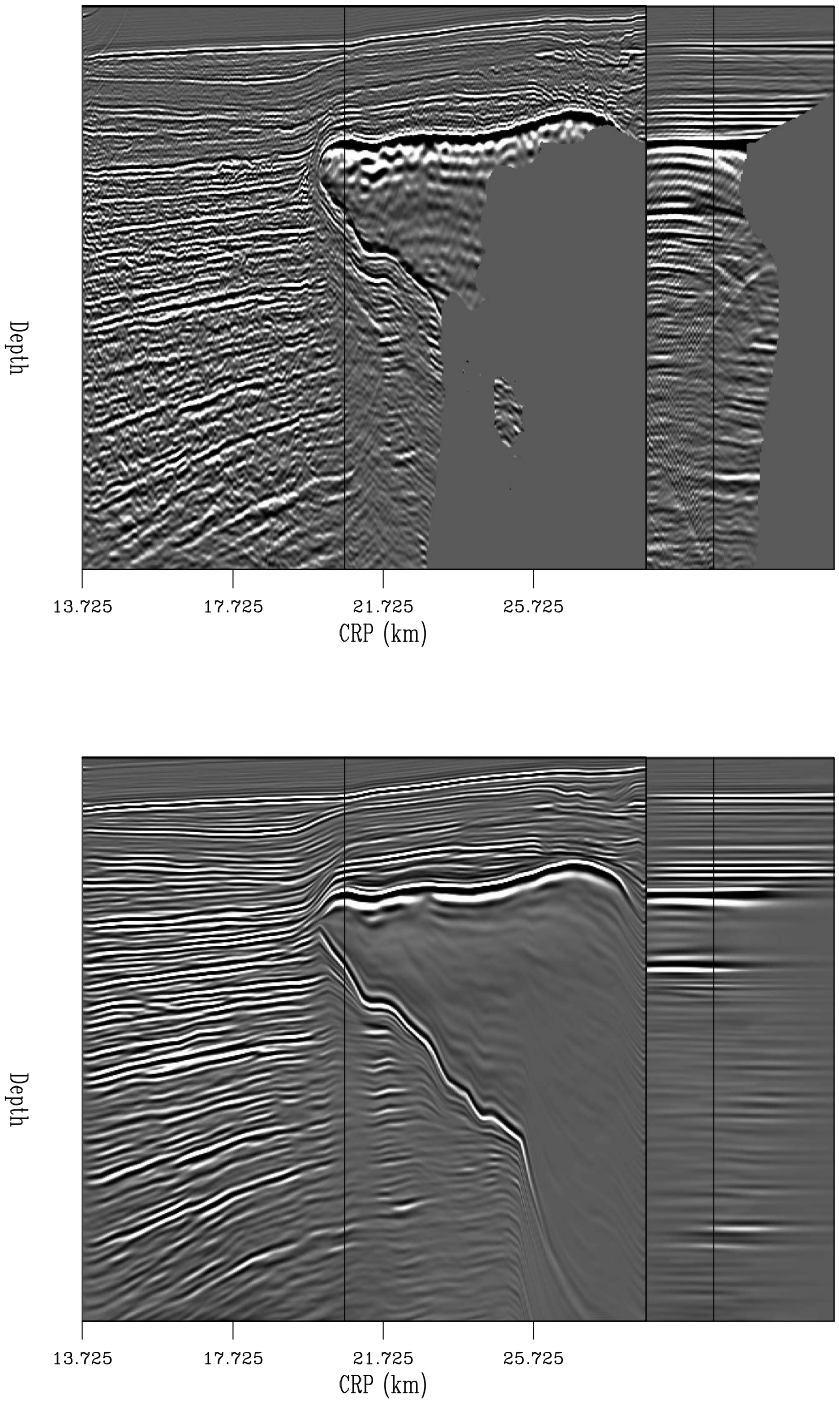

Figure 4.13: Top: result of downward-continuation migration of 2-D line. Left part is a common offset ray parameter section at $p_h = .265$, right part is a common image gather from $CRP = 20.675$. Bottom: result of 6 iterations of geological RIP. This result can also be compared to the geophysical RIP result in Figure 4.2. real-lbp2d.1 [CR,M]

artifact in the shadow zone that has been significantly reduced in the RIP results. With that artifact gone, the improvement in the imaging of the reflector passing through the center of the oval is more obvious. After 7 iterations of RIP, this reflector can be traced, though weakly, through almost the entire shadow zone. The ovals marked “D” indicate a fault beneath the salt that is better imaged with RIP.

The improvements made by RIP can be seen better by zooming in under the salt. Figures 4.16 and 4.17 show the stacked 3-D migration on top and the stacked RIP result after 7 iterations on the bottom. In Fig. 4.16, oval “A” indicates reflectors that can be followed under the salt nose after imaging with RIP. Ovals “B”, “C”, and “D” show areas on the inline section where the reflectors can be traced almost entirely through the shadow zones after RIP. In the crossline section, many more reflectors are seen after RIP, particularly in oval “E”. In Fig. 4.17, ovals “A”,“B”, and “C” show areas on the inline section where the reflectors can be traced almost entirely through the shadow zones after RIP and oval “D” shows reflectors and a possible fault in the crossline section.

It is not surprising that the comparison of the migration stack and the RIP stack show less impressive improvements than seen in the 2-D example. Performing only 7 iterations of geophysical RIP, which is regularizing only the inline p_h axis, will not change the image enough to show significant effects in the stacked volumes. Although there were more substantial improvements in the stacks after 6 iterations of RIP on a 2-D line taken from this dataset (Fig. 4.10), inverting a 3-D problem means that it can take many more iterations to get similar improvements.

Comparison of unstacked inline results

Using CAM as the imaging operator in my least-squares inversion means that my geophysical regularization operator will only be acting along the inline p_h axis. Therefore, the most significant changes between the CAM result and the geophysical RIP result will be seen in unstacked results. To study these, I have selected several unstacked inline volumes from crossline=20.9 km. These volumes can be seen in Figures 4.18 through 4.25, where (if you rotate the pages 90^o clockwise) I am displaying the depth slice on the top of the figure, the common inline p_h

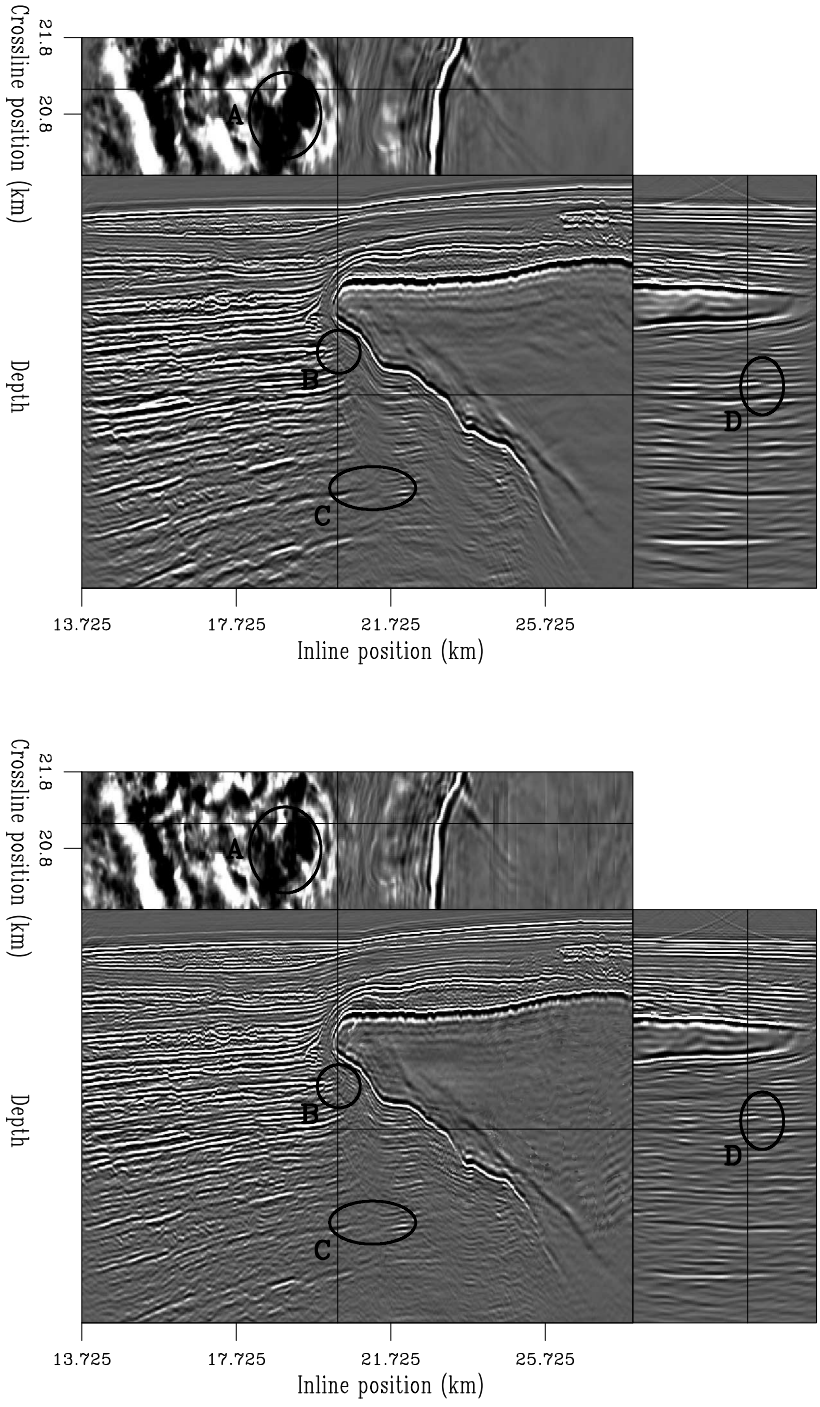

Figure 4.14: 3-D image displayed with depth slice, inline section from crossline=21.125 km and crossline section from inline=20.35 km. Top: stack after common azimuth migration. Bottom: stack after 7 iterations of geophysical RIP. Ovals indicate areas of particular improvement in the RIP result. real-stack3d.1 [CR,M]

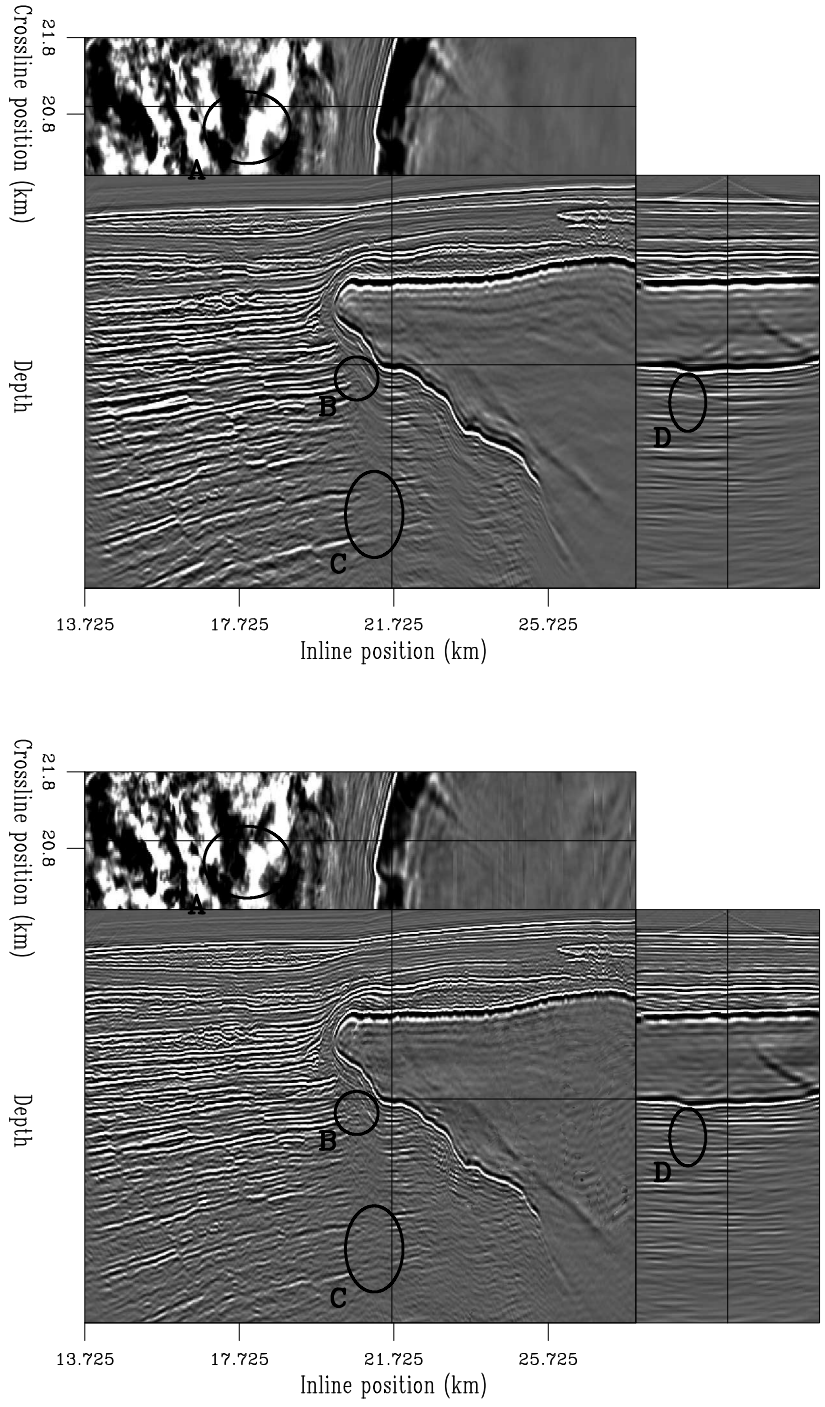

Figure 4.15: 3-D image displayed with depth slice, inline section from crossline=20.9 km and crossline section from inline=21.675 km. Top: stack after common azimuth migration. Bottom: stack after 7 iterations of geophysical RIP. Ovals indicate areas of particular improvement in the RIP result. real-stack3d.2 [CR,M]

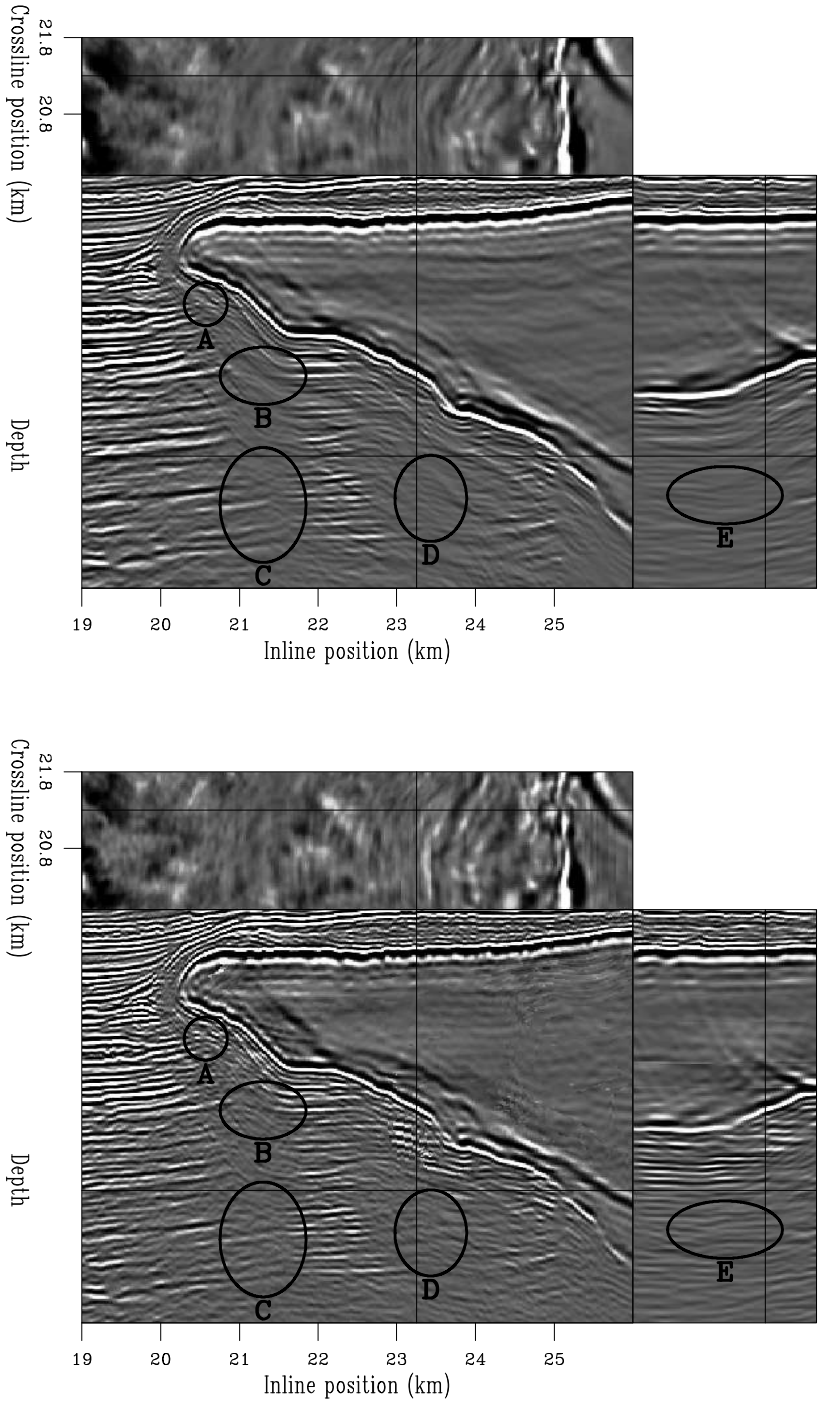

Figure 4.16: Zoomed 3-D image displayed with depth slice, inline section from crossline=21.3 km and crossline section from inline=23.25 km. Top: stack after common azimuth migration. Bottom: stack after 7 iterations of geophysical RIP. Ovals indicate areas of particular improvement in the RIP result. real-zstack3d.1 [CR,M]

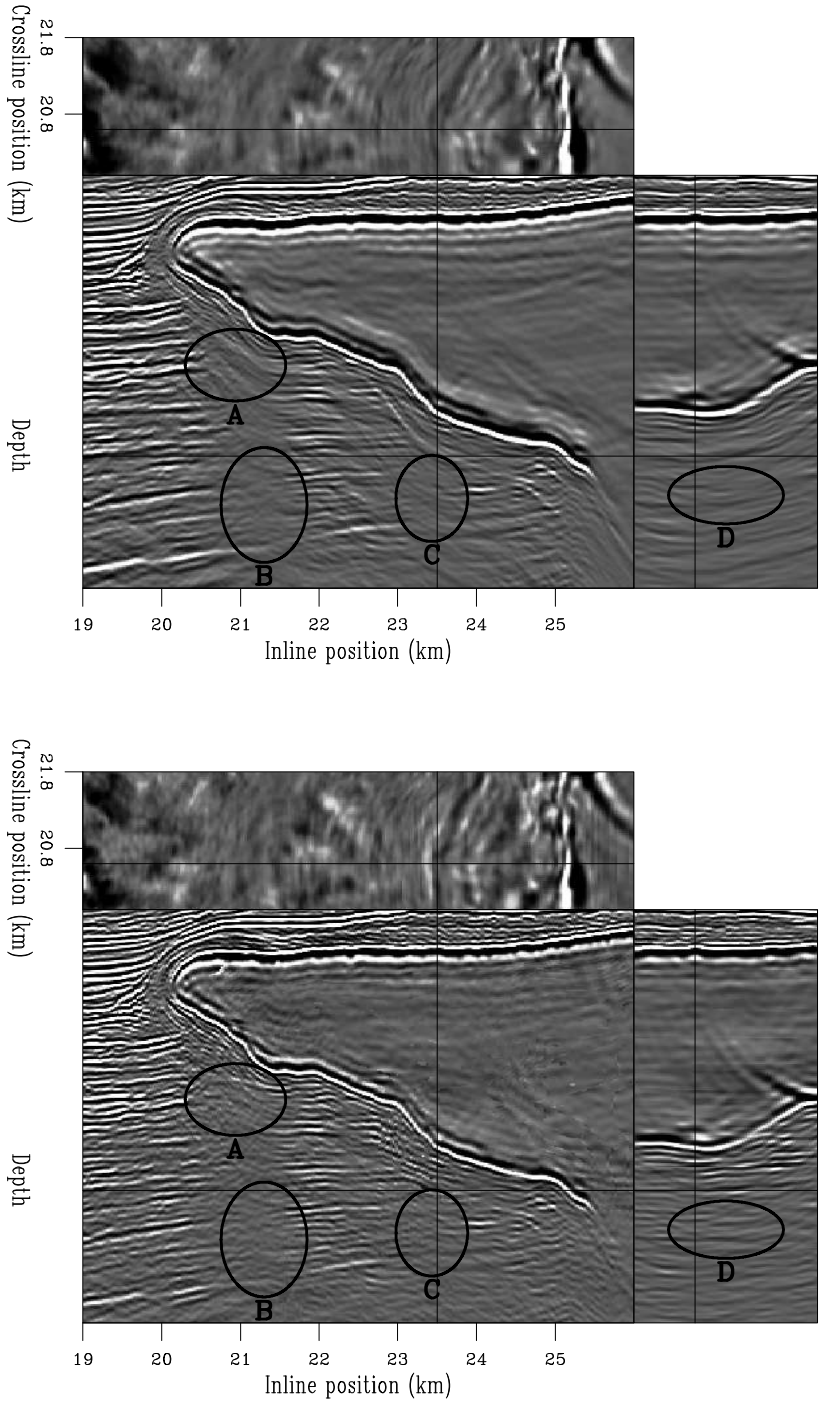

Figure 4.17: Zoomed 3-D image displayed with depth slice, inline section from crossline=20.6 km and crossline section from inline=23.5 km. Top: stack after common azimuth migration. Bottom: stack after 7 iterations of geophysical RIP. Ovals indicate areas of particular improvement in the RIP result. real-zstack3d.2 [CR,M]

section on the left, and the common image gather to the right of the common inline p_h section. The migration result is shown first, then the geophysical RIP result for each (common inline p_h section - common image gather) pair.

Figures 4.18 and 4.19 show a common inline p_h section from $p_h = .1875$ and a common image gather from inline position 20.375 km. Comparing Figure 4.18 and Figure 4.19, the RIP result is considerably cleaner. The effects of the regularization are clear in the common image gather (right part of the figures), where the unlabeled oval indicates gaps in the events that are filled by RIP. In the common inline p_h section, the ovals indicate particular areas of the shadow zones that are being filled in. Oval "A" highlights a reflector that is discontinuous and has inconsistent amplitudes where it does exist in the migration result. In the RIP result, this reflector is continuous with strong amplitudes along its full extent. Oval "B" extends across one of the shadow zones. The shadow zone is considerably cleaner in the RIP result, with almost none of the up-sweeping artifacts seen in the migration result. Also, the reflectors themselves extend farther into the shadow zone, particularly on the right side of the oval. The events also extend farther into the shadow zone indicated by oval "C".

Moving further under the salt and to a larger offset ray parameter, Figures 4.20 and 4.21 show a common inline p_h section from $p_h = .2325$ and a common image gather from inline position 21.65 km. The unlabeled oval in the common image gather shows events that have been strengthen and are more horizontal in the RIP result (Fig. 4.21) than the migration result (Fig. 4.20). The ovals marked "A", "B", and "C" on the common p_h sections show the same type of improvement seen in the previous comparison (Figs. 4.18 and 4.19). The reflectors at the right side of oval "B" in Figure 4.21 extend much farther into the shadow zone than those from the migration result.

Another interesting comparison can be made at common inline p_h section from $p_h = .15$ and a common image gather from inline position 20.9 km (Figures 4.22 and 4.23). In this migration result (Fig. 4.22), the common image gather once again has events with gaps caused by poor illumination, indicated by the unlabeled oval. These gaps are largely filled by 7 iterations of RIP, as seen in Figure 4.23. We see the same improvements in ovals "A", "B", and "C" as discussed for the previous two comparisons. In this comparison, there is an additional oval "D" that indicated reflectors under the salt that are less affected by artifacts and more

likely to be accurate in the RIP result than in the migration result.

Finally, looking at the same common image gather from inline position 20.9 km but moving the common inline p_h section to $p_h = .2925$, we compare Figures 4.24 and 4.25. In this common p_h section, the effect of the critical angle and user-defined mutes described in the previous chapter can be seen in and below the salt body. The oval in the common image gather shows the same events with gaps in the migration result (Fig. 4.24) that are filled by RIP (Fig. 4.25) that was seen in the previous comparison. It is interesting to see that the improvements seen in the “A”, “B”, and “C” ovals in the previous examples are also seen in this example, at a much larger p_h. RIP has a positive effect for a large range of p_h.

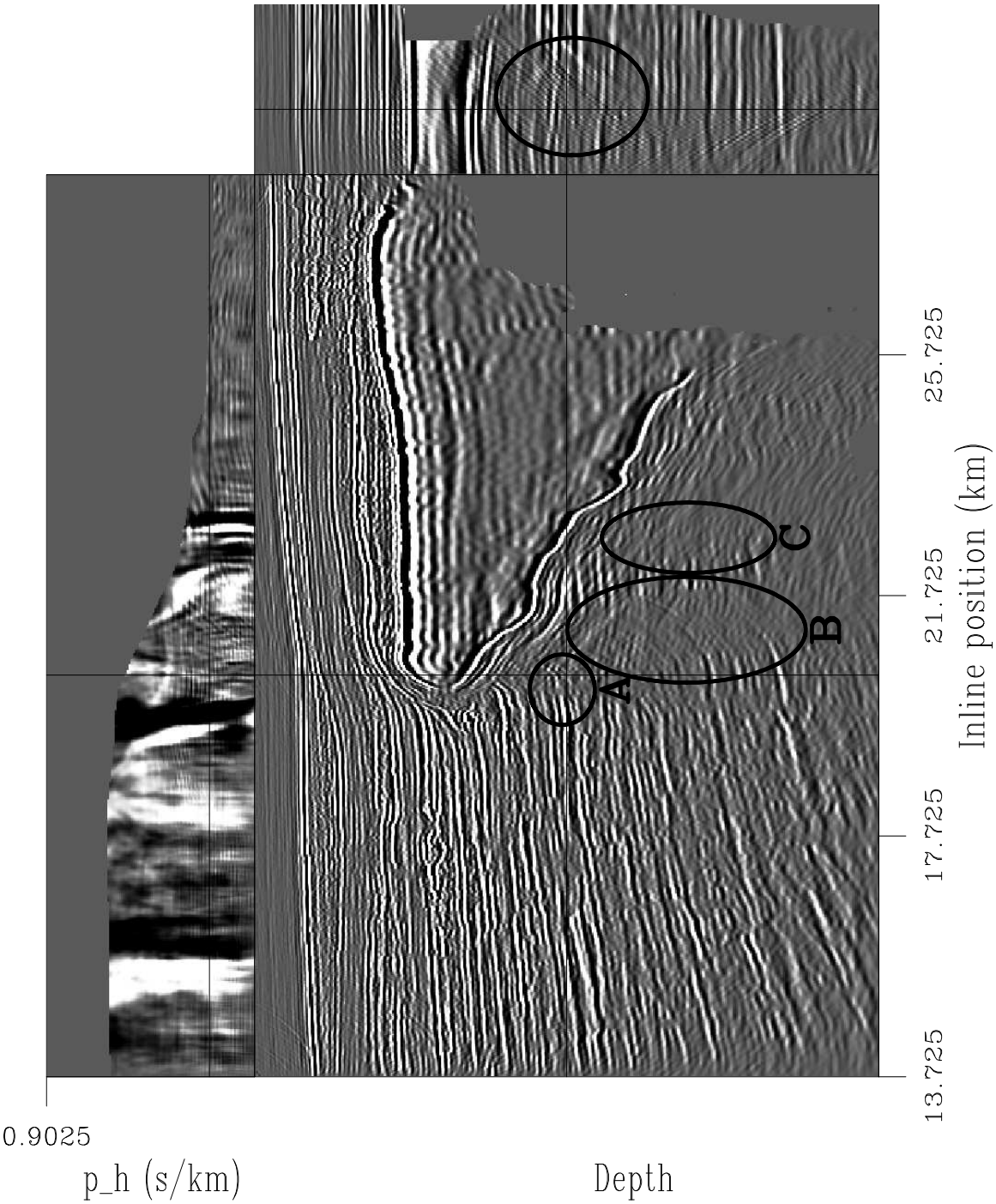

Figure 4.18: Migration result. Crossline=20.9 km, common inline p_h section from $p_h = .1875$, and common image gather from inline=20.375 km. Compare with Figure 4.19. real-bp3d.mig.1 [CR]

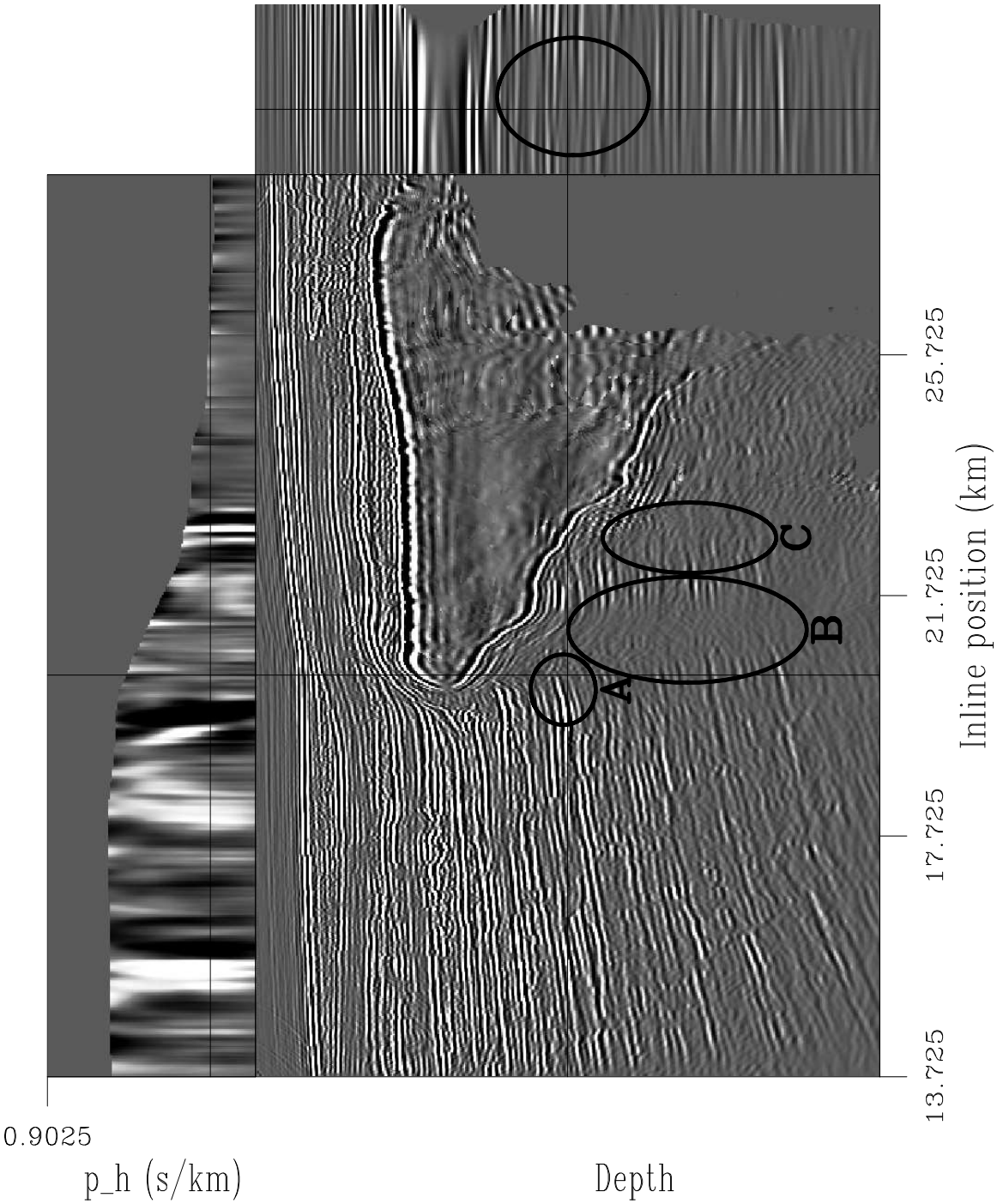

Figure 4.19: Geophysical RIP result. Crossline=20.9 km, common inline p_h section from $p_h = .1875$, and common image gather from inline=20.375 km. Compare with Figure 4.18. real-bp3d.geop.1 [CR]

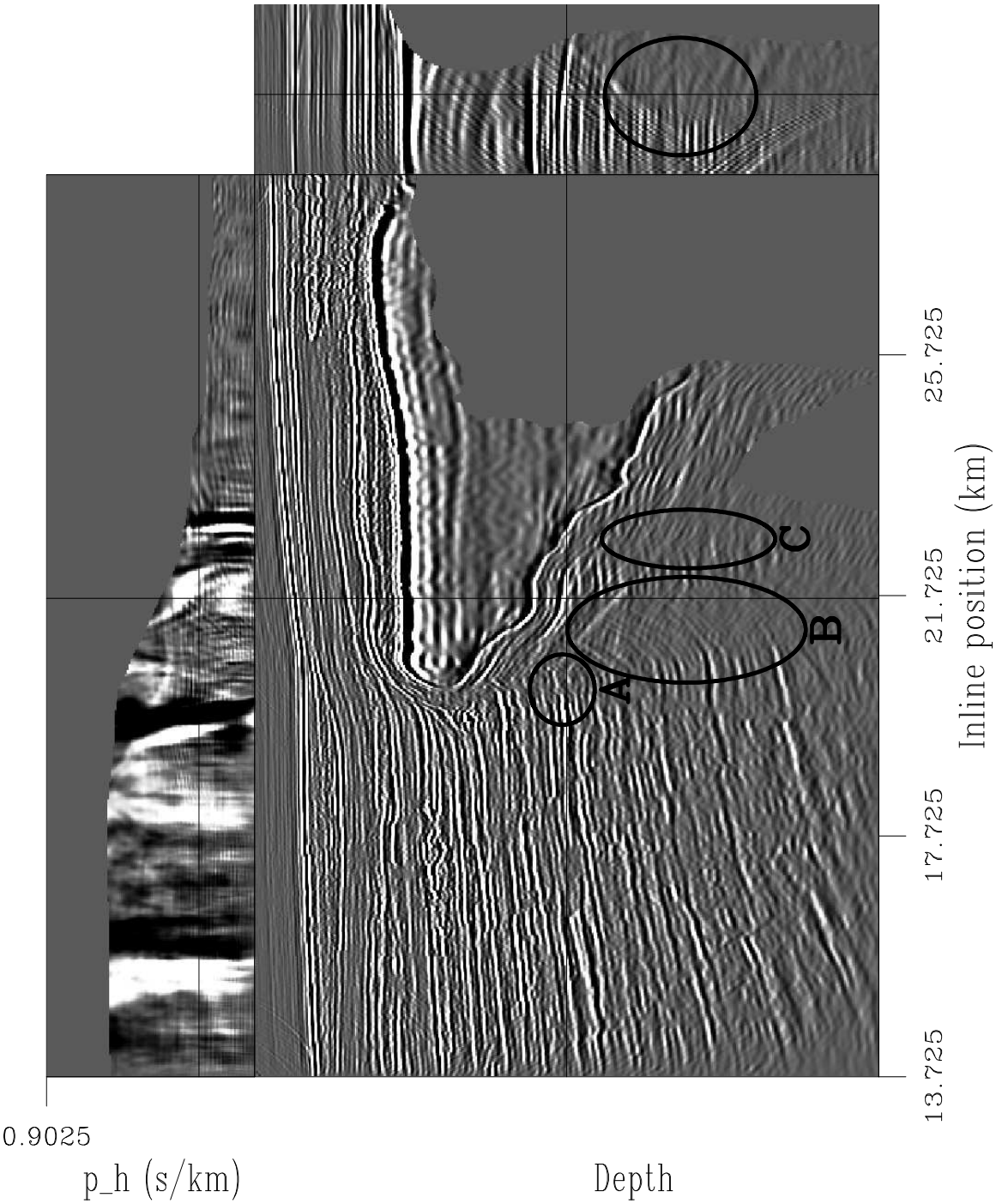

Figure 4.20: Migration result. Crossline=20.9 km, common inline p_h section from $p_h = .2325$, and common image gather from inline=21.65 km. Compare with Figure 4.21. real-bp3d.mig.2 [CR]

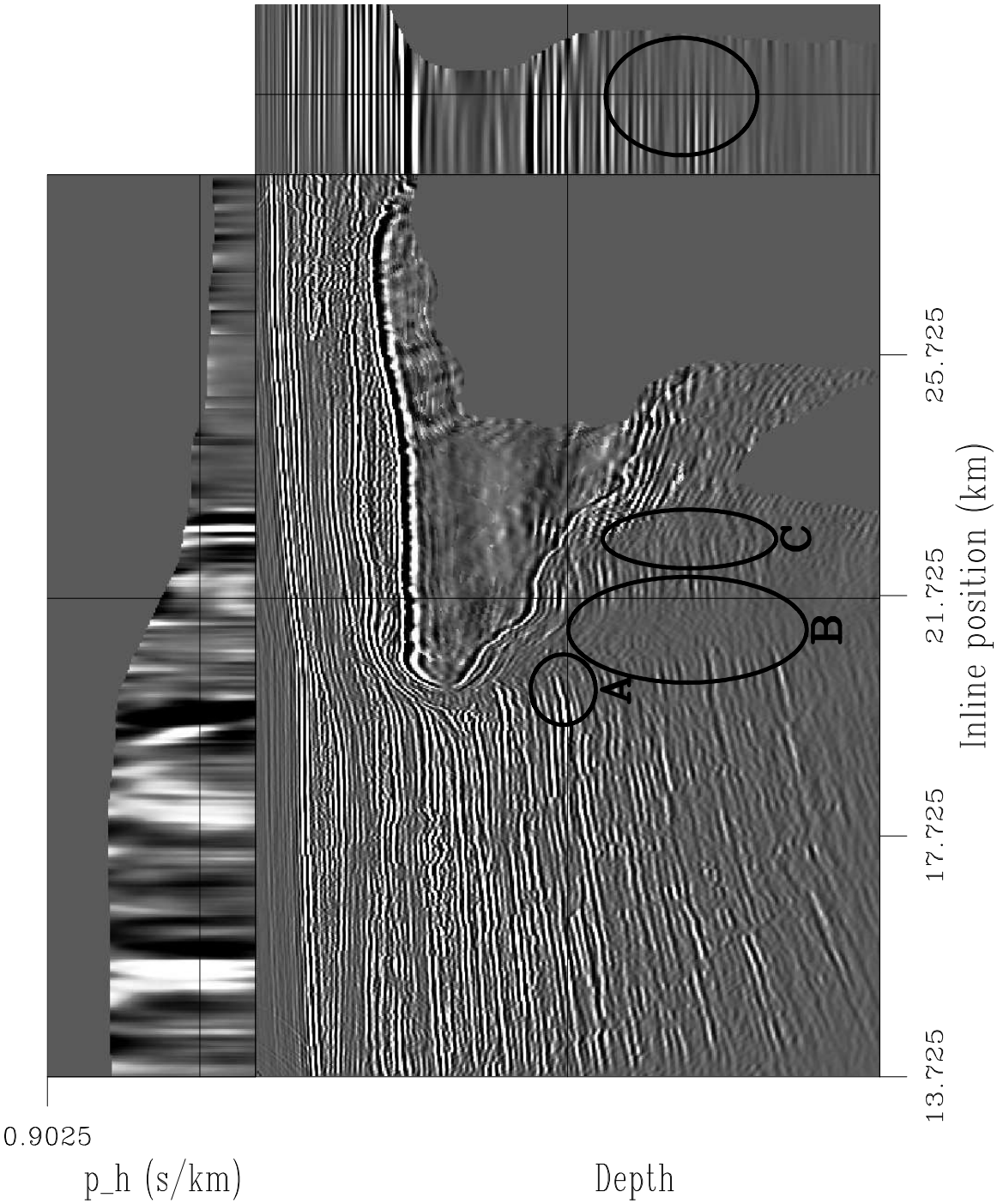

Figure 4.21: Geophysical RIP result. Crossline=20.9 km, common inline p_h section from $p_h = .2325$, and common image gather from inline=21.65 km. Compare with Figure 4.20. real-bp3d.geop.2 [CR]

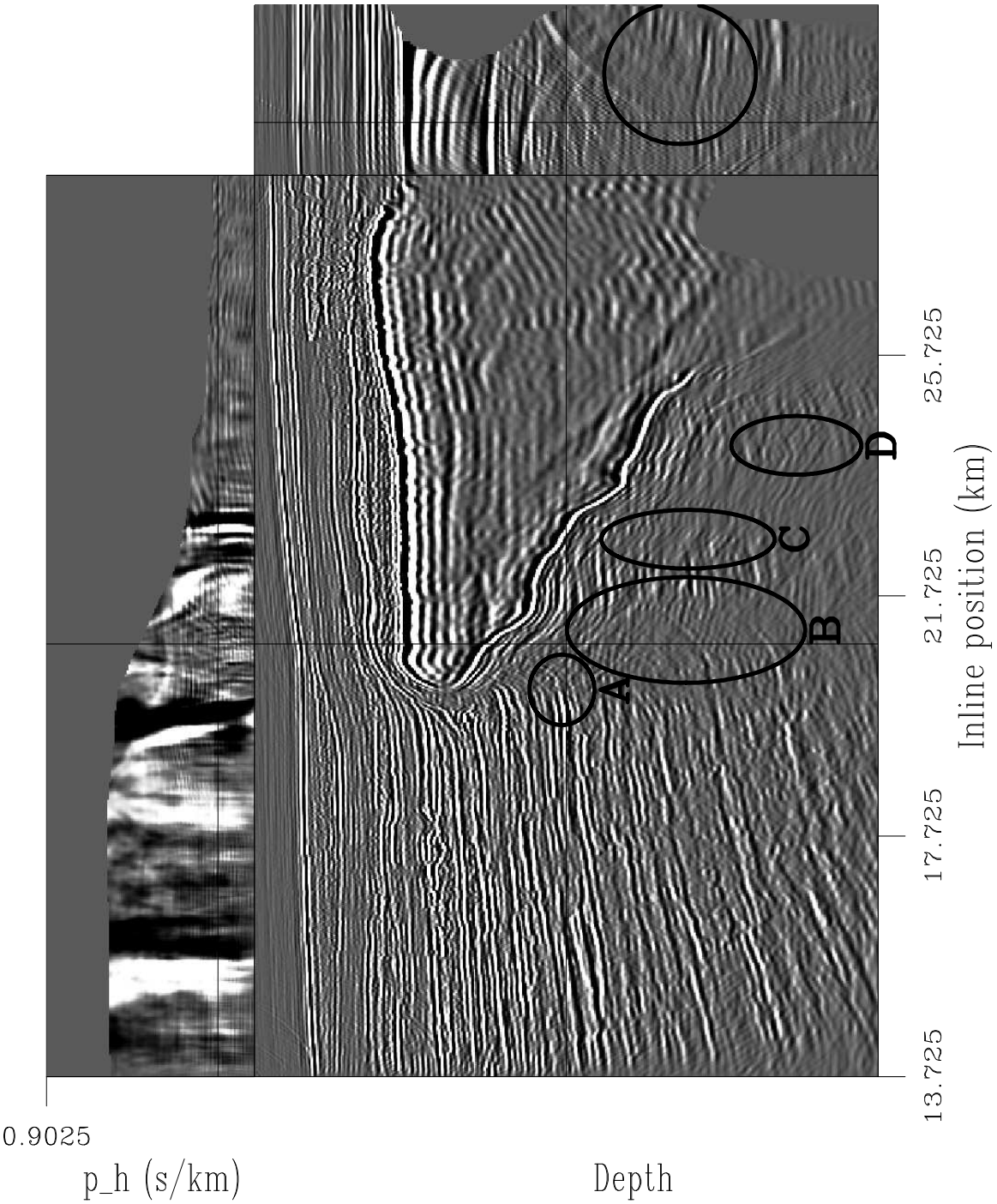

Figure 4.22: Migration result. Crossline=20.9 km, common inline p_h section from $p_h = .15$, and common image gather from inline=20.9 km. Compare with Figure 4.23. real-bp3d.mig.3 [CR]

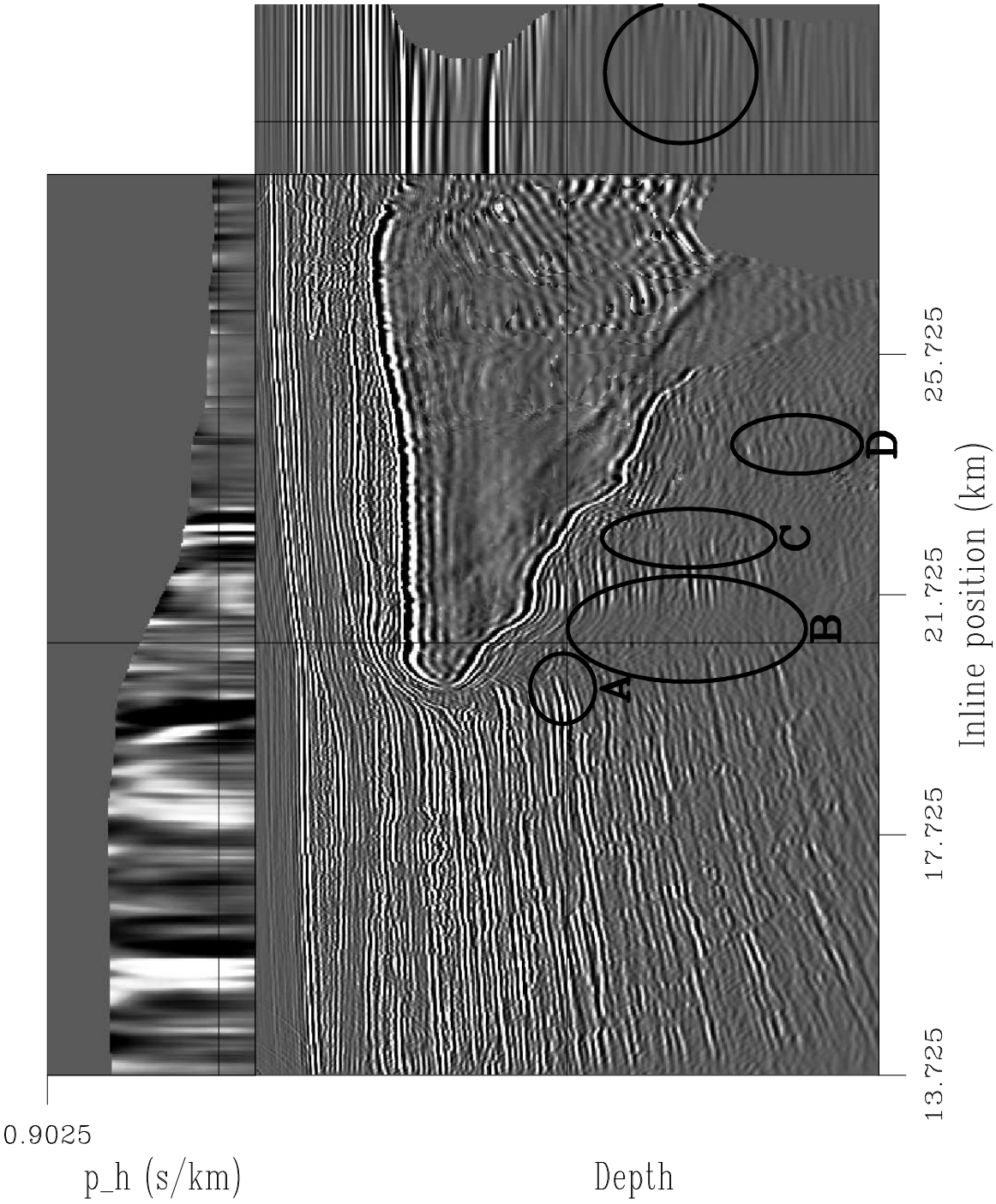

Figure 4.23: Geophysical RIP result. Crossline=20.9 km, common inline p_h section from $p_h = .15$, and common image gather from inline= 20.9 km. Compare with Figure 4.22. real-bp3d.geop.3 [CR]

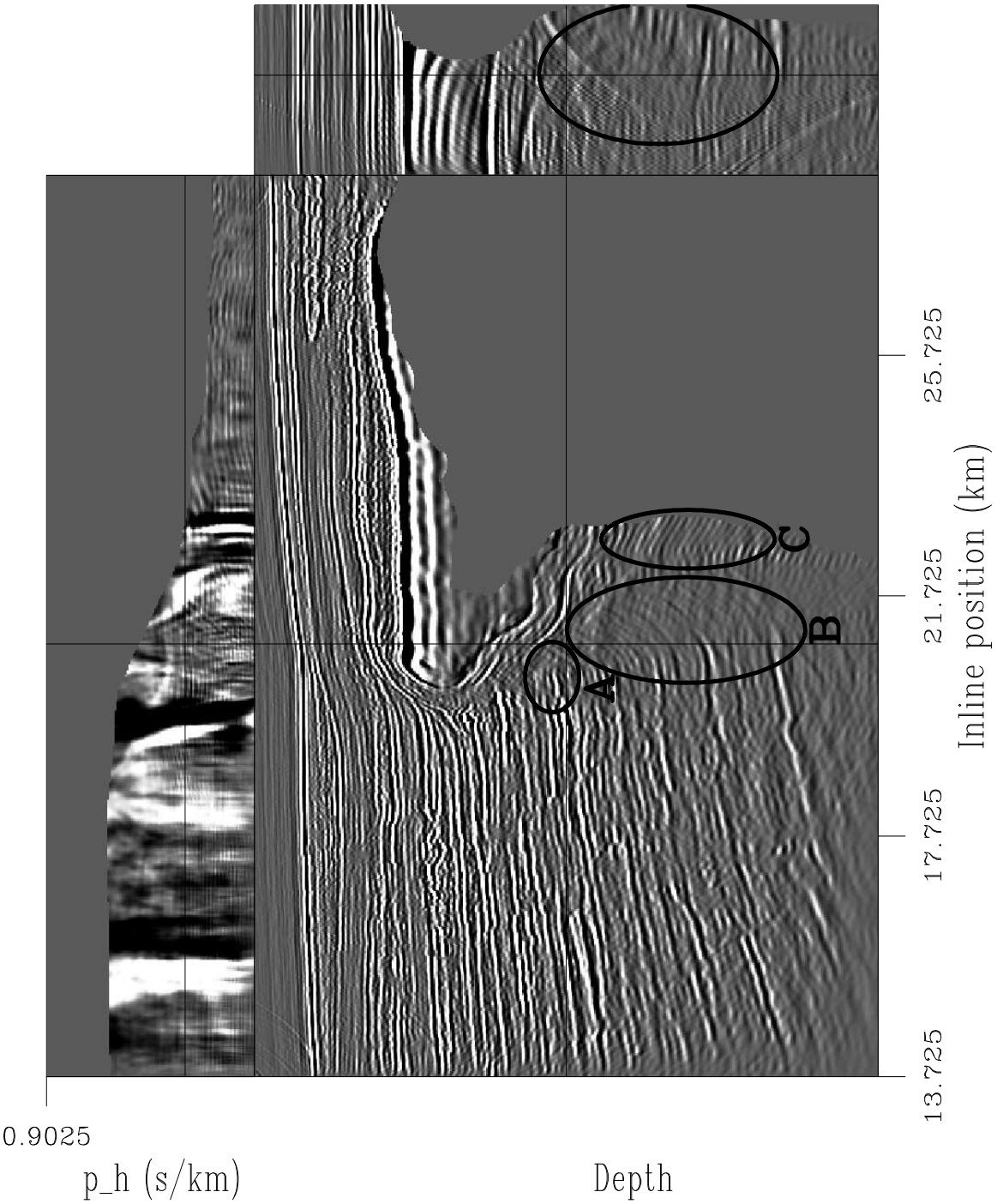

Figure 4.24: Migration result. Crossline=20.9 km, common inline p_h section from $p_h = .2925$, and common image gather from inline=20.9 km. Compare with Figure 4.25. real-bp3d.mig.4 [CR]

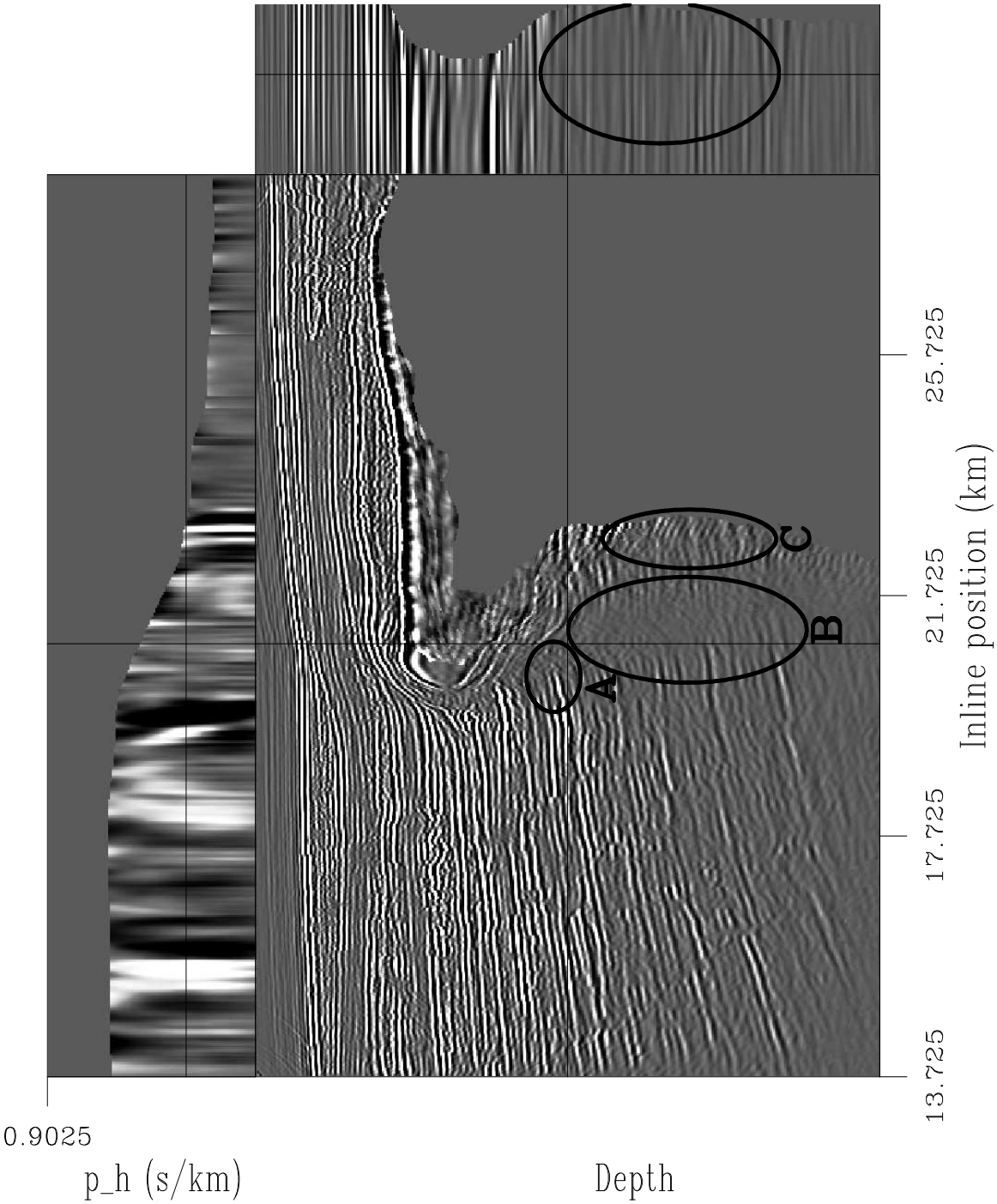

Figure 4.25: Geophysical RIP result. Crossline=20.9 km, common inline p_h section from $p_h = .2925$, and common image gather from inline=20.9 km. Compare with Figure 4.24. real-bp3d.geop.4 [CR]

Chapter 5

Summary

The problem of subsurface imaging in poorly illuminated areas is an increasingly important one. Our search for hydrocarbons often concentrates on the potential reservoirs near salt bodies in the subsurface, often under deep water. The strong velocity contrast between the salt and the surrounding rock causes seismic energy to be redirected or become evanescent. This energy will not be recorded during the seismic survey, resulting in poor illumination. In such areas, the high cost of drilling wells makes accurate imaging essential, and justifies algorithms that have a high computational cost.

Subsurface imaging is typically done with a migration algorithm. In complex areas such as those around salt bodies, it is common to use some type of wave-equation depth migration. The 2-D migration algorithm used in this thesis is a downward-continuation migration and the 3-D migration algorithm is a common azimuth migration. Both generate angle-domain (offset ray parameter) common image gathers. When using these migration algorithms, poor illumination will be manifested in the common image gathers as gaps in the events. It will appear as shadow zones in the Common Reflection Point (CRP)-depth plane. It is not possible for a migration algorithm to compensate for seismic energy that has been directed outside of the survey bounds. Fortunately, it is possible to use a migration operator in a least-squares inversion to obtain a better seismic image than that obtained from migration alone.

The inversion algorithm I described in this thesis, Regularized Inversion with model Preconditioning (RIP), can be designed to improve imaging in poorly illuminated areas. RIP is a regularized least-squares inversion that uses not only the migration operator but also a regularization operator to compensate for the sudden amplitude decrease that occurs when a seismic event passes into a shadow zone. Geophysical regularization acts along the offset ray parameter (equivalent to reflection angle) axis. It can be thought of as a derivative operator that minimizes large changes in amplitude. This geophysical regularization can be combined with geological regularization, which acts along specified dips in the CRP-depth plane. The geological regularization operator is a steering filter composed of dip annihilator filters at every point in the model. The geological regularization operator is created by an interpreter from a migration result or a geological model.

The geophysical regularization acts horizontally along the offset ray parameter axis, which means that the velocity model used for the migration should be correct to get the best results. However, as long as the velocities are reasonably close so that the moveout is fairly small, geophysical RIP will still provide a better image than migration alone.

Geological RIP has its own difficulties. The geological regularization operator is dependent on an interpreter's idea of how the seismic events should behave in the CRP-depth plane. If the geological regularization conflicts with recorded data, the inversion process will reject the attempted regularization.

The regularization, by filling in the gaps caused by poor illumination in the model, can be thought of as recovering seismic energy that was directed outside of the survey bounds. To keep this energy, we must pad the dataspace so it has somewhere to go. When calculating the residual in the conjugate gradient step, this energy must be masked out or the inversion will try to suppress it. In addition to this energy, the regularization also introduces frequencies into the model that are not included in the original data. Therefore we must pad the frequencies as well. These must also be masked out during the calculation of the residual.

Regularized inversion with model preconditioning is a framework that can be used for many different problems with many different regularization schemes. Concentrating on the problem of poor illumination, it is possible that RIP could be used to jointly invert two or

more 3-D datasets shot in different directions over the same subsurface volume. In this case, the illumination patterns of the different datasets would be different, allowing us to construct a regularization operator that would combine the information to produce a model with the best illumination from each dataset. RIP is very flexible and is really only limited by the creativity of the researcher.

The single greatest drawback in the use of RIP is that it is very computationally expensive when used for seismic imaging problems. Fortunately, parallel processing and improved processors and memory are making it possible to handle the enormous amounts of data now seen as commonplace in the oil exploration industry. It will soon be reasonable to use regularized inversion with model preconditioning to image complex areas where hydrocarbons are suspected.

Bibliography

Akbar, F. E., Stoffa, P. L., and Sen, M. K., 1998, Three-dimensional plane-wave kirchhoff depth migration:, *in* 68th Ann. Internat. Mtg Soc. of Expl. Geophys., 1708–1711.

Audebert, F., Nichols, D., Rekdal, T., Biondi, B., Lumley, D. E., and Urdaneta, H., 1997, Imaging complex geologic structure with single-arrival kirchhoff prestack depth migration: Geophysics, **62**, no. 05, 1533–1543.

Berryhill, J. R., 1979, Wave-equation datuming: Geophysics, **44**, 1329–1344.

Biondi, B., and Palacharla, G., 1996, 3-d prestack migration of common-azimuth data: Geophysics, **61**, no. 06, 1822–1832.

Biondi, B. L., 1999, 3-D Seismic imaging: Stanford Exploration Project.

Biondi, B., 2001, Kirchhoff imaging beyond aliasing: Geophysics, **66**, no. 2, 654–666.

Brandsberg-Dahl, S., de Hoop, M. V., and Ursin, B., 1999, Sensitivity transform in the common scattering-angle/azimuth domain: EAGE 61st Annual Conference, Expanded Abstracts, submitted.

Claerbout, J., and Nichols, D., 1994, Spectral preconditioning: SEP–**82**, 183–186.

Claerbout, J. F., 1985, Imaging the Earth's Interior: Stanford Exploration Project, `http://sepwww.stanford.edu/sep/prof/`.

Claerbout, J. F., 1995, Basic Earth Imaging: Stanford Exploration Project, `http://sepwww.stanford.edu/sep/prof/`.

Claerbout, J., 1998, Multidimensional recursive filters via a helix: Geophysics, **63**, no. 05, 1532–1541.

Clapp, R. G., Fomel, S., and Claerbout, J., 1997, Solution steering with space-variant filters: SEP–**95**, 27–42.

Clapp, M. L., 2003, Velocity sensitivity of subsalt imaging through regularized inversion: SEP–**114**, 57–66.

de Bruin, C., Wapenaar, C., and Berkhout, A., 1990, Angle-dependent reflectivity by means of prestack migration: Geophysics, **55**, no. 9, 1223–1234.

Dobrin, M., and Savit, C., 1988, Introduction to geophysical prospecting: McGraw-Hill, San Francisco.

Duquet, B., and Marfurt, K. J., 1999, Filtering coherent noise during prestack depth migration: Geophysics, **64**, no. 4, 1054–1066.

Fomel, S., Clapp, R., and Claerbout, J., 1997, Missing data interpolation by recursive filter preconditioning: SEP–**95**, 15–25.

Geoltrain, S., and Brac, J., 1993, Can we image complex structures with first-arrival travel-time?: Geophysics, **58**, no. 04, 564–575.

Hokstad, K., and Sollie, R., 1998, Multi-component elastic anisotropic kirchhoff migration:, *in* 68th Ann. Internat. Mtg Soc. of Expl. Geophys., 2044–2047.

Nemeth, T., Wu, C., and Schuster, G. T., 1999, Least-squares migration of incomplete reflection data: Geophysics, **64**, no. 1, 208–221.

Nolan, C. J., and Symes, W. W., 1996, Imaging and conherency in complex structure: Proc. 66th Annual International Meeting, 359–363.

O'Brien, M. J., and Etgen, J. T., 1998, Wavefield imaging of complex structures with sparse point-receiver data: 68th Annual Internat. Mtg., Soc. Expl. Geophys., Expanded Abstracts, 1365–1368.

Ottolini, R., and Claerbout, J. F., 1984, The migration of common-midpoint slant stacks: Geophysics, **49**, no. 03, 237–249.

Prucha, M., Biondi, B., and Symes, W., 1999, Angle-domain common image gathers by wave-equation migration: 69th Ann. Internat. Meeting, Soc. Expl. Geophysics, Expanded Abstracts, 824–827.

Richter, C. F., 1941, Elementary Seismology: Freeman, San Francisco.

Rickett, J., 2001, Spectral factorization of wavefields and wave operators: Ph.D. thesis, Stanford University.

Sava, P., and Biondi, B., 2001, Amplitude-preserved wave-equation migration: SEP–**108**, 1–26.

Sava, P., and Guitton, A., 2003, Multiple attenuation in the image space: SEP–**113**, 31–44.

Sava, P., Biondi, B., and Fomel, S., 2001, Amplitude-preserved common image gathers by wave-equation migration: 71st Ann. Internat. Meeting, Soc. Expl. Geophysics, Expanded Abstracts, 296–299.

Schneider, W., 1978, Integral formulation for migration in two and three dimensions: Geophysics, **43**, 49–76.

Schultz, P. S., and Claerbout, J. F., 1978, Velocity estimation and downward-continuation by wavefront synthesis: Geophysics, **43**, no. 04, 691–714.

Shuey, R. T., 1985, A simplification of the zoeppritz-equations: Geophysics, **50**, no. 04, 609–614.

Stoffa, P. L., Fokkema, J. T., de Luna Freire, R. M., and Kessinger, W. P., 1990, Split-step fourier migration: Split-step fourier migration:, Soc. of Expl. Geophys., Geophysics, 410–421.

Stolk, C., and Symes, W., 2002, Artifacts in Kirchhoff common image gathers: 72nd Annual Internat. Mtg., Soc. Expl. Geophys., Expanded Abstracts, submitted.

Tarantola, A., 1986, A strategy for nonlinear elastic inversion of seismic reflection data: Geophysics, **51**, no. 10, 1893–1903.

ten Kroode, A. P. E., Smit, D.-J., and Verdel, A. R., 1994, Linearized inverse scattering in the presence of caustics: SPIE - Conference on Mathematical Methods in Geophysical Imaging, 1247.

Tikhonov, A. N., and Arsenin, V. Y., 1977, Solution of ill-posed problems: John Wiley and Sons.

Wapenaar, K., Van Wijngaarden, A. J., van Geloven, W., and van der Leij, T., 1999, Apparent ava effects of fine layering: Geophysics, **64**, no. 6, 1939–1948.

Xu, S., Chauris, H., Lambare, G., and Noble, M., 1998, Common angle image gather - A strategy for imaging complex media: 68th Annual Internat. Mtg., Society of Exploration Geophysicists, Expanded Abstracts, 1538–1541.

Xu, S., Chauris, H., Lambare, G., and Noble, M., 2001, Common angle image gather - A strategy for imaging complex media: Geophysics, **66**, no. 6, 1877–1894.

Yilmaz, O., 1987, Seismic data processing: Society of Exploration Geophysicists, Tulsa.